Diploma Thesis

Correlative Light and Electron Microscopy of Magnetic Nanoparticle-Induced Stroke

submitted by

Platin Ramadani

for the Academic Degree of

Doktor der gesamten Heilkunde

(Dr. med. univ.)

at the Medical University of Graz

Gottfried Schatz Research Center for Cell Signaling, Metabolism and Aging

Under the supervision of

Assoz. Prof. Priv.-Doz. Mag. Dr. Roland Malli (Med Uni Graz)

Graz, 06.04.2023

Declaration of Academic Integrity

I, Platin Ramadani, hereby declare that the diploma thesis entitled “Correlative Light and Electron Microscopy of Magnetic Nanoparticle-Induced Stroke” is my original work. All individuals and organizations who have contributed to this work are fully acknowledged by name. No other sources of information other than those referenced have been used in composing this work. All legal requirements have been respected. This work is in accordance with the Standards of Good Scientific Practice of the Medical University of Graz.

Graz, 06.04.2023 Platin Ramadani eh.

Disclosures

Some content and figures of this thesis will be published later in a paper. For this reason, this work will be locked until the paper is published. These co-authors have contributed to the paper:

Severin Filser, Igor Khalin, Joshua Shrouder, Antonia When, Martina Schifferer, Nikolaus Plesnila (there might be more people involved in the final manuscript, but these are currently on the paper).

All authors and parties have given consent that some of their data is used in my thesis.

Acknowledgments

This thesis was my entry point into the world of science. I have always been an admirer of all natural sciences.

Therefore, my great gratitude goes out to my supervisor, **Prof. Roland Malli**, who immediately saw my interest in neuroscience and did not hesitate to introduce me to the research team of Prof. Nikolaus Plesnila at the Institute for Stroke and Dementia research of the LMU in Munich. He always helped me out with everything I needed and was very supportive of my work at all times.

Prof. Nikolaus Plesnila immediately took me into his research team and opened the gates to the world of neuroscience to me. I was allowed to be part of a great research team, where I learned more about neuroscience than I could have ever imagined and for that I am very thankful.

I also want to express my great thanks to my mentor in Munich, **Dr. Severin Filser**. He was a great teacher and mentor, who incorporated me into every step and all the experiments from day 1. He was always patient and motivated to teach me everything I needed to know. Dr. Severin Filser taught me what it means to be a scientist and has accompanied me as a mentor and a friend throughout my work.

My highest gratitude, I want to express to my loved ones, who have always given me support and love in every aspect of my life. They have motivated me to become the person I am today and if not for them I would not be where I am. Thank you to my parents, **Lirije** and **Florin Ramadani**, my partner **Elisabeth Brodacz**, my sisters **Jeta Muja** and **Argjenta Veseli,** and my cousin **Aulon Ramadani**.

Table of Contents

Abbreviations

Table 1: Abbreviations

2P	2-Photon
2PE	2-photon excitation
ATUM	Automated tape-collecting ultramicrotome
BBB	Blood brain barrier
CBF	Cerebral blood flow
CLEM	Correlative light and electron microscopy
CSD	Cortical spreading depression
EM	Electron Microscopy
ER	Endoplasmic reticulum
ET-1	Endothelin-1
FOV	Field of view
FP	Fluorescent protein
FRET	Förster resonance energy transfer
GC	Golgi complex
GECI	Genetically encoded calcium indicator
GFAP	Glial fibrillary acidic protein
GFP	Green fluorescent protein
ICA	Internal carotid artery
ICD	International classification of diseases
IONP	Iron oxide nanoparticle
LM	Light microscopy
LNP	Lipid nanoparticle
MCA	Middle cerebral artery
MCAo	Middle cerebral artery occlusion
MP	Magnetic nanoparticles
NA	Numerical aperture
NO	Nitric oxide
NVU	Neurovascular unit

PEG	Polyethylene glycol
RER	Rough endoplasmic reticulum
SAH	Subarachnoid haemorrhage
SEM	Scanning electron microscope
SIMPLE	Stroke induced with magnetic nanoparticles
SMC	Smooth muscle cell
TEM	Transmission electron microscope
TIA	Transient ischemic attack

Zusammenfassung

Schlaganfall war 2016 die zweithäufigste Todesursache weltweit. In den letzten Jahren ist die Zahl der Behinderungen durch Schlaganfall deutlich gestiegen. Die Therapieergebnisse sind sehr unzufriedenstellend. Einer der Hauptgründe dafür ist das geringe Verständnis der Pathophysiologie des Schlaganfalls. Die Wissenschaft hat verschiedene Methoden entwickelt, um ein besseres Verständnis zum Schlaganfall zu gewinnen, jedoch haben viele dieser Methoden große Limitationen. Um die Prozesse beim Schlaganfall besser analysieren zu können bedarf es Methoden, die die pathophysiologischen Vorgänge über die Zeit analysieren können und gleichzeitig Bilder mit sehr hoher Auflösung generieren können. Nanopartikel haben aufgrund ihrer Vielfältigkeit und niedrigen Toxizität in den letzten Jahren viel Aufmerksamkeit gewonnen. Eisenoxid-Nanopartikel haben einige charakteristische Eigenschaften, die im Rahmen dieser Arbeit kombiniert wurden, um einen experimentellen Aufbau zu schaffen, der Schlaganfallinduktion und korrelative Licht- und Elektronenmikroskopie ermöglicht. Sie sind ferromagnetisch und können verwendet werden um einen gezielten, reproduzierbaren, fokalen Insult *in vivo* zu induzieren. Sie können angeregt werden und im 2-photonen Mikroskop sichtbar gemacht werden. Außerdem sind sie im Elektronenmikroskop sehr leicht erkennbar aufgrund ihrer hohen Elektronendichte und können daher als Orientierungspunkt für korrelative Licht- und Elektronenmikroskopie verwendet werden. Die Methode wurde an einer Maus angewendet und es wurden elektronenmikroskopische Schnittbilder eines gestörten Mikrogefäßes nach Schlaganfall generiert. Zusätzlich wurden fluoreszierende Lipidnanopartikel verwendet, um die Dynamik von Lipidnanopartikel bei Schlaganfall zu beobachten. Die Analyse und 3D-Rekonstruktion der Bilder zeigte ein Loch in einer Endothelzelle mit anschließender Einstülpung extrazellulären Materials in das Gefäß. Weiters wurden deformierte Erythrozyten gesichtet und eine Immunreaktion durch Mikrogliazellen beobachtet. Außerdem konnte das Austreten von Lipidnanopartikel durch die intakte Blut-Hirn-Schranke via Transzytose festgestellt werden. Die hier vorgestellte Methode kann verwendet werden, um die Pathophysiologie des Schlaganfalls in hohem Detail zu erforschen.

Abstract

In 2016, stroke was the second most common cause of mortality worldwide. In recent years, the number of disabilities associated with stroke has increased significantly. The therapy outcomes are very unsatisfactory. One major reason is that much of the pathophysiology of stroke remains unknown. Scientists have developed various methods to a gain better understanding of the processes, but many have big limitations. To better understand what happens after a stroke, methods are needed that can trace the pathophysiological processes over time and create images with very high resolution at the same time. Nanoparticles have gained more and more attention in recent years, due to their versatile uses and low toxicity in living organisms. They are used as drug carriers to deliver substances to the desired location for therapy. Iron oxide nanoparticles have multiple characteristic properties that have been combined in this work to develop a method for stroke induction and correlative light and electron microscopy. They are ferromagnetic and can be used to induce targetable, reproducible, focal stroke *in vivo* with selective reperfusion. In addition, they can be excited and can be visualized in the 2-photon microscope. Furthermore, they are easily detectable in the electron microscope due to their very dark appearance and can therefore act as correlation landmarks for correlative light and electron microscopy. The method was applied on a mouse to create a z-stack of electron microscopy images of a disrupted microvessel after a stroke. Fluorescent lipid nanoparticles were used to observe the dynamics of lipid nanoparticles in the brain after stroke. The analysis and 3D reconstruction revealed a hole in an endothelial cell with an invagination of extravascular content, causing vessel constriction. Deformed erythrocytes and immune response of microglia were also observed. Additionally, lipid nanoparticles were seen exiting the vessel through an intact blood-brain barrier via transcytosis. The method introduced here can be used to investigate the pathophysiological processes of stroke in high detail.

1. Introduction

Epidemiological data gathered for the Global Burden of Disease Study shows that stroke was the second most common cause of mortality worldwide in 2016. The study reported a total of 5,5 million deaths related to stroke and a total of 80,1 million strokes on a global scale. Approximately 85% of all strokes were of ischaemic nature, the remaining 15% were haemorrhagic. The number of disabilities associated with stroke has increased significantly over the years racking with reports of 116,4 million disability-adjusted life-years in 2016 (1).

The definition of stroke has often changed in the past. The most recent iteration of the International Classification of Diseases, the ICD-11, recommends including transient ischemic attacks (TIA), cerebral infarctions, intracerebral haemorrhage, and subarachnoid haemorrhage (SAH) when speaking of stroke or cerebrovascular disease. The TIA is defined as an acute focal neurologic deficit, that disappears within 24 hours with no objective evidence of infarction during the symptoms and after remission. An ischemic stroke or cerebral infarction is present if symptoms persist for more than 24 hours, or radiologic findings of an infarction can be found. In this case, permanent damage to the affected brain tissue is highly likely. Global ischemia of the brain should not be included in the definition of an ischemic stroke. While focal ischemia is characterized by loss of brain tissue and function in the corresponding area of the affected occluded or stenosed artery, global ischemia of the brain is mostly caused by low blood pressure or an increase in intracranial pressure, leading to damage in the more susceptible areas of the brain, such as the basal ganglia, hippocampus, or the cerebellum. The pathophysiology, etiology, and treatment of focal deficits are very different from global deficits, making them two very distinct entities that should be separated (2).

Currently, the best therapy available for acute ischemic stroke is restoring the blood supply of the ischemic area via recanalization of the affected blood vessel. The most successful method developed so far to achieve that is thrombolysis. There are many possible side effects to this, and the success rate of thrombolysis is not satisfying. Currently, the main hypothesis for unsatisfying results of thrombolysis is that recanalizing an occluded blood vessel does not necessarily assure reperfusion of the tissue, also called incomplete microcirculatory reperfusion. Clinical data has shown that reperfusion is not present in at least 25% of successfully recanalized

ischemic strokes. In addition, further clinical studies have shown that the reperfusion rate of the tissue is a much better outcome predictor of thrombolytic therapy than recanalization. Experimental data suggest that the microcirculation of the ischemic area is severely impaired and damaged even after recanalization, leading to a bad nutrient supply. This effect has also been observed in the heart after the recanalization of blood vessels in ischemic heart attacks and is called the “no-reflow-phenomenon” (3,4).

Analysing the dynamics of larger arteries has improved massively over the past due to technological advances. The same cannot fully be said for small blood vessels which provide the microcirculation of the tissue. Small blood vessels are <100µm in size, making them very difficult to image and analyse, especially in *in-vivo* models. Most imaging data comes from MRI, but voxels of $1mm^3$ do not allow precise evaluation of small blood vessels and the tissue surrounding them. To further understand the vascular dynamics of small blood vessels during stroke, an experimental setting is needed which provides both high spatial resolution and precise temporal analysis of the pathophysiological microcirculatory processes (5,6).

1.1. Aims and Objectives

This work aims to establish an *in vivo* experimental setup and protocol that allows temporal analysis of stroke with high spatial resolution.

We determined the requirements for studying and tracking stroke in mice with high accuracy and detail:

- An animal stroke model that allows precise selection of the location for a stroke. The size of the stroke should be as small as needed to not harm the animals. All efforts were done to achieve that. In addition, the stroke model should allow recanalization of the occluded blood vessel to imitate the real-life event of a recanalized blood vessel after a stroke.
- Imaging techniques that allow temporal tracing of the stroke and the processes in the aftermath.
- Imaging techniques that create ultra-high-resolution images capable of resolving small vessels, cells, and subcellular compartments.

- Correlation-landmarks to correlate both imaging techniques mentioned above.
- Computer programs to analyse the gathered images.

For this research, I joined the working group of Prof. Plesnila and was mainly involved in the analysis of electron microscopy images, the generation of 3D reconstructions, and data interpretation.

1.2. Neurovascular Architecture of the Brain

The brain needs a very refined architecture due to its high demand for energy and complex functions. It relies solely on aerobic metabolism which is almost exclusively provided by glucose. A perfectly balanced and regulated blood flow is needed to provide the tissue with enough oxygen and glucose. As vessels form smaller branches, they become microvessels and start forming various loops and anastomoses throughout the tissue. Arterioles are surrounded by smooth muscle cells (SMCs) whereas capillaries show no SMC lining. The diameter of capillaries ranges from 5-8µm, while arterioles are larger than 8µm in diameter microvessels, neurons, glial cells, endothelial cells, SMCs, pericytes, basal membrane and the extracellular matrix among other structures are in constant communication and form the neurovascular unit (NVU). The NVU ensures that the cerebral blood flow is always in the correct balance and the required energy is delivered precisely whenever needed (7,8). The microvessels of the brain have a barrier to separate the blood from the tissue surrounding it, which is called the blood-brain-barrier (BBB). It prevents most inflow of blood substances to the brain, serving as a protective barrier. The BBB is a cellular formation and is constituted of endothelial cells with tight junctions, pericytes, and astrocytic end feet (9). Three different structures have been identified as sheathing structures of the endothelial lining in brain microvessels. Astrocytes, especially their end feet, make up approximately 63% of the endothelial surrounding structure. 3D reconstructions have shown that astrocyte end feet surrounding a microvessel usually do not leave space in between each other. In rare cases, small slits have been found, which were identified as microglial processes based on their electron density. In addition, the mitochondria in astrocyte end feet are distinct from mitochondria found in different tissues regarding both shape and size. They are inhomogeneously shaped as round or elongated mitochondria partly unbranched and in other cases with branches. The

remaining 37% that encapsulates microvessels are pericytes and pericyte processes. (10).

1.3. Pathophysiology of Ischemic Stroke

Ischemic stroke occurs when the brain receives a lack of oxygen and nutrients, due to occlusion or stenosis of supplying arteries. The occlusion can be caused by atherosclerotic processes which lead to the formation of plaques and thrombosis in the affected artery, or by embolism. In both cases, the blood supply is severed, leading to deficient oxygen and nutrient supply (11). The brain tissue has the highest demand for energy making it the most susceptible organ to ischemia (12).

Ischemia of the brain will lead to cell death within the span of a few minutes. The centre of the ischemia, the ischemic core region, is primarily affected. The ischemic core region is surrounded by a less affected, functionally silent but metabolically active region, which is called the ischemic penumbra. The penumbra is regarded as an already damaged, but still salvageable tissue if treated (13). A variety of cellular processes are involved in an ischemic stroke. Ischemia causes the depolarization of neurons, which subsequently activates glutamate receptors. This leads to a massive influx of Na^+ and Ca^{2+} into the cell and a shift of K^+ into the extracellular space. Water follows into the intracellular space resulting in cytotoxic oedema. The increase of intracellular Ca^{2+} leads to the activation of lipases, endonucleases, and proteases, which causes the accumulation of free radicals. The free radicals harm the cells, the mitochondria, and the DNA resulting in necrosis (14).

The accumulation of free radicals, glutamate, and Ca^{2+} and the necrosis cause massive inflammation in the ischemic core. In the process, the nuclear factor 'kappa-light-chain-enhancer' of activated B-cells, more commonly known as NF-kB, activates. This pro-inflammatory gene leads to the production of adhesion molecules and cytokines. They regulate the recruitment of inflammatory cells and further amplify the damage done to the ischemic core, by creating cyclooxygenase and other toxic mediators (15).

Apoptosis also takes place during ischemic stroke. It mainly occurs in the penumbra and can be observed even days after the initial stroke onset. In contrast to necrosis, apoptosis takes course in a much more regulated manner and tries to minimize the damage. The goal is to remove unnecessary cells and protect endangered cells in

close vicinity. Intrinsic as well as extrinsic mechanisms induce apoptosis. Intrinsic pathways are mostly mediated by mitochondria releasing cytochrome C and therefore activating caspases. Extrinsic mechanisms involve the binding of specific ligands to death receptors, which also activate caspases. Caspases will subsequently initiate apoptotic processes (13).

After ischemia, the BBB changes its usual function and behaviour. Permeability increases and the barrier function decreases. The integrity of the basal lamina is lost, and the brain endothelial cells interact with CNS cells, such as neurons, astrocytes, or microglia and intravascular cells, like leukocytes and platelets, which further enhances the damage done to the tissue. These interactions lead to poor microcirculation of the brain, pro-adhesive and pro-thrombotic processes, increased inflammation, and decreased barrier function of the BBB. Therefore, disruption of the BBB is a major problem that leads to harmful situations for neurons and brain tissue (14,16,17).

1.4. No-Reflow Phenomenon

The no-reflow phenomenon is characterised by deficient reperfusion of microvasculature after the recanalization of an occluded large artery supplying the tissue. Animal studies show that disruptions in microvessels start as soon as a couple of minutes after the onset of ischemia. The subsequent impairment of microcirculation or no-reflow begins approximately half an hour after onset (18). It has first been observed in the heart and further in the brain, skin, and kidney. Experimental studies hypothesize many potential mechanisms that could lead to no-reflow such as changes in the blood cells, astrocyte swelling, endothelial swelling, cortical spreading depression (CSD), inflammation, vasoconstriction, and contraction of pericytes. The results are poor healing in patients with myocardial infarction or stroke. A clear understanding of the mechanisms of no-reflow could therefore drastically improve the approach to stroke therapy (4).

1.4.1. Potential No-Reflow Mechanisms

Entrapment of blood cells could potentially be one of the contributing factors of no-reflow after stroke. Animal studies have shown sludging and stacking of erythrocytes, leukocytes, and platelets in microvessels following ischemia.

Significant neuronal damage was often observed after obstruction of microvessels (19,20).

Experiments on rats suggest that endothelial cells and astrocytes contribute to loss of perfusion after stroke. Occlusion of a large artery resulted in swelling of astrocytes and endothelial cells and reduction in luminal surface of the microvessels. This might influence blood flow and oxygen supply leading to neuronal death (21).

Astrocytes have distinct anatomy that ensures their function as supporting glial cells in the CNS. They form many delicate processes that travel to blood vessels or dendrites and encapsulate them with their so-called “astrocytic end feet” (22,23). Experimental data show that changes in astrocyte activity can influence cerebral blood flow (CBF). For example, Mulligan and MacVicar have shown that an increase in Ca^{2+} in astrocytic end feet can cause vasoconstriction in arterioles that are in communication with those astrocytes (24). Such increases in Ca^{2+} activity have been observed after increased neuronal activity amongst others, which raises the hypothesis that changes in the metabolic activity of neurons could influence blood flow via astrocyte communication (25). In addition to Ca^{2+}, other mechanisms have also been observed that led to both vasoconstriction and vasodilation, such as changes in arachidonic acid metabolites or nitric oxide (NO) activity. Therefore, astrocytes and other glial cells could potentially be one part of the NVU that influences blood flow in the brain in health and disease (26).

Endothelial cells seem to play an important role in controlling CBF. *In vivo* and *in vitro* experiments have shown that constriction, dilation, and permeability of blood vessels in the brain change after ischemia. These changes might occur due to an increase in the activity of vasoactive substances that affect the endothelial cells. Endothelin-1 (ET-1), NO, and 2-arachidonoglycerol seem to play an important role amongst others. They influence Ca^{2+} homeostasis and the endothelial cytoskeleton and have been associated with postischemic hypoperfusion. In addition to vasoconstriction and vasodilation, changes in the structural and functional integrity of endothelial cells can occur, such as tight junctions or membrane polarity. Endothelial cells are possibly an important factor regarding CBF changes in ischemia and reperfusion, especially in the microvasculature (27).

Pericytes are another part of the NVU which might cause disruptions in the microcirculation after ischemia, especially after reperfusion. They can mostly be found around microvessels, particularly around capillaries and venules with no SMCs. They are in close interaction with endothelial cells and possess proteins that enable contractile capabilities (28,29). Yemisci *et al.* discovered that microvessels constrict after ischemia and remain constricted even after the recanalization of the occluded artery. They further investigated the behaviour of pericytes during a stroke and after recanalization. Pericytes contracted during ischemia and remained contracted. The contraction could be alleviated to some degree when reducing oxidative and nitrative stress, while the application of peroxynitrite-induced contraction. In addition, they found segmental erythrocyte entrapment in capillaries which was possibly induced by pericytes. This hypothesis comes from the observation that erythrocyte entrapment mostly happened when a pericyte was around the capillary and rarely when no pericytes were involved. Since erythrocytes were entrapped and plasma flow was again present, they believe that there is a discrepancy between oxygen and glucose supply to the tissue, leading to acidity and other metabolic challenges for the penumbral tissue. In conclusion, damage to pericytes via ischemia and reperfusion could lead to disruption of the microcirculation after stroke despite recanalization of the occluded artery (19).

Mathematical studies suggest that vasogenic oedema might support the development of no-reflow after stroke. After a stroke, the changes in BBB permeability can cause an efflux of plasma filtration fluid in the interstitial tissue. The swelling could lead to compression of microvessels and further collapse of the microcirculation and CBF. The mathematical models show that this effect can occur, but only when given circumstances are met such as high reperfusion pressure, osmotic blood pressure, increased permeability of capillaries, and low stiffness of capillaries (30).

During and after an ischemic attack, the electrochemical properties of the brain tissue change. Especially in the penumbra different kinds of cortical spreading depression/depolarisations (CSDs) occur such as peri-infarct depolarizations and anoxic depolarizations. They have been shown to deteriorate CBF, induce vasoconstriction, and enlarge cortical hypoperfusion sites, resulting in a worse tissue survival rate. Dextromethorphan and other inhibitors of CSD improved CBF

and therefore had neuroprotective effects. This raises the hypothesis that CSDs might be an important contributor to no-reflow and poor outcomes of stroke (31).

1.5. In vivo Stroke Models in Rodents

This chapter will outline different methods to induce an ischemic stroke in a living animal.

1.5.1. Intraluminal Middle Cerebral Artery Occlusion (MCAo)

Intraluminal MCAo has historically been one of the most popular methods to induce a stroke *in vivo* in rodents. In a surgical procedure, the internal carotid artery (ICA) of one side is dissected in anaesthesia. A nylon filament is placed in the ICA and advanced further to the middle cerebral artery (MCA) blocking blood flow. The nylon filament can be retracted to reproduce blood flow at any given time point. Craniectomy is not needed in this method (32). Although a stroke with a penumbra can reliably be reproduced in rodents using this method, several drawbacks should be mentioned (33). Schmid-Elsaesser *et al.* used 3-0 and silicon coated 4-0 filaments to analyse the outcome of the method. They reported 30% SAH and 24% premature reperfusion with the former method and 8% SAH and 26% premature reperfusion with the latter. The premature reperfusion contributes to unreliable variability in results between individual animals (34). Intraluminal MCAo damages a substantially large part of the hemisphere, affecting vast amounts of the cortex, thalamus, striatum, hippocampus, and subventricular zone (35,36). Li *et al*. found that permanent MCAo and transient MCAo > 2h in almost all cases induced hyperthermia (>39°C) and were associated with hypothalamic damage (37).

1.5.2. Photothrombotic Stroke

For a photothrombotic stroke, a photosensitive dye is required. A very commonly used dye is Rose Bengal. It is applied to the animal, for example via the jugular vein. After the dye spreads systemically, a region of the brain is illuminated by light. The light needs to have a specific wavelength to excite the corresponding dye used. Illumination is usually done through a thinned skull or through a chronic cranial window, which will be explained in more detail in the chapter **“1.6.8 2PE Application *in vivo*: A cranial window”** (38,39). The dye reacts to the light by forming reactive oxygen species, which causes endothelial damage and further leads to platelet activation and the formation of thrombi. The occlusion leads to

cortical ischemia. The model was primarily used in rats, but applications for mice have also been developed (40,41). In a human stroke, the penumbra is a very important part of every stroke, which does not usually form in a photothrombotic stroke. This is a major concern because the penumbra is one of the hallmarks of human stroke (13,42). Scientists are concerned that the photothrombotic stroke model further does not mimic a human stroke due to the formation of vasogenic oedema in addition to the usual cytotoxic oedema (14,43). But it should be noted that the mathematical study by Mokhtarudin *et al*. suggests that vasogenic oedema might be involved in the no-reflow phenomenon (30).

1.5.3. Endothelin-1 (ET-1)-Induced Stroke

ET-1 is a long-lasting vasoconstrictive peptide, which modulates Ca^{2+} in SMCs (44). This property is used to induce focal cerebral ischemia at any given region by injecting ET-1 into a blood vessel of choice, the brain surface, or the parenchyma. The vasoconstriction caused by ET-1 leads to ischemia in that region. The duration and severity depend on the concentration, so the stroke can be modified to a certain degree (45–47). Later, the ET-1 effect diminishes and the vasoconstriction decreases, leading to reperfusion of the tissue. Thus, this model can be used to create transient focal ischemia (48). Oedema is very small, and ischemia develops in a very slow fashion, which is of concern to scientists because the situation does not mimic the human stroke and therefore results might not be translatable (49). In addition, astrocytes as well as neurons have ET-1 receptors, which might lead to misinterpretations caused by ET-1 itself and not by ischemia (50). The method has primarily been designed for rats but applications for mice have been developed as well (45,51).

1.5.4. Embolic Stroke

Embolic stroke can be induced by using microspheres (20-50 µm diameter) or macrospheres (100-400 µm diameter). The microspheres consist of different materials such as dextran or polyethylene and are instilled into the MCA or ICA with a microcatheter. The spheres are transported through the blood stream to the brain and cause multifocal infarcts, whereas macrospheres occlude the primary stem of the MCA and cause focal ischemia, similar to MCAo (52–54). Spherical microembolisation-induced infarcts do not accurately mimic a vascular human stroke situation, because it leads to redistribution of blood flow and a very rapid

collapse of the BBB, whereas in humans the BBB does not break down instantaneously (55).

Another way to induce an embolic stroke is by producing a thromboembolic clot in the animal's brain. This is achieved by applying a clot of autologous blood into the blood stream or by injection of thrombin into the intracranial part of the ICA or MCA (56–58). Although this model seems to be very close to a human situation there are still differences and sources of error for interpretation. Thromboembolic models are associated with high mortality and haemorrhage (59). The infarcts are often multifocal and very inhomogeneous with high rates of autolysis and unmanageable reperfusion (60,61). Human stroke observations have shown that accumulations of platelets with fibrin, neutrophils, monocytes, and a large number of erythrocytes all play an important role in the occlusion of vessels and ischemia, whereas thrombin-induced strokes in animals show very low participation of cellular elements and platelets (58,62).

1.5.5. Magnetic Nanoparticle-Induced Stroke

"Stroke induced with magnetic particles (SIMPLE)" (63) is a method developed by Jia *et al*. where magnetic nanoparticles (MP) are used to generate an ischemic stroke. Magnetic nanoparticles are injected into the tail vein/artery of a mouse and an external magnet is placed on the skull. This leads to an accumulation of nanoparticles in that area, occluding the blood vessels. The magnet can be placed wherever needed, so the stroke location can be chosen manually. The MPs consist of magnetite, which is an iron oxide and can be magnetized by applying a magnetic field from the outside. The external magnet used to generate the magnetic field consists of neodymium-iron-boron and is 1.2 mm long and 0.3-3.0 mm in diameter. The forces and reach of the magnetic field depend on the size of the magnet. Therefore, larger magnets should be used when trying to occlude larger arteries and vice versa. The chemical and biological properties of MPs can vastly differ depending on size and coating (63). Through the reticuloendothelial system MPs >10 nm and <200 nm quickly get cleared from blood circulation (64). Polyethylene glycol (PEG) has proven to be a biocompatible coating with low toxicity and low immunogenicity (65,66). Of all the different coatings PEG-2000 is best suited for achieving vessel occlusion *in vivo*. Another important feature of the MPs is their low remanence which is very useful to reverse the occlusion and accomplish

recanalization and reperfusion. After MP injection no inflammation was observed by Jia *et al*. as neurons, dendrite spine density, and microglial morphology and activity remained unchanged. They also compared different health parameters of mice between an MP-injected group and a control group. No significant distinction could be made between the groups in terms of blood oxygen, CO_2 and glucose, heart rate, body temperature, respiratory rate, and weight (63).

Imaging and induction of stroke can be done simultaneously if needed. To still be able to induce the infarction properly, a small diameter magnet is needed. Since the small magnet's magnetic field is weaker and has a shorter reach, it is helpful to reduce the distance between the magnet and the brain via thinned skull (38,63). The blood flow can be visualized using laser speckle flowmetry, where the velocity of a flowing liquid is translated into a map. This is possible due to laser light scattering on diffusing surfaces and creating speckle effects. The velocity of the flow creates different contrasts, which can be used to create a flow map (67,68).

The pathophysiological aftermath of the MP-induced vessel occlusion has been analyzed to assess if ischemic damage develops or not. MP-induced stroke led to mitochondrial impairment, neuronal degeneration, and disruption in blood vessels in the ischemic region. An increase in glial fibrillary acidic protein (GFAP) expression by astrocytes in peri-infarct areas was also detected. Reactive gliosis with increased GFAP expression is considered one of the most prominent reactions of the glial cells to ischemia and other forms of CNS injury. These observations suggest that SIMPLE is capable of causing ischemic injury in the brain (63,69).

1.6. 2-Photon Fluorescence Microscopy

To create functional live images of certain brain areas, specific methods, and tools are needed. One of the most used in neuroscience, especially for *in vivo* imaging, is 2-photon microscopy or 2-photon excitation (2PE). In combination with fluorescent molecules (e.g., fluorescent proteins) 2PE enables the creation of high-resolution images over time. In comparison with confocal microscopy, it allows the acquisition of images in higher depths and lower tissue photodamage (70).

1.6.1. Image Resolution

The resolution of an image is the smallest distance between two points that can be distinguished by the microscope. Therefore, the smaller the distance the better the

resolution and image quality. The smallest distance that can be detected depends on the wavelength of light or any electromagnetic wave (λ) and the numerical aperture (NA) of the lenses within the objective of the microscope. The NA is a dimensionless constant of optical systems such as lenses, that depends on the lens composition. The angle of the light cone that can be detected by a lens and the refraction index of the optical medium define the NA. Both the condenser lens, which condenses the light from the light source into a beam and the objective lens, which gathers the light coming from the specimen, have their respective NA. The smallest distance of distinguishable points next to each other in the xy-plane by the microscope (lateral resolution) can be defined as follows:

$$d_{min} = \frac{1.22\lambda}{NA_{obj} + NA_{cond}}$$

The smaller the value *d*, the better the resolution. Therefore, it can be concluded that the smaller the wavelength, the better the image quality (71).

1.6.2. Fluorescence

Luminescence is described as a phenomenon of light emission by a substance. The main requirement for this phenomenon to occur is the electric excitation of a substance. Luminescence can be further divided into fluorescence and phosphorescence. When the excited electron has the opposite spin to its paired electron in the ground state, it can return to the ground state in a rapid manner of approximately 10 nanoseconds and emits a photon as a result. This phenomenon is called fluorescence and usually appears in aromatic molecules. A fluorescent substance is called a fluorophore. By contrast when the spin of both electrons is the same, returning to the ground state happens much slower, resulting in slow emission rates, like milliseconds, seconds, or even minutes. This phenomenon is called phosphorescence. Excitation is usually the result of the absorption of incoming light. Therefore, it is important to note that a fluorophore has different absorbance qualities at different wavelengths of light, which are plotted in the absorbance spectrum. Another important characteristic of a fluorophore, especially regarding imaging, is its emission spectrum. It plots the intensity of fluorescence compared to the wavelength of the light emitted. In other words, it shows which wavelength of the emitted light gives the brightest signal. The emission energy is usually lower than the absorption energy. The resulting wavelength of the emitted

light is therefore longer. This shift in energy and wavelength between absorption and emission is called Stokes-Shift. The Stokes-Shift is an integral part of every fluorescence phenomenon. Lastly, a fluorophore has an excitation spectrum that plots the intensity of fluorescence to the wavelength of incoming light (72).

1.6.3. Fluorescent Proteins

In 1962, Shimomura *et al*. first described the extraction of the bioluminescent protein Aequorin from the jellyfish *Aequorea*, which emitted blue light when interacting with Ca^{2+}. Later they isolated the green fluorescent protein (GFP) from the same animal and were able to separate different components of GFPs, the most common being GFP a, b, and c (73,74). The discovery of GFPs marked a big milestone in life sciences since GFP and many other fluorescent protein variants (FPs) with different emission, absorption, and excitation spectra have become commonly used fluorescent markers. FPs have been developed and modified for many different uses over time. They possess many useful properties and are very convenient to use (75).

They can be used to label proteins, by genetic fusion of the FP gene code with the protein gene of interest. Wang and Hazelrigg were able to fuse GFP to a protein of Drosophila. The protein maintained most of its native function and behaviour and by labelling the protein with highly sensitive GFP they were able to localize and track it subcellularly (76).

FPs can also be utilized to label cells and tissue, which makes them very handy for *in vivo* imaging. Using the correct promoters and genetic modification, these transgenic animals can express different FPs in specific cells and tissues. These FPs can then be visualized by using their excitation wavelength. By attaching the Thy1-promoter to a GFP, for example, neurons can be targeted for GFP expression and imaged with fluorescence microscopy. It is therefore possible to specifically target certain cells in the CNS and image them *in vivo* with high sensitivity if the proper promoter and genetic composition are used (77–80).

One important application of FPs is based on the Förster Resonance Energy Transfer (FRET). Förster described a phenomenon where a molecule that functions as a donor can transfer the electron excitation energy applied to it to another similar molecule that functions as an acceptor. After the energy transfer, the acceptor

becomes the fluorescence-emitting subject. This process is only possible if those molecules are in a certain vicinity to each other, in most cases a few nm. The energy efficiency is indirectly proportional to the 6^{th} power of the distance between the donor and acceptor. This shows that distance is one of the key factors that make FRET possible (81). FPs such as GFP can be used as FRET molecules. By attaching two proteins of interest to corresponding FRET donors and acceptors, observations can be made about interactions between those proteins. Whenever the interaction brings the FRET molecules close enough to each other so that the FRET distance threshold is reached, a detectable and sensitive fluorescence signal is created (82,83).

FPs can also be used for the functional analysis of cells. A group of modified FPs called genetically encoded Ca^{2+} indicators (GECI) have become a common way to analyse neuronal behaviour. They achieve their fluorescent potential whenever Ca^{2+} is in the vicinity (84). An action potential in neurons usually activates Ca^{2+} channels and triggers Ca^{2+} influx into the cell causing high intracellular Ca^{2+} levels (85). The intracellular Ca^{2+} then interacts with the GECI and causes a fluorescent signal, which can be measured and related to the action potential of the neuron (86). In addition to *in vitro* usage, there are different approaches to utilizing GECIs *in vivo*, such as gene transfer via viruses or transgenic methods. Thy1 is a promoter that can be used to achieve high concentrations of GECIs which are applicable in long-term *in vivo* studies of neural populations (87).

1.6.4. Visualization of Iron Oxide Nanoparticles

The phenomenon of luminescence has been discovered in nanoparticle systems such as quantum dots and gold (88,89). Later, similar properties have also been discovered to occur in iron oxide nanoparticle (IONP) systems. Sadat *et al*. have described the luminescent properties of IONPs. In their study, polyacrylic acid-coated IONPs with 10 nm diameter and polystyrene-coated IONPs with 100 nm diameter were prepared and irradiated with a 4.5 mW laser at 407 nm wavelength. The IONPs showed very strong photoluminescence peaks at 540 nm for 10 nm particles and at 565 nm for 100 nm particles. A weaker peak at 690 nm and a small infrared peak at 840 nm were also observed. They further discovered luminescence in 5 µm large magnetite beads with a shift of wavelength towards red at about 571 nm. Larger clusters of nanoparticles show stronger photoluminescence intensity

because the particles collectively emit light. Additionally, small particles that are well-dispersed in polyacrylic acid cause scattering of incoming and emitted light, leading to lower detectable luminescence intensity. The underlying excitation mechanism of the electrons in the nanoparticles is made possible by surface plasmons (90). In metallic substances, surface electrons can be arranged in groups and oscillated by the incoming light. These groups of dense conductor surface electrons on metals are called plasmons. The plasmons can be oscillated by incoming light and change the light absorption and scattering properties of the particles. This effect called surface plasmon resonance makes metallic particles and their plasmons useful as photonic devices (91).

Additionally, IONPs can be visualized in electron microscopy. Due to the high electron density of iron oxide, IONPs are easily identified as they appear as very dark spots in the electron microscope (92).

1.6.5. Fluorescent Lipid Nanoparticles

Nanoparticles have gained a lot of interest in the past years as potential drug carriers. The BBB is a major concern when developing pharmaceuticals for the brain because it blocks the entry of most drugs to the parenchyma. To tackle this problem, drugs are often used in very high concentrations, which highly increases the risk of adverse effects. A lot of research aims to develop systems that can bypass the BBB and transport drugs safely to the brain parenchyma (93,94).

Lipid nanoparticles (LNP) are especially low in toxicity and might provide a means to transport drugs to the brain. They can carry and transport small molecules making them a candidate for a drug-delivery system to the CNS. Khalin et al. have tested 30 nm and 80 nm LNPs in traumatic brain injury. They found that both LNPs travel through the damaged BBB and 30 nm LNPs also traversed the intact BBB, especially in occluded vessels. They suggested that transcytosis through the endothelial wall might occur due to the low velocity of blood flow in the occluded vessels (95–97).

LNPs can be attached to highly fluorescent dyes and imaged in confocal or 2-photon microscopy. In the before-mentioned work by Khalin *et al*. LNPs were loaded with rhodamine and a brightness-enhancing bulky counterion. With this method, LNPs

could be visualized in 2-photon microscopy. Additionally, LNPs are visible and can be observed in electron microscopy, as shown by Marschallinger *et al*. (97,98).

1.6.6. Basics of Confocal Microscopy (1 Photon)

Imaging fluorophores with conventional light microscopy (LM) seems to be a near-impossible task due to the scattering of light and intensive out-of-focus light even at very little depth, leading to unusable, blurry images with low contrast. The first step to overcome this problem was the development of the confocal microscope by Marvin Minsky. In contrast to a conventional microscope, a confocal microscope first limits the illuminated area with a pinhole. After passing a lens an image of the pinhole is created in the focal point where the specimen is located. A second lens focusses the light precisely on a second pinhole where the image of the specimen is created and detected by a photocell. This setup ensures that only the light in focus of the specimen passes the second pinhole, without letting most of the scattered light through. However, this implies that only a small field of view (FOV) is imaged. Therefore, a scanner is needed to acquire multiple images of the specimen with a raster pattern, which can then be computed into an image. The technology has advanced ever since confocal microscopy has been introduced, with lasers being used as light sources, scanners becoming more precise and faster, and computing power allowing better and faster acquirement of images (71,99).

It should be noted that confocal microscopy has its limitations and drawbacks. After a certain time of excitation, fluorophores can irreversibly lose their fluorescent capabilities. This photobleaching effect most likely occurs due to the creation of reactive singlet oxygen during the excitation process. The reactive species also targets other biological structures in close vicinity resulting in phototoxicity. Experimental studies have shown that 2-photon excitation can greatly reduce photobleaching effects (100–102). As explained in the resolution chapter, the wavelength of light is a strong resolution limiting factor. The pinhole itself is used to only gather useful in-focus light, but at the same time it severely limits the number of photons gathered, especially if the pinhole is made small enough to prevent diffraction effects. Few photons lead to statistical inaccuracy and non-visible images. On the other hand, a larger pinhole allows the signal from neighbouring planes to come through, reducing z-resolution. Lastly, especially in *in vivo* imaging the tissue is rarely homogenous. The light beam will be either absorbed or scattered

to other directions after a certain depth so that the signal becomes impossible to measure. The inhomogeneity also defocusses the incoming and outgoing light, so much of the signal that should return in theory doesn't do so because it is out of focus (71).

1.6.7. 2-Photon Excitation and its Application in Fluorescence Microscopy

In 1931 Maria Goeppert-Mayer discovered that an atom can not only be excited by an incoming photon with the corresponding excitation frequency, but also by two photons whose sum of frequencies equals the excitation frequency of the atom (103). A research group was able to trigger this effect in organic matter in 1963 using a laser (104). Denk *et al*. applied 2PE to fluorescent dyes with a laser microscope in 1990 and studied the effects. They show that to trigger 2PE in fluorescent dyes, a laser is needed that creates instant, intense, and short femtosecond long pulses of light. Using long wavelength (or short frequency) light in such a laser creates a high probability of 2 photons uniting and exciting the fluorophore with their sum of energy (105). This has multiple benefits compared to a confocal microscope. First, only the ROI receives the laser intensity needed to cause 2PE. Therefore, no other spot, neither in xy nor in z, receives the excitation wavelength of light to create a signal, which makes the image free of out-of-focus light. Because only a selected spot is excited, photobleaching and photodamage are also greatly reduced. Secondly, since the ROI is selectively excited, and all the other regions do not emit unwanted signal, the exit pinhole of a confocal microscope is unnecessary. All these factors lead to higher image quality and deeper imaging possibilities. The main limiting factors of 2PE or even multi-photon excitation are complex lasers and high cost (71,105).

1.6.8. 2PE Application in vivo: A cranial window

When trying to image the brain with microscopy in a living animal, the layers of dura mater, skull, skin, and fur are blocking the light source. To overcome this problem, protocols have been developed to perform surgeries where a part of the skull is carefully removed and replaced with a thin cover glass, which is attached by dental acrylic. The FOV of the window ranges from 0,8mm^2 – 12mm^2 (39). Additionally, protocols have been established to implant a femoral catheter for substance application (106). Multiple studies have analyzed the effects of performing this surgery on brain functionality, plasticity, inflammation, and other factors. While there

is one study that shows a drop in dendrite spine density and activation of astrocytes and microglia, most other studies show stable boutons and spines for months and glial cell activation seems to be low and temporary (107–112). The chronic cranial window is an important tool for long-term *in vivo* imaging of fluorescent markers in the brain. It enables imaging of neuronal populations and structures over time at any given time point while the brain remains comparable to a naive one. It is of utmost importance that all surgeries and experiments are carried out under national and institutional guidelines and with the best care for the animals (39).

1.7. Electron Microscopy (EM)

The discovery that electrons have wavelike properties in addition to particle properties set the base for electron microscopy. De Broglie applied Einsteins and Plancks' findings on quantum mechanics and waves on electrons. He proposed that an electron should have a wavelength of approximately 0.17nm if accelerated through a vacuum with 50V. This makes the spatial resolution of EM much better than LM because shorter wavelength results in a smaller distinguishable distance, as shown in the chapter *"Image Resolution"* (71,113). Focussing these short-wave electrons allows the creation of images with much higher spatial resolution than with light microscopes. Shortly after De Broglies' findings, other research groups showed wave-like character experimentally and even the first microscope using electrons was proposed by Ruska and Knoll and used to create images with higher resolution than with a light microscope (113–115).

1.7.1. Electron Interactions with Matter

When an electron interacts with matter many processes can happen, which are ultimately used to gather information about the specimen. It is important to note that any light is only visible when it interacts with a certain matter, otherwise, it remains invisible to the eye. Similarly, electron-matter interactions are needed to gain structural information about the specimen (115).

The first possible interaction is scattering in a particle manner. When the electron hits a specimen, it can either remain on its path or be scattered in another direction. Since electrons can be treated like charged particles, they interact with electron clouds or even positively charged nuclei if they pass the electron cloud. This interaction changes the motion direction of electrons in the beam. It can result in

forward scattering or backward scattering when the angle of the scattered electron is above 90° compared to the incoming beam. Backward scattering usually occurs more the bulkier the specimen is. The probability and amount of scattering depend on different factors like the atomic weight or the incoming electron energy. The result is a combination of non-scattered electrons passing through the specimen and scattered electrons. The information on both is important to generate structural and chemical data of the specimen. It should also be noted that an electron can scatter more than once on its way to the detector depending on the probability. The scattering can be elastic, where energy is preserved in the electron, or inelastic, where some of the electron energy is transferred somewhere else, e.g. the specimen or other electrons (115).

Diffraction is another effect that occurs after the interaction of electrons with the matter. This is because electrons do not only act as particles but also as waves. Any electromagnetic wave passing the edge of a gap causes a new circular wavelet. Every atom in the specimen can be treated as the source of a new circular elementary wave. The waves interfere with each other and can either negate themselves or increase the amplitude, depending on the phase shift. The amount of diffraction and the resulting patterns depend on diffraction circumstances such as wavelength, incoming angle, or specimen constitution (115,116).

Inelastically scattered electrons can deliver some of their energy to the outer shell electrons of atoms belonging to the specimen. These outer shell electrons are very loosely bound to their atoms and can be emitted off the surface by receiving the energy of inelastically scattered electrons. These secondary electrons are not to be confused with the previously mentioned backscattered electrons. They have a different origin and usually, their kinetic energy is lower than that of backscattered electrons (116).

1.7.2. Creating an Electron Beam

The electron beam can be created by either thermionic emission or by field-emission. In thermionic emission, the electron beam is created using heated tungsten or lanthanum hexaboride. After heating the material to a certain degree, the electrons receive enough energy to break out of their atom barrier. In field-emission, high electric potentials are created between the emission gun and an

anode using high voltage. If the electric field is strong enough, it will create an emission of electrons. Combinations of both mechanisms are also used to create high-energy electron beams. It should be noted that at a certain degree, the energy of electrons becomes so high that it ionizes atoms and irreversibly damages biomass (113,115).

1.7.3. Transmission Electron Microscopy (TEM)

One of the applications of EM is the TEM, where electrons that are transmitted through a specimen are used for imaging. Forward elastic scattering and diffraction are the effects that give us the most information about the specimen in a TEM. The specimen cannot be too thick, because it would hinder electrons from passing through, which is one important limitation of the TEM. The sample needs to be cut with a very sharp knife to create ultra-thin slices. Simply speaking, the angular and spatial distribution of slightly scattered light (either by forward scattering as a particle or diffraction) is detected by a detector and computed into a signal. The reason why the distribution can be used as a signal is that the probability and amount of scattering heavily depend on the constitution of the specimen at every single location. In a similar sense, the diffraction pattern results from specific gaps that are different depending on the structure of the specimen. The scattering events and diffraction patterns (and thus the contrast of the image) can be controlled to a certain degree by adjusting the energy and the angle of the beam. Inelastic scattering also delivers important information that can be used to generate data. The transfer of energy in inelastic scattering can result in the emission of X-Rays. These X-rays and their energy contain important information about the elements constituting the specimen. Simply speaking, an electron loses a certain amount of energy while going through the specimen in form of X-Rays. Depending on the atoms the energy-loss is different, resulting in different X-Ray signals that can be detected. The resolution of TEMs is extremely high, with modern devices reaching resolutions up to 60pm. The final image is always 2-dimensional, although, as thin as the specimen might be, it still is a 3-dimensional structure (113,115).

1.7.4. Scanning Electron Microscopy (SEM)

The previous chapter explained that TEM uses electrons that pass through a thin specimen and their information about the spatial distribution of forward elastic scattering, diffraction patterns, and to a certain degree X-Rays to compute a 2-

dimensional image of the specimen. In SEM other phenomena are used to create an image. After the electrons are accelerated through the vacuum chamber, they undergo elastic backward scattering on the surface of the specimen and secondary electrons also emit backward due to inelastic scattering. Since electrons do not need to pass through the specimen in SEM, the sample does not need to be thinly cut, which makes sample preparation a great deal easier compared to TEM. One problem that occurs is that the secondary electrons are so vastly different in energy that it is very difficult to focus them with electron lenses. To overcome this problem, the SEM creates many small signals of the surface at a time in a raster pattern and transforms the entirety of the scanned surface into a 3-dimensional image. The resolution of modern SEMs lies between 1-10nm, and large areas can be imaged due to the scanning system. X-Rays are also used as analytic signals like in the TEM (113,115,116).

1.7.5. ATUM-SEM

Imaging large neural circuits is difficult with a simple TEM or SEM apparatus because the areas of interest are very large. Multiple techniques have been developed to overcome these difficulties. One possibility is the ATUM (automated tape-collecting ultramicrotome) in combination with an SEM. The ATUM uses very sharp diamond knives to cut samples into very thin slices. Using an SEM in low resolution, the entirety of the area can be scanned rather quickly. After finding specific ROIs, the SEM-resolution can be increased to create a high-quality image (117). The SEM is far superior compared to a TEM in this situation because a large number of slices can be handled much more easily on a stable substrate than with a TEM where transmission of electrons is only possible on unstable and inconvenient substrates. One major problem is that manually finding corresponding ROIs of thousands of large slices is a very time-consuming and difficult task. For that reason, Hayworth *et al*. have developed software that can semi-automatically map ROIs of a tissue created by an ATUM before imaging by checking anatomical landmarks and creating section libraries. Using these libraries, the software can gain quick access to corresponding ROIs of multiple slices. Combining the ATUM with this software, multiple z-stacks of very thin 2-D images of different ROIs can be created at high speed while keeping the high resolution of the SEM in the ROIs (118).

1.7.6. Correlative Light and Electron Microscopy (CLEM)

One of the major drawbacks of EM in contrast to LM is that the sample needs to be fixed, resulting in a static image of one time point. Therefore, valuable temporal and dynamic information is lost. To compensate for that, approaches have been made to correlate information gathered from LM with EM. One problem is that, even though certain fixation methods have been developed to try and overcome this problem, fluorescent signals are still very faint or even non-existent in EM. Due to this fact, spatial correlation is a very difficult task when performing CLEM. Especially in large areas such as entire neural circuits finding the exact same location in LM and EM is very problematic. Most methods lack the correlation landmarks to easily and precisely find the same ROIs in large images (119).

EM requires fixation of the sample, which is irreversible, so timing is another important factor. LM can be incorporated at any point in time and delivers a different kind of information depending on when it is performed (120). The first group of methods is when LM is performed before EM. This is done to gain dynamic, functional, and temporal information with fluorescence microscopy over longer periods. After the LM sessions samples are prepared and imaged in EM to gain high-resolution spatial information (121–123). The group focuses on EM first and tries to preserve fluorescent signals with specific fixation methods. The temporal correlation between the LM and EM is better with this method, because the time in between imaging sessions is minimal, although the loss of fluorescence and autofluorescence of the resin limit these methods (119,124). Cryo-LM is another approach where fluorescent markers are preserved with cryo-techniques. LM can be used on a vitreous sample just before EM, but the setup is very complicated and the cold temperature worsens the optical results of these methods (125).

1.7.7. Mip Mapping

The images acquired by the EM have a high resolution. Overviewing high-resolution images can cause aliasing effects, which disturb the original images. To solve this problem, programs use anti-aliasing methods. The idea behind it is to reduce the level of detail as the image gets farther away from the viewer. Reduced levels of detail will also reduce aliasing effects. Therefore, a mip map will reduce the resolution of an image when zooming out a certain distance to avoid aliasing effects and still have a good-quality image (126).

1.8. Ultrastructure of the Brain

This chapter will summarise the characteristics of different components of the brain in the EM. This information is helpful to identify different cell types and subcellular components of EM images of the brain. Most of the information is based on the criteria of Peters *et al*. and SynapseWeb (127,128).

1.8.1. Neurons

In the EM neurons often show large euchromatic nuclei, with potentially multiple more electron-dense nucleoli and often nuclear pores. Very active neurons occasionally show invaginations in their nuclei. Subcellular characteristics are a very noticeable Golgi complex (GC) in the close vicinity of the nucleus, accompanied by long and flat rough endoplasmic reticulum (RER) with high loads of ribosomes. Near the GC groups of 40-80 nm large vesicles accumulate to build multivesicular bodies, becoming more concentrated as they move closer to the axon. The neurons contain numerous mitochondria of round and oval structures depending on the image slice. Every now and then lysosomes filled with lipofuscin, characterized by their high electron density, can be found. Polyribosomes or single ribosomes roam the space between cell organelles. Large amounts of microtubules and neurofilaments arrange and expand throughout the dendrites (127,129).

1.8.2. Astrocytes

Astrocytes represent the most frequent of all glial cells in the brain. They can be divided into two subtypes, protoplasmic and fibrous. While protoplasmic astrocytes have many branches of processes in various directions and are mainly present in the grey matter, fibrous ones tend to have longer straight processes and are mostly present in the white matter. Protoplasmic astrocytes can be identified by trigonal-like protuberances, pale cytoplasm with intermediate filaments (GFAP) of 8-12 nm diameter, and a pale nucleus with a narrow rim. One of the most distinguishable traits of astrocytes in the EM is their general low electron density. In addition to the cytoplasm, astrocyte mitochondria often appear lighter than mitochondria of other glial cells, endothelial cells, pericytes, or neurons. Other organelles can also be found, especially near the nucleus, such as GCs, Lysosomes, and rough ER (RER). Astrocytes send out long processes to small blood vessels and encapsulate them with their astrocytic end feet. With these end feet, astrocytes form a very important component of the BBB and the NVU (127,130–132).

1.8.3. Oligodendrocytes

Oligodendrocytes also belong to the group of glial cells and have darker, more electron-dense, rectangular cytoplasm compared to astrocytes. One of the most characteristic traits of oligodendrocytes is the nucleus with a very heterogenous electron density pattern. The endoplasmic reticulum is rather short and wide and can be found close to the nucleus, as well as the GC. Ribosomes, mitochondria, and short sections of RER roam the free spaces of the cytoplasm (127).

1.8.4. Microglia

Microglia can sometimes be difficult to distinguish between oligodendrocytes, because of their electron-dense, dark cytoplasm. The soma of microglia is smaller than of other glial cells and neurons and often of triangular shape. The nuclei have characteristic patterns of multiple heterochromatin spots in the periphery, which are identified as more electron-dense areas in the peripheral nucleus. The endoplasmic reticulum often forms long cisterns with lipids such as lipofuscin, lipid droplets, or lysosomes. Primary lysosomes are smaller (<1µm) and have homogenous content, whereas secondary lysosomes are larger (>1µm) and have heterogenous content. Microglia are in close communication with blood vessels, synapses, dendrites, astrocyte processes, and axon terminals. They can often be found in the areas between microvessels and neurons where they fulfill their role as immune cells in the CNS (133–135).

1.8.5. Endothelial Cells and Pericytes

A basal lamina separates the perivascular space from the glial cells and neurons. Astrocyte end feet rest on the abluminal side of the basal lamina. Within the perivascular space, pericytes and endothelial cells are located, therefore pericytes are not regarded as glial cells. Pericytes can be distinguished from endothelial cells because they are encapsulated by a basal lamina from all sides. The nucleus is often elongated and possesses homogenous chromatin. Capillary pericytes send out primary processes in multiple directions that encapsulate the endothelium. Secondary flattened processes emerge from the primary ones, covering a large area of the endothelial wall with circular projections. Pericytes and endothelial cells have a similar cytoplasm, although the electron density of pericytes can be lower and therefore paler than that of endothelial cells. Organelles are present but rather sparse in pericytes. Endothelial cells build the innermost lining of the blood vessels.

They are mostly separated from the pericytes by basal lamina, but in some locations, the lamina becomes thin or missing. In these locations, pericytes and endothelial cells are in close contact via gap junctions, adhesion plaques, or so-called “peg and socket” interdigitations (127,136,137).

1.8.6. Neuropil

The neuropil is a large net of glial and neuronal processes stretching out from the cell bodies. Myelinated axons can be easily identified by their highly electron-dense myelin sheath and are often accompanied by encapsulating oligodendrocyte processes. Unmyelinated axons are mostly found within bundles and have more regular contours, more microtubules, and fewer bumps than dendrites. The presynaptic end of an axon, also called bouton, can be identified as a swollen terminus, mostly filled with presynaptic vesicles of neurotransmitters. Dendrites possess an actin cytoskeleton, which appears as a fluffy content resembling cotton. Dendritic spines are in contact with axon terminals to form synapses. In the post-synaptic area, the electron density becomes very high in mature spines (127,138,139).

Astrocyte processes are very distinct, as they are much more angular and irregular in their path, whereas neuronal or other glial processes show rather round cross-sections and more regular expansion patterns. Their cytoplasm is also very low in electron density, therefore appearing in a very light colour. In pathologic conditions, perivascular astrocyte end feet swell and take up glycogen granules. Microglial and oligodendrocyte processes, on the other hand, have a denser cytoplasm which appears rather dark in the EM while neuronal processes mostly occupy a middle ground regarding electron density. The easiest way to identify an oligodendrocyte process is when it is found in direct contact with myelin sheaths of axons. Oligodendrocytes and microglia extend similarly with obtuse angles, whereas astrocytes extend in acute angles. Microglial processes are often surrounded by larger extracellular space than others. Additional characteristics of microglial processes include large vesicles, cellular inclusions of many kinds, numerous endosomes, and long-reaching endoplasmic reticulum (127,131,139–141).

2. Materials and Methods

The experiments were carried out at the Institute for Stroke and Dementia Research of the Ludwig-Maximilian University in Munich. Application for ethical approval was made by Prof. Nikolaus Plesnila and approved by the Ethical Review Board of the Government of Upper Bavaria. Data collection was performed according to the ARRIVE guidelines (142). Laboratory animal activities, hygiene management, animal health monitoring, training and education were carried out in compliance with guidelines by the Federation of European Laboratory Animal Science Associations (FELASA) (143).

2.1. Basic Experimental Setup – Data acquisition

A C57/B16N transgenic mouse (Charles River Laboratories, Kisslegg, Germany) with a CXCR1 promoter expressing GFP in microglia was used to observe the immune response among others (CXCR1-GFP). Surgery was performed on the mouse to place a cranial window on the skull using the method of Holtmaat *et al*. and to insert a femoral catheter for substance application as established by Khalin *et al.* (39,106). All instruments for surgery were thermically disinfected. The surgery was performed with a stereomicroscope under sterile conditions. The mouse was anaesthetized with an intraperitoneal injection of medetomidine-midazolam-fentanyl for surgery. To keep the body temperature stable, the mouse was constantly on a heating pad. The head of the animal was fixed on a holder and bepanthen ointment was applied to the eyes during the surgery to protect them from dryness. The scalp was removed with scissors after disinfection. Trepanation of the skull was performed with a drill with the help of stereotactic devices for orientation. The skull was not fully penetrated with the drill, but thoroughly thinned. Sterile phosphate-buffered saline was applied to the craniotomy and the bone and dura mater were carefully removed with forceps. Subsequently, a glass coverslip was placed on the craniotomy and fixed with tissue adhesive. Buprenorphine and Carprofen were used to reduce pain and inflammation. Afterwards, the femoral artery catheter was placed. For a more in-depth description, see the work by Holtmaat *et al.* and Khalin *et al*. (39,106).

Stroke induction was achieved with magnetic nanoparticles via SIMPLE (63). 150 µl of MPs were inserted through the catheter. The magnet was placed on the cranial window of the anaesthetised mouse for 1 hour to induce focal ischemia. After

magnet removal, 100µl of rhodamine-based fluorescent lipid nanoparticles were inserted through the catheter. The brain was imaged *in vivo* with the 2P microscope for 1 hour using fluorescent lipid nanoparticles and luminescent magnetic iron oxide nanoparticles. The animal was under isoflurane anaesthesia during 2P-microscopy.

Immediately after *in vivo* imaging the mouse was prepared for electron microscopy using magnetic nanoparticles as correlation landmarks. The mouse was transcardially perfused with 3.5% formaldehyde and 0.5% glutardialdehyde in phosphate-buffered saline for fixation. The mouse was decapitated after 1h of perfusion. Subsequently, the brain tissue was cut using a vibratome, creating a 300 µm thick brain slice. After the slice was inspected in the light microscope, electron microscopy images were acquired using the ATUM-SEM protocol developed by Hayworth *et al*. (118). The raw images were then reconstructed in 3D to improve analysis.

2.2. Equipment

2.2.1. Hardware

Table 2: Hardware

Name	**Usage**	**Company**
500-550 band pass filter	Green band pass fluorescence filter	Carl Zeiss AG Oberkochen, Germany
575-610 band pass filter	Red band pass fluorescence filter	Carl Zeiss AG Oberkochen, Germany
Blue Line – SEALSAFE NEXT	Mouse housing cages	Tecniplast Deutschland GmbH Hohenpeißenberg, Germany
Chameleon Vision II	Ti:Sa laser for LSM 7MP	Coherent, Inc. Santa Clara, USA
Crossbeam Gemini 340 SEM	Scanning electron microscope for ATUM-SEM	Carl Zeiss AG Oberkochen, Germany
DC Temperature Controller	Mouse thermoregulation	FHC, Inc. Maine, USA

Demi Ultra LED UV light	IBOND and Tetric EcoFlow polymerization	Kerr GmbH Herzogenrath, Germany
DFC290 HD	Camera module for Leica M80	Leica Microsystems Wetzlar, Germany
Elmasonic S 10 H Ultrasonic cleaning device	MP preparation	Elma Schmidbauer GmbH Singen, Germany
Heating Pad (5x12.5 cm)	Temperature control during surgery with DC Temperature Controller	FHC, Inc. Maine, USA
Isoflurane funnel-fill vaporizer (34-1040SV)	Storage and distribution of Isoflurane during surgery	Harvard Apparatus, Massachusetts, USA
KL2500 LED	Light source for Leica M80	Leica Microsystems Wetzlar, Germany
LSM 7MP	2P-microscope	Carl Zeiss AG Oberkochen, Germany
M80 microscope	Stereomicroscope for surgery	Leica Microsystems Wetzlar, Germany
Mediheat™	Heating cabinet for the mouse post-surgery	Pecoservices Brough, UK
Mixer Uzusio VTX-3000L	Shaker for MP preparation	LMS Co., Ltd. Tokyo, Japan
Stereotaxic Instrument	Mouse fixation during surgery	Harvard Apparatus Massachusetts, USA
Uni-drives	Craniotomy drill	Rewatronix Wald-Michelbach, Germany
W Plan-Apochromat 20x/1.0 NA	Water immersion objective for LSM 7MP	Carl Zeiss AG Oberkochen, Germany
Weighing scales	Scale for mouse body weight	OHAUS Nänikon, Switzerland

2.2.2. Surgery instruments

Table 3: Instruments

Name	**Usage**	**Company**
Biopsy Punch BP-30F	Placement of round mark on the skull bone	KAI Europe GmbH Solingen, Germany
Dumont Forceps Micro-Blunted Tips (11253-25, 11273-20)	Periosteum removal, scalp fixation, handling of filaments, exposure of femoral artery, catheter insertion	Fine Science Tools GmbH, Heidelberg, Germany
Extra Fine Bonn Scissors (14084-08)	Fur removal for skull and femoral artery exposure	Fine Science Tools GmbH, Heidelberg, Germany
Micro-Serrefine Clamp (18055-04)	Transient ligation of the femoral artery	Fine Science Tools GmbH, Heidelberg, Germany
Micro-Serrefine Clamp Applying Forceps (18057-14)	Micro-Serrefine Clamp placement at femoral artery	Fine Science Tools GmbH, Heidelberg, Germany
S&T Forceps SuperGrip Tips (00632-11)	Removal of dura mater	Fine Science Tools GmbH, Heidelberg, Germany
Safeshield Scalpel No. 20	Carving the bones during surgery	FEATHER Safety Razor Co., Ltd. Osaka, Japan
Student Dumont #5 Forceps (91150-20)	Filament handling, femoral artery exposure and catheter insertion	Fine Science Tools GmbH, Heidelberg, Germany
Vannas Spring Scissors 3mm Cutting Edge (15000-00)	Opening of the femoral artery	Fine Science Tools GmbH, Heidelberg, Germany

2.2.3. Consumables

Table 4: Consumables

Name	**Usage**	**Company**
20-gauge needle	Catheter preparation for femoral artery	B. Braun SE Melsungen, Germany
3M™ Vetbond™ Tissue Adhesive	Glass coverslip fixation on the cranial window	Fisher Scientific GmbH Schwerte, Germany
Cotton Applicator	Bepanthen application and fur removal from the wound	NOBAMED Paul Danz GmbH Wetter (Ruhr), Germany
Durapore 3M Silk Tape	Hind limb fixation during femoral artery surgery	3M Deutschland GmbH Neuss, Germany
Eye spear	Blood and saline removal	BVI International Sales Ltd. Oxfordshire, UK
Fine Bore Polythene Tubing	0.38 mm inner diameter, 1.09 mm outer diameter, catheter preparation	Smiths Medical International Ltd. Kent UK
Gazin® Gauze Swap	Heating pad cover	Lohmann & Rauscher GmbH & Co. KG Neuwied Germany
Glass cover slips (CS-3R-0)	3.0 mm diameter, bone replacement for cranial window,	Warner Instruments, Inc. Hamden, CT, USA
iBOND® Self Etch	Adhesive layer on the skull pre-surgery	Kulzer GmbH Hanau, Germany
Injekt®-F Duo	Injection of pharmaceuticals, injection of substances through the catheter	B. Braun SE Melsungen, Germany
Insta-Set™ Accelerator	Maxi-Cure™ Super Glue polymerization accelerator	Drechseln und Mehr Weiden, Germany

Maxi-Cure™ Super Glue, CA	Femoral artery catheter fixation and wound sealing	Drechseln und Mehr Weiden, Germany
Microbrush®	0.5 mm fine brush	Microbrush International Grafton, WI, USA
Mikrozid® AF wipes	Disinfection of instruments and surface areas	Schülke & Mayr GmbH Norderstedt, Germany
Nanomag®-D	PEG-2000 coated MPs with 180 nm diameter, 10mg/ml	Micromod Partikeltechnologie GmbH Rostock, Germany
NdFeB Magnets [$Nd_2Fe_{14}B$]	1.5 mm height, 1.0 mm diameter, N52 strength, Ni-Cu-Ni-Au coating, magnet for external application of a magnetic field	Neomagtec. GmbH Berlin, Germany
NuSil™ MED-2174 Silicone Elastometer	Femoral artery ligation and catheter fixation	Pearsalls Limited Taunton, UK
Ring Holder Titanium	Fixation of mouse skull for imaging	Custom made for fixation of the head during imaging
Tetric EcoFlow	Filling material for metal ring fixation	Ivoclar Vivadent AG Schaan, Principality of Liechtenstein

2.2.4. Pharmaceuticals

Table 5: Pharmaceuticals

Name	**Dose**	**Company**
Flumazenil [0.1 mg/ml]	0.5mg per kg body weight	B. Braun SE Melsungen, Germany
Midazolam [1 mg/ml]	5 mg per kg body weight	B. Braun SE Melsungen, Germany
Naloxon [0.4 mg/ml]	1.2 mg per kg body weight	B. Braun SE Melsungen, Germany
Bepanthen	Ointment manually applied during surgery	Bayer AG Leverkusen, Germany
Isoflurane	1000mg/g per inhalationem	Dechra Veterinary Products Deutschland GmbH Aulendorf, Germany
Atipamezol [5 mg/ml]	5mg per kg body weight	Pfizer Pharma GmbH Berlin, Germany
Fentanyl [0.05 mg/ml]	0.05 mg per kg body weight	Piramal Critical Care Deutschland GmbH Hallbergmoos, Germany
Buprenorphin [0.3 mg/ml]	1:15 diluted to 0.02 mg/ml, 5ml per kg body weight	Schering-Plough New Jersey, USA
Carprofen [50 mg/ml]	1:50 diluted to 1 mg/ml, 75 ml per kg body weight	Zoetis Deutschland GmbH Berlin, Germany
Medetomidine [1 mg/ml]	0.5 mg per kg body weight	Zoetis Deutschland GmbH Berlin, Germany

2.2.5. Software

Table 6: Software

Name	**Usage**	**Company/Developer**
Blender	Inspection and editing of 3D objects	Open-source, general public license;
FIJI = Fiji is just Image J	Image editing	Open-source, general public license;
LabChart 7 Pro	Real-time body temperature measurement during surgery	ADInstruments Inc. Colorado Springs, CO, USA
LAS = Leica Application Suite	Software for LEICA DFC290 HD	Leica Microsystems Wetzlar, Germany
MATLAB	Export of 3D objects as obj. files for inspection and editing in Blender	The MathWorks, Inc. Natick, Massachusetts, USA
Microsoft Office	Word-processing, figure editing	Microsoft Corporation Redmond, WA, USA
Vast Lite	Inspection and analysis of EM-data	Daniel Berger Lab of Sebastian Seung (MIT, USA) Lab of Jeff Lichtman (Harvard, USA)
WaferMapper	EM image acquisition in ATUM-SEM	Hayworth *et al*. (118)
Zen Black	Software for Zeiss LSM 7MP	Carl Zeiss AG Oberkochen, Germany

The list of materials was kindly provided by Maximilian Dorok.

3. Results

3.1. Stroke induction via SIMPLE

Occlusion of blood vessels could successfully be achieved by using SIMPLE combined with a chronic cranial window (39,63). **Figure 1** shows the occlusion of blood vessels after the application of the magnet on a laser speckle flow map and an intensity map. It further demonstrates the development of the occluding MPs and the reperfusion over time. No mortality occurred after the application of SIMPLE on the mouse.

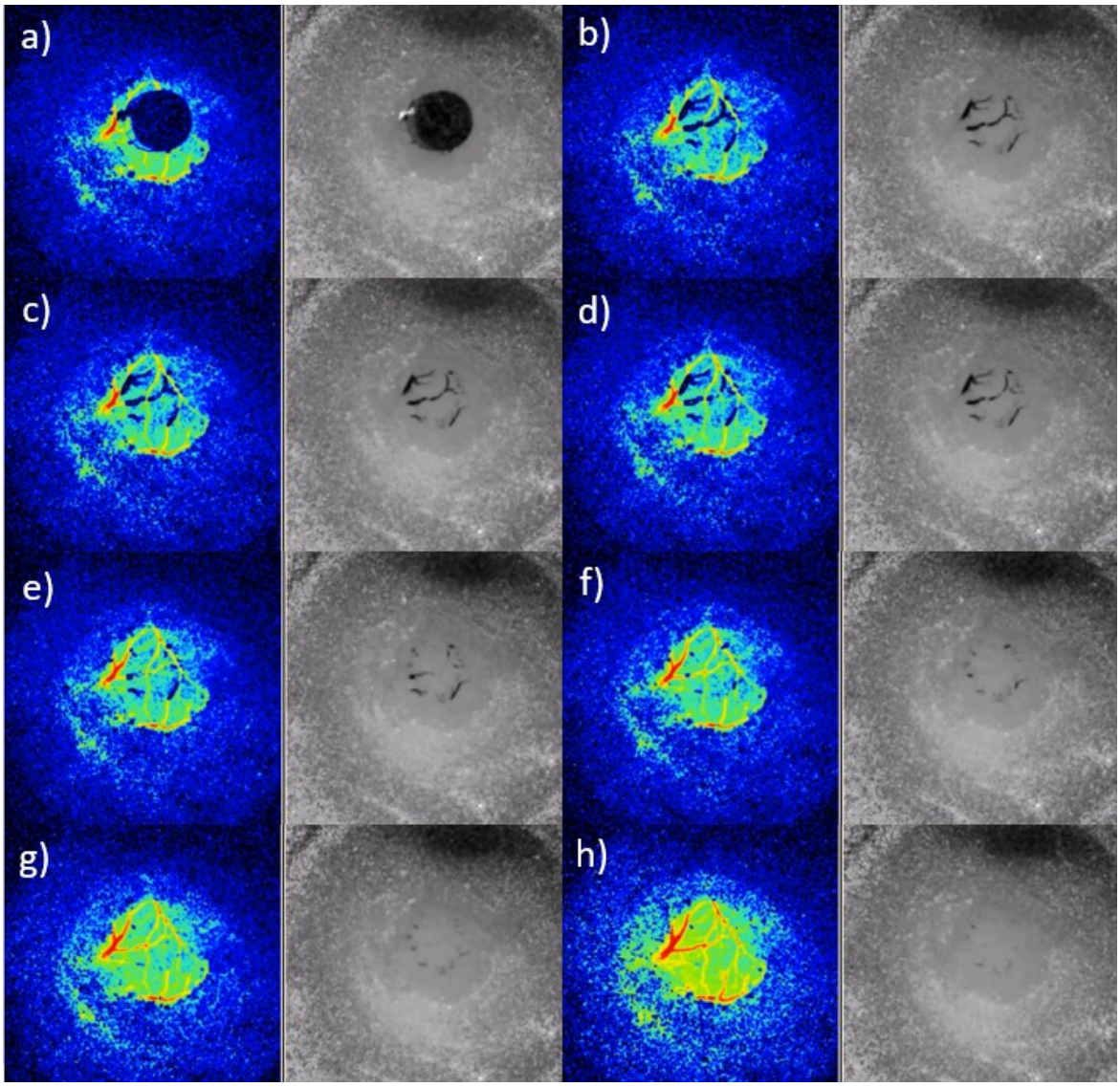

Figure 1: Development of blood vessel occlusion by MPs via SIMPLE. Each time point is represented by 2 images, a heat map, and an intensity map. On the heat map, blue and black colour indicates no blood flow and therefore blood vessel occlusion, whereas red and yellow indicate blood flow. On the intensity map, black

indicates the presence of MPs. **a)** the magnet on the cranial window is visible. **b)** magnet removal after 1 hour of magnet placement. Larger vessels, branches, and smaller vessels at the magnet area are occluded, indicating that the magnetic field applied by the magnet is large enough to affect the MPs. **c)** 30 seconds post removal of the magnet shows no real change in blood vessel occlusion. **d)** 60 seconds post removal some MPs become thinner on the intensity map while the heat map remains dark blue in most areas. **e)** 120 seconds post removal most of the previously large clots start dissolving while blood flow remains mostly silent. **f)** 5 minutes post removal only small, disseminated nanoparticle clots remain and blood flow slowly restores. **g)** 10 minutes post removal increasing red and yellow colour indicates recanalization of most blood vessels. **h)** 30 minutes post removal the red colour becomes very dominant, especially in larger blood vessels and MPs are barely visible in the intensity map.

The images demonstrate that SIMPLE is a viable tool for reproducible, targetable, and simple induction of cortical stroke with reperfusion *in vivo*.

3.2. 2-Photon Imaging revealed MP-clot Formation and Microglial Immune Response after Reperfusion

With the 2P-microscope temporal and spatial information of fluorescent LNPs (magenta) and MPs (white) were acquired. The LNPs are evenly distributed in the blood flow and visualize the blood vessels with high contrast and accuracy. The image from **Figure 2** was taken several minutes after the stroke via SIMPLE. Luminescent MPs can also be observed within the blood vessels. The MPs light up in all excitation channels. Here, the excitation in a green and magenta channel is shown. The merging of all channels creates the white colour of the MPs. The blood vessels in this image are mostly below 30 µm in size.

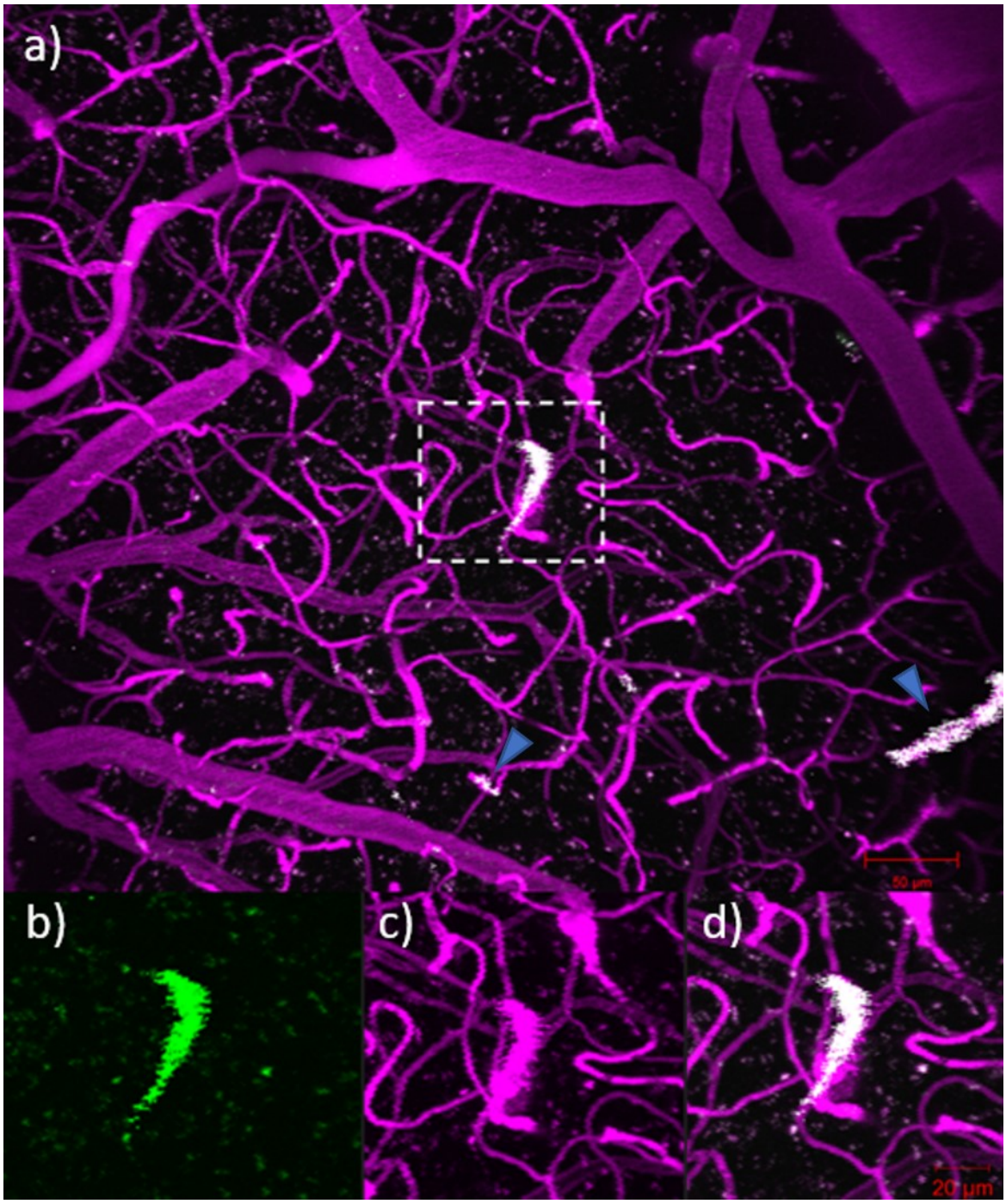

Figure 2: Inspection of IONP/MP clots in the 2P-microscope. A network of blood vessels is visualized by fluorescent LNPs in magenta. Blood vessels of sizes ranging from a few µm up to 30 µm appear, indicating the presence of capillaries, arterioles, and venules. MPs light up in all channels adding up to a white colour and accumulate in vessels of different sizes (►). **a)** shows an overview of the blood vessel network. **b)-d)** show the magnification of a golf club-shaped accumulation of nanoparticles in different colours. The maximum diameter is approximately 15 µm.

Figure 3 illustrates a temporal registration of MPs and microglia post-recanalization. Transgenic CX3CR1-promoter mice expressing eGFP were used to analyse the immune response to ischemia and MPs. Fluorescent LNPs can be seen in magenta and MPs in white. For an hour post-recanalization, multiple accumulations of MPs can be seen throughout the blood vessels (►). This effect mainly occurred in small vessels below 10 µm. The accumulations become larger and brighter at each time point and remain static in the area, indicating microvessel occlusion. Changes in microglial processes can also be observed. The processes extend throughout the tissue and change their formation and direction as time passes, seemingly traveling toward nanoparticle clots. This observation is especially prominent in d).

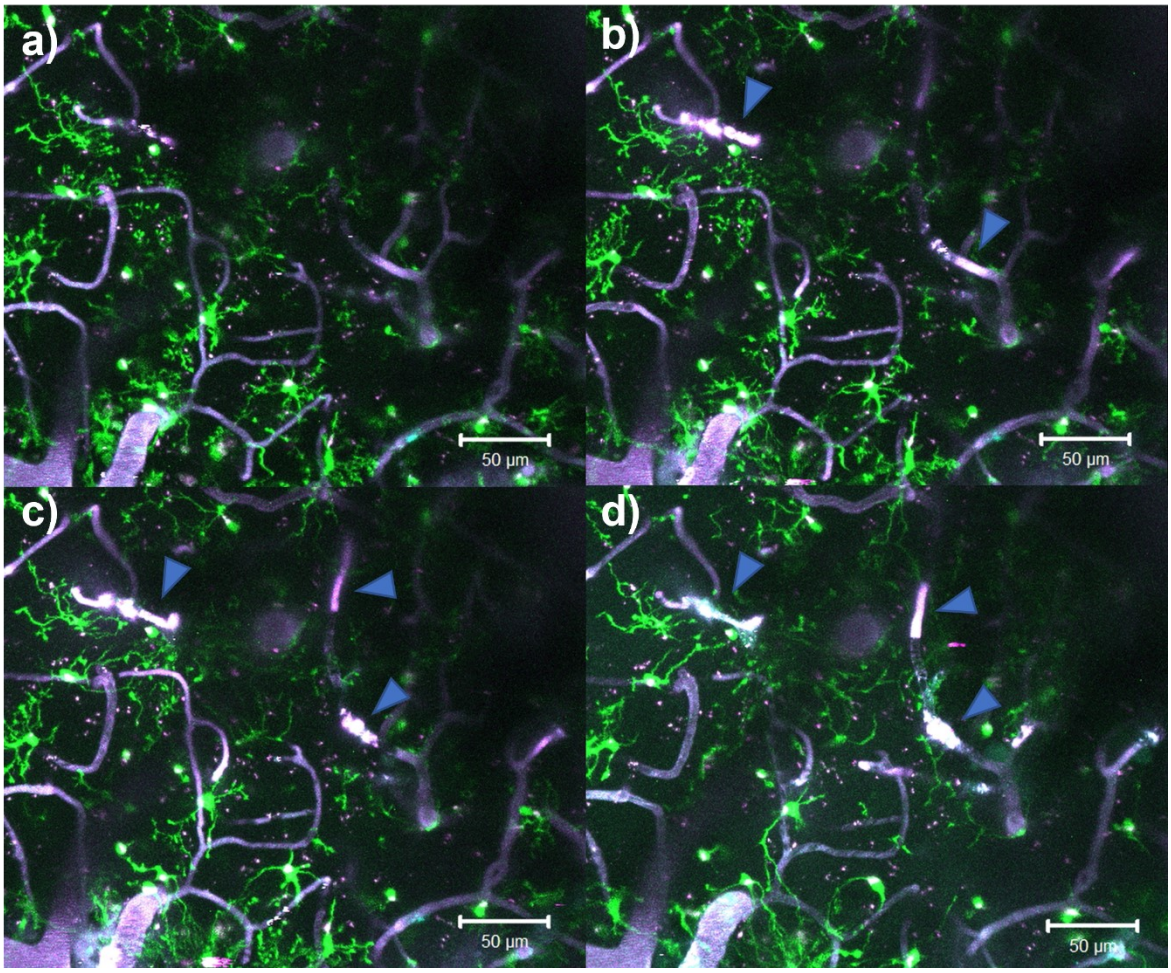

Figure 3: Real-time observation of MP clot formation and the immune response. Blood vessel occlusion in the near vicinity was achieved via SIMPLE a few minutes before. Blood vessels are marked by fluorescent LNPs in magenta. **a)** small numbers of unspecific white dots. **b)** beginning accumulation of luminescent white MPs in small microvessels. **c)** more accumulation of MPs in multiple

microvessels. **d)** stagnating clots of MPs indicating blood vessel occlusion and green microglial processes seemingly reaching out for MP clots. Most of the blood vessels where MP clots were observed ranging from a few µm to approximately 15 µm diameter.

MPs have been visualized in the 2P-microscope (**Figure 2**, **Figure 3**). They can be excited to generate luminescence and appear here in bright white.

3.3. Magnetic Nanoparticles as Correlation Landmarks for Correlative Light and Electron Microscopy

The chronic cranial window was successfully placed on the mouse skull. The window remained clear and provided good imaging prerequisites for 2P imaging. Larger accumulations of MPs were visible to the bare eye through the cranial window. Vibratome sections of the brain and the section identification are shown in **Figure 4**.

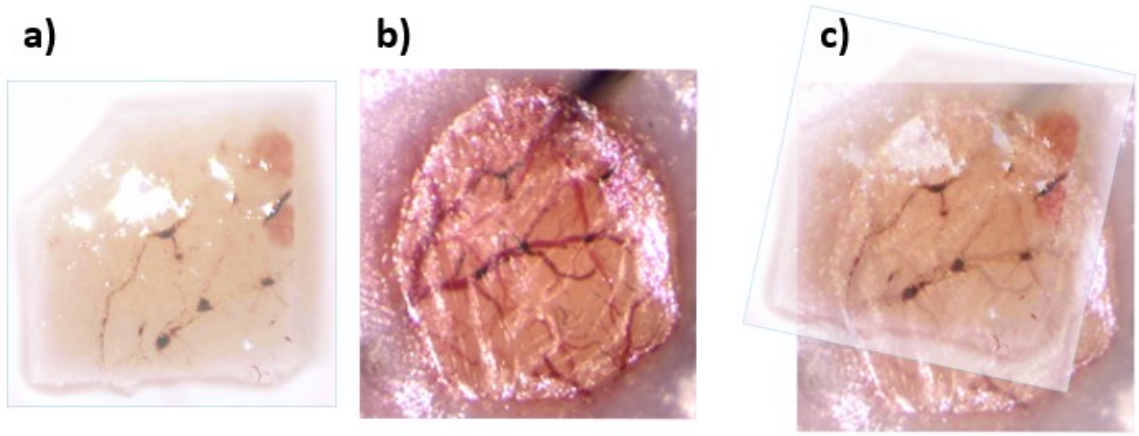

Figure 4: Sample preparation for CLEM. **a)** shows a 300µm thick brain section created by the vibratome. MPs are visible as dark spots. **b)** view of the chronic cranial window with MPs visible to the bare eye. **c)** section identification in preparation for ultramicrotome sectioning for ATUM-SEM imaging.

Figure 5 shows LM and EM images of the same brain section. In both imaging modalities, the MPs could be easily identified. Accumulations of MPs identified by the SEM are marked as blue squares. In combination with the ATUM-SEM protocol developed by Hayworth *et al*., MPs could be used as correlation landmarks for CLEM (118).

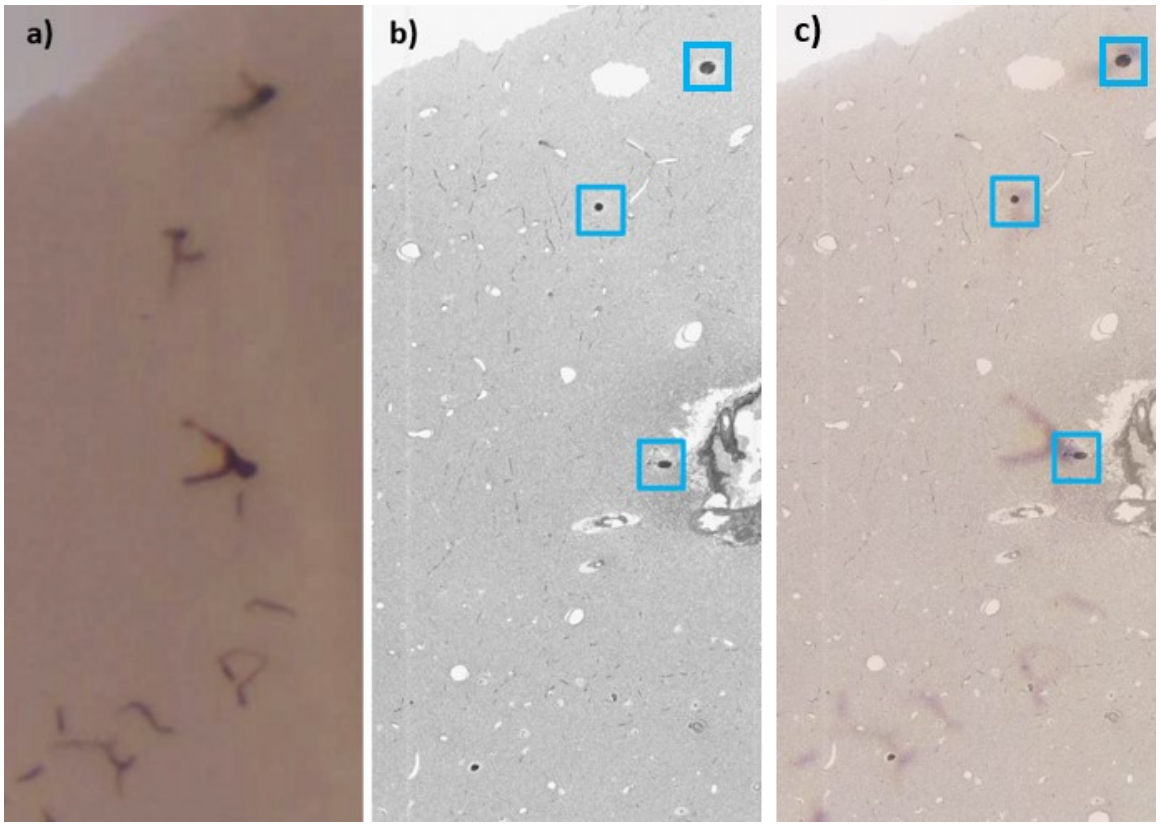

Figure 5: LM and EM images of brain sections for CLEM. a) In the LM image the parenchyma is homogenous, and MPs can be identified as groups of black substances. The rough shape of blood vessels can also be seen through MPs. **b)** in the EM image MPs are also identified by their deep black colour. After fixation, the blood gets washed out, but MPs remain. **c)** shows the merged image of LM and EM. MP spots are used as correlation landmarks for CLEM.

Using the 2P-microscope, a blood vessel occluded within an hour post reperfusion was found (**Figure 6**). MPs were not inside the vessel of interest, but accumulations of fluorescent LNPs indicated blood vessel occlusion. Furthermore, EM images of LNP accumulations in a clot could reveal information about the dynamics of LNPs in occluded blood vessels. A group of MPs (►) was found in the close vicinity, which was used as a correlation landmark for CLEM. The microvessel in the ROI (□) splits into 2 branches, a straight branch and a curved one. In the straight branch, the signal intensity of LNPs is double-sided. For the longer part of the vessel, signal intensity is increased, indicating the accumulation of LNPs. A shorter part of the vessel is completely dark, with no signal at all, indicating the formation of a clot. In the bottom right corner of the image, a group of MPs can be observed. They appear

as scattered small dots suggesting an extravascular location. Nonetheless, they can be used as correlation landmarks for CLEM.

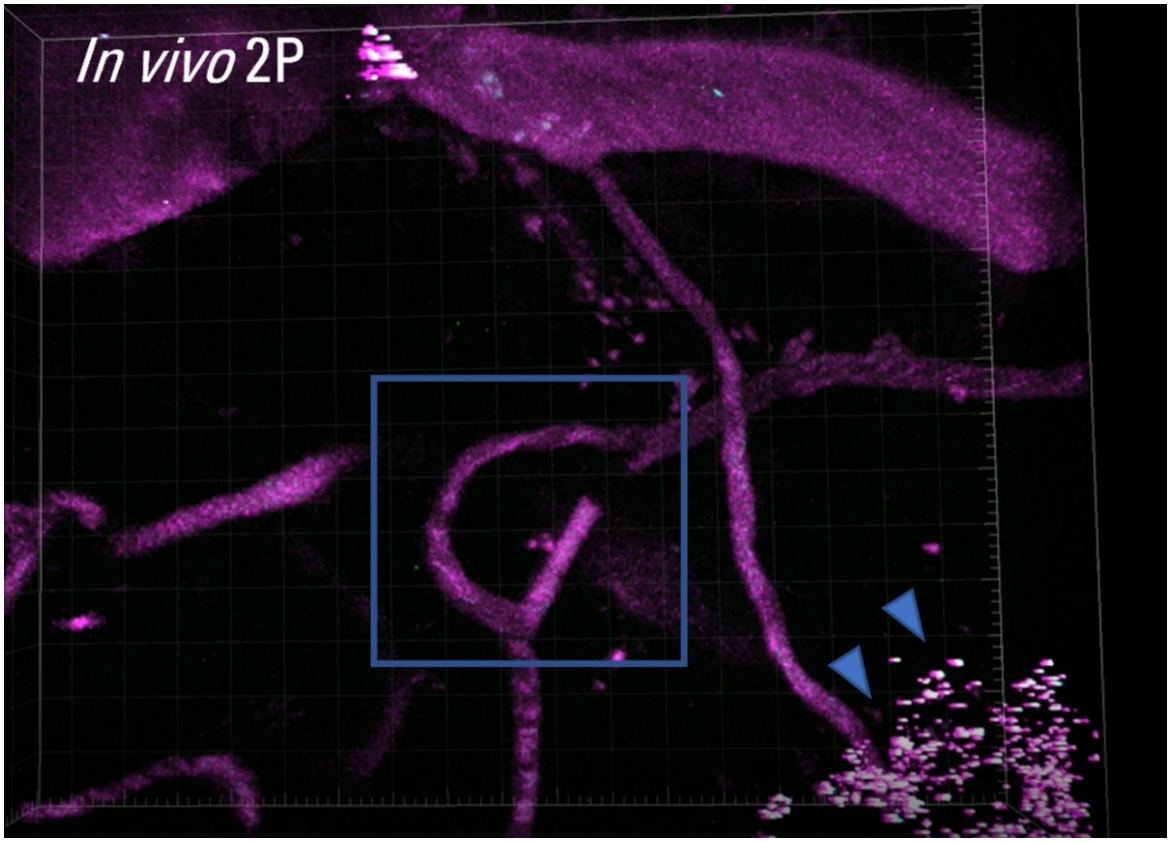

Figure 6: *In vivo* 2P image of the mouse cortex: Fluorescent LNPs appear in magenta and MPs (▶) in white.

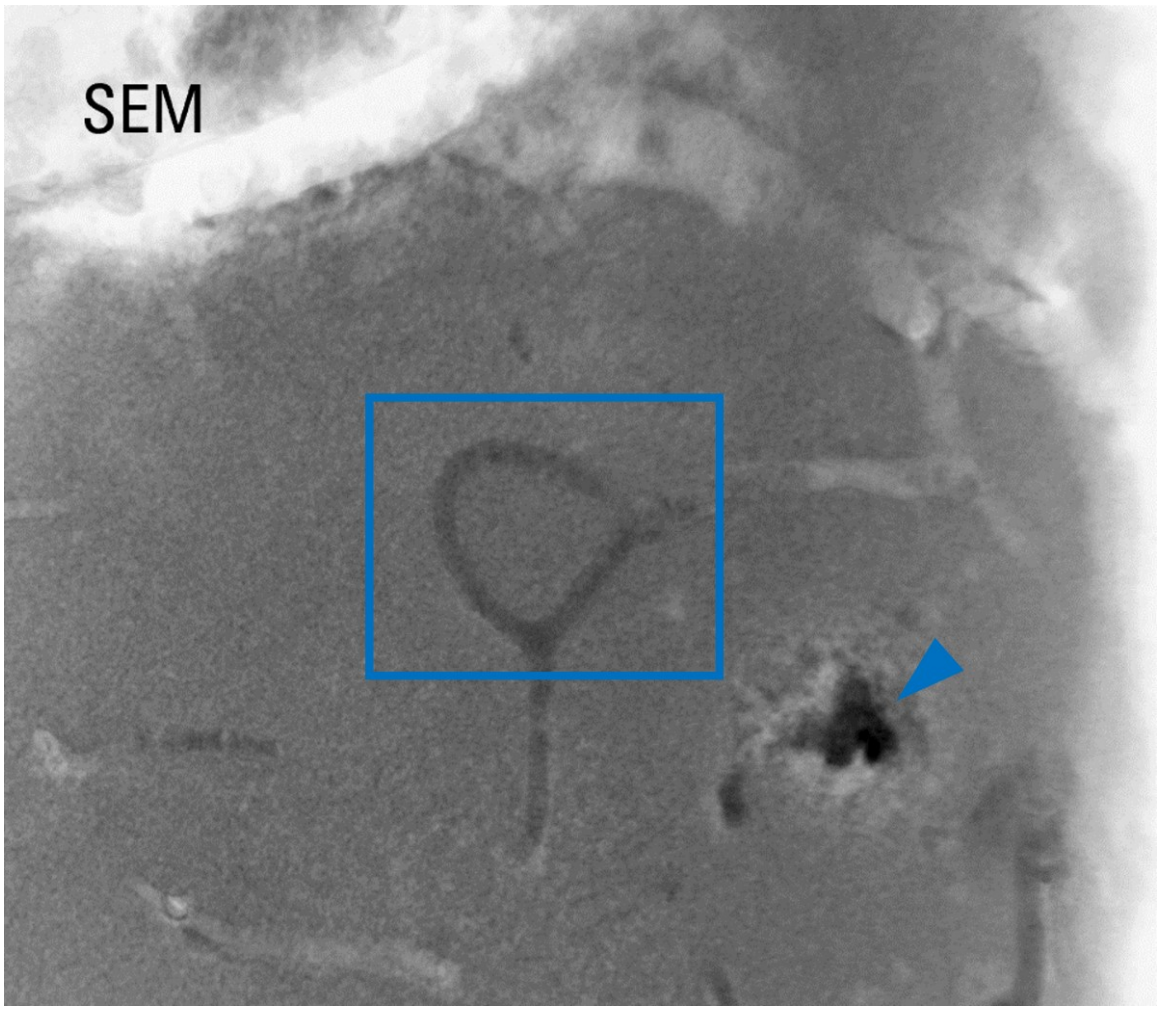

Figure 7: Low-resolution SEM overview image in preparation of high-resolution ATUM-SEM imaging.

In **Figure 7**, the same ROI (□) is demonstrated as in the 2P image (**Figure 6**). The location was found based on the MPs on the bottom right (►). The content of the microvessel has a slightly different electron density than the tissue around it. LNPs have been seen in EM before, so the difference in electron density may derive from accumulating LNPs (98).

3.4. EM-Inspection revealed MP-Clot Formation, Microcirculatory Disruption, Cellular Changes, and Extravasation of Lipid Nanoparticles

3.4.1. MP-Clots aggregate and undergo Phagocytosis

Aggregations of extravascular MP-clots were imaged and inspected with a resolution of 4nm x 4nm. **Figure 8** shows a cluster of MPs with approximately 8 µm

diameter. The electron density of MPs is very high, therefore they can be easily identified and separated from other structures.

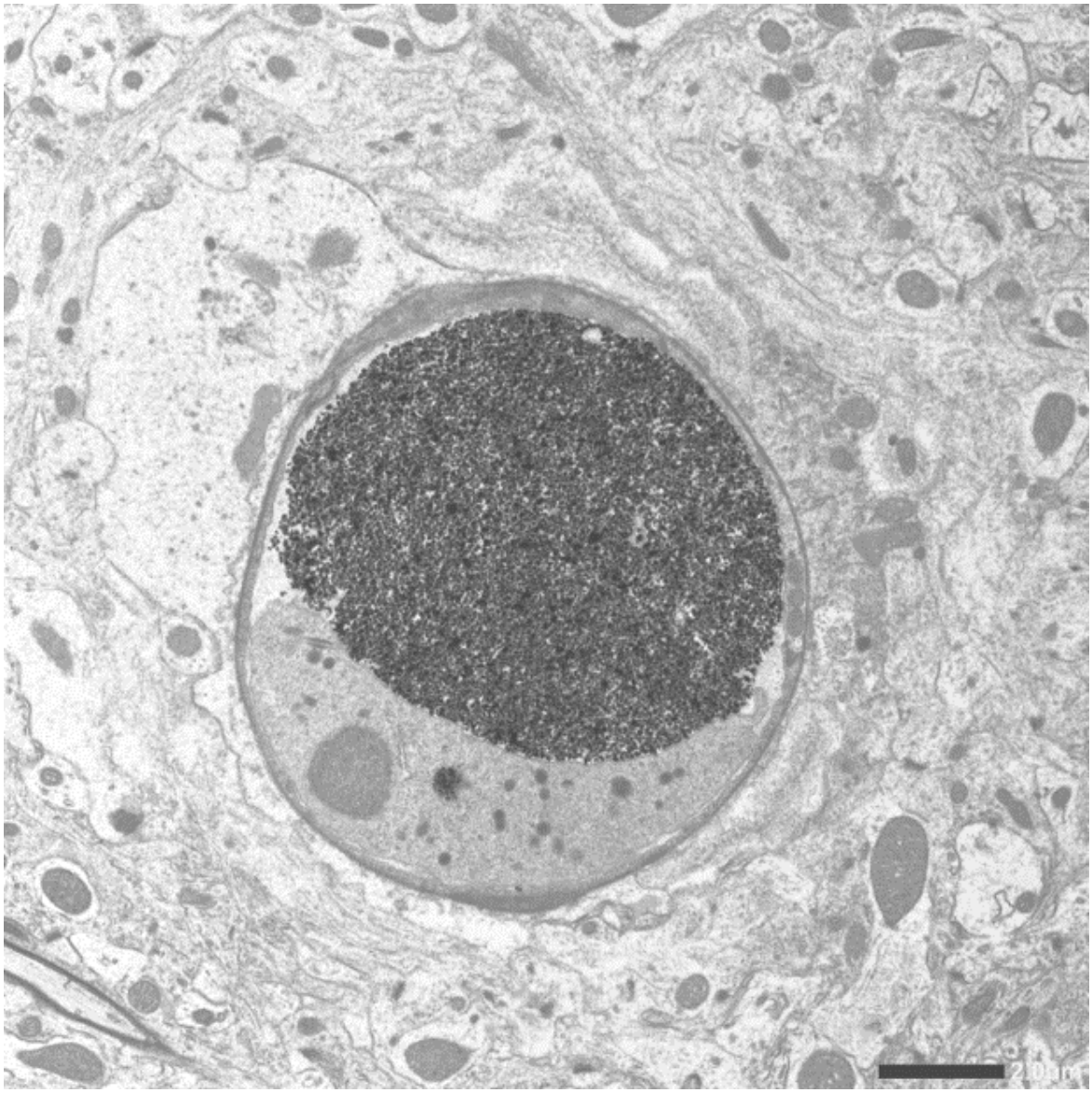

Figure 8: EM image of an encapsulated MP-clot. Resolution: 4nm x 4nm.

The MPs are encapsulated inside a cell with relatively dense cytoplasm and lysosomes, most likely a microglial cell. Surrounding it is a structure with very low electron density, small dust-like dots (cross-section of microtubules), and few organelles. The location and morphology fit an astrocyte process, potentially an astrocyte end foot (127).

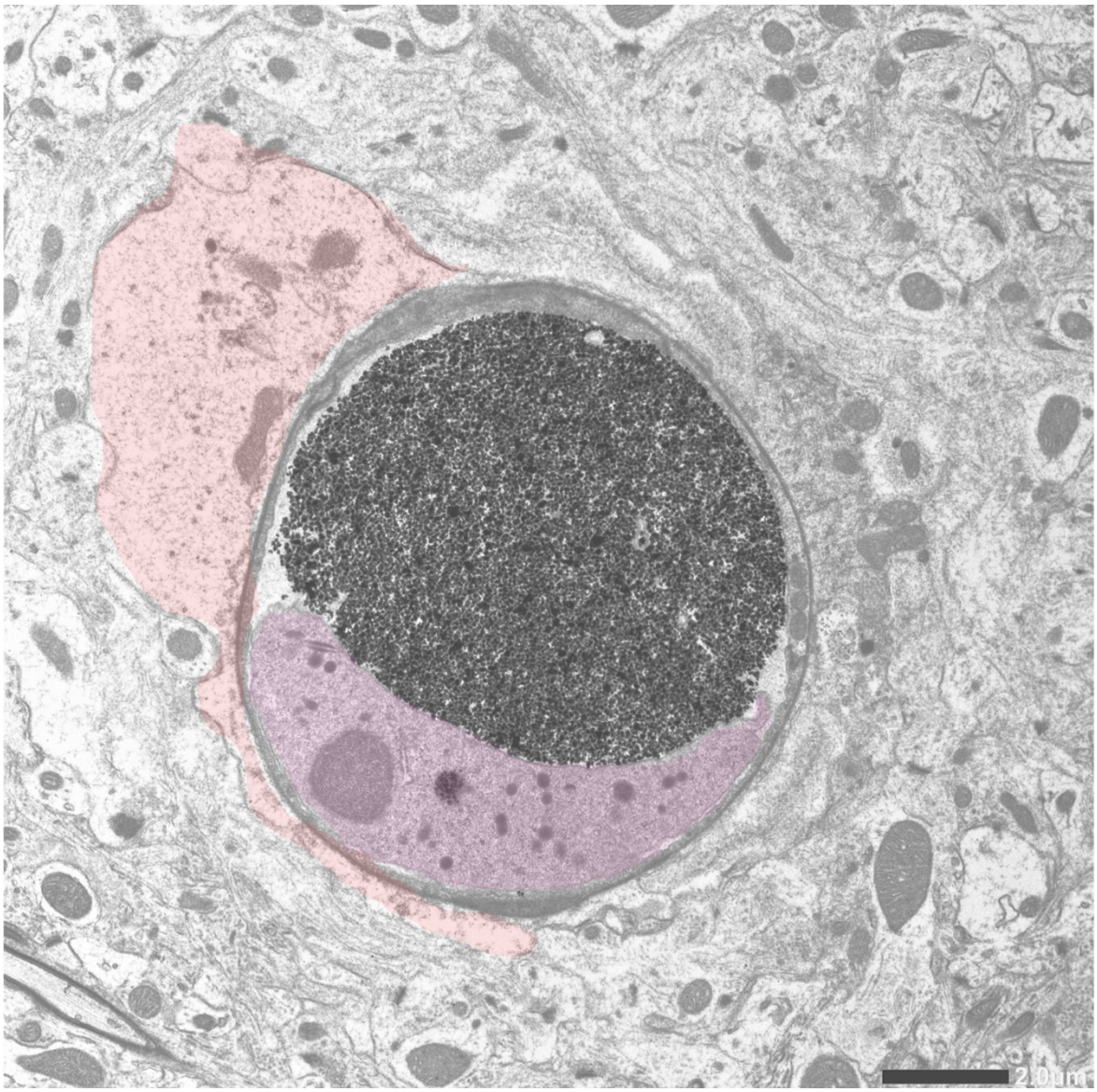

Figure 9: Microglia encapsulating MPs, surrounded by an astrocyte process.

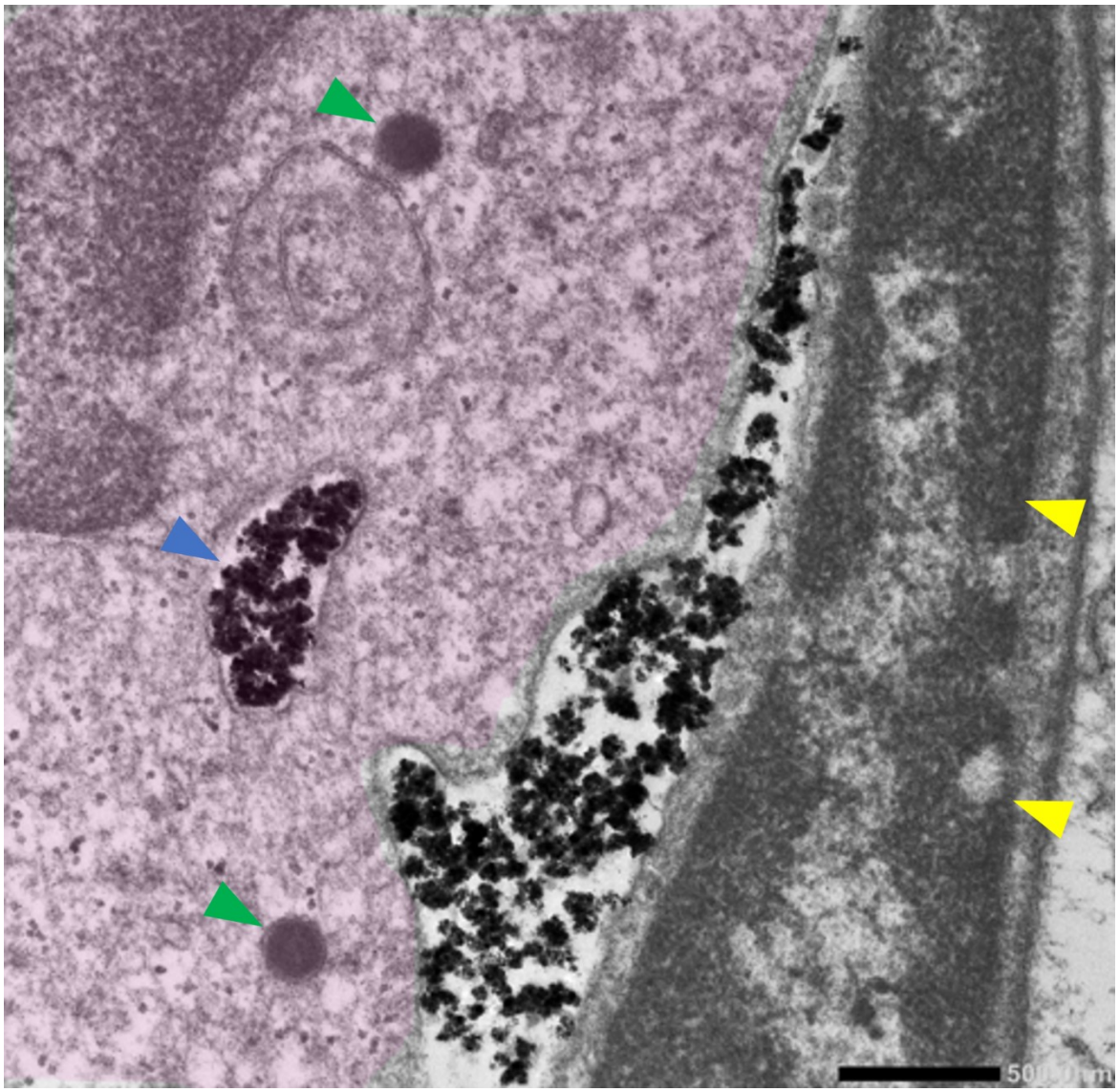

Figure 10: Close-up inspection of MPs in phagocytosis. ▶Endosome with MPs. ▶Primary Lysosomes. ▶Microglial Nucleus

A closer inspection of the microglia in a different slice reveals phagocytic processes. An oval endosome with approximately 700nm length and 200nm width and MPs inside (▶) can be observed. Two circular-shaped structures can be identified in the area, with very electron-dense content (▶). These could be interpreted as small primary lysosomes, due to their small size (approximately 200nm diameter) and rather homogenous content. The microglial nucleus that can be seen on the right side (▶) is flattened and has rich peripheral heterochromatin.

3.4.2. EM-Resolution and Mip-Levels

After *in vivo* imaging with the 2P-microscope, an EM z-stack of 254 images was created with an XY-resolution of 4nm x 4nm and an axial resolution (slice thickness)

of 100nm. 254 TIF-files with 1GB each were converted to a single VSV-file for inspection.

The resolution remains high as the image is zoomed in. Texture mip-levels range from 6 to 0, with 6 being the maximum overview and 0 being the maximum zoom. Mip level 0 represents the original resolution with pixels of 4nm x 4nm. As mip-levels progress, the image is built from half the pixels for each step, resulting in 8 nm x 8 nm for mip-level 1, 16 nm x 16 nm for mip-level 2 and so forth. **Figure 11** illustrates the progression of the level of detail with increasing zoom and mip-level.

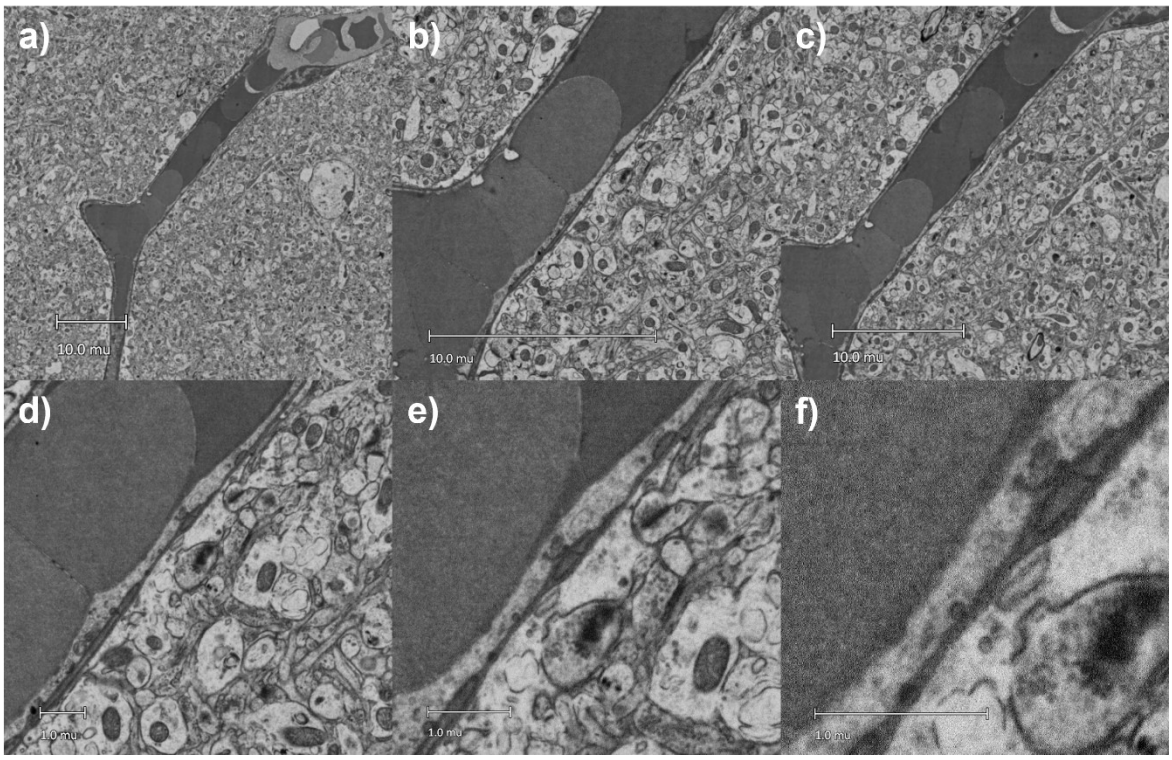

Figure 11: Mip-Progression with increasing zoom. a)-f) represent mip-levels 5)-0). 1mu ≙ 1µm. The textures remain smooth as the image is zoomed in. At mip-level 0 single 4 nm pixels start becoming visible. The resolution is sufficient to identify subcellular structures such as mitochondria, synapses, synaptic vessels, endoplasmic reticulum, GCs, etc.

3.4.3. Erythrocyte Morphology Changes

Usually, vessels are empty in EM-inspection because the blood gets washed out during sample preparation. Here, different blood elements remained, most likely because the clot prevented washing out during fixation. Therefore, erythrocytes and other blood components can be inspected and analysed. Multiple erythrocytes can

be seen stacked next to each other (**Figure 12**). This suggests that a mechanical barrier blocks blood flow.

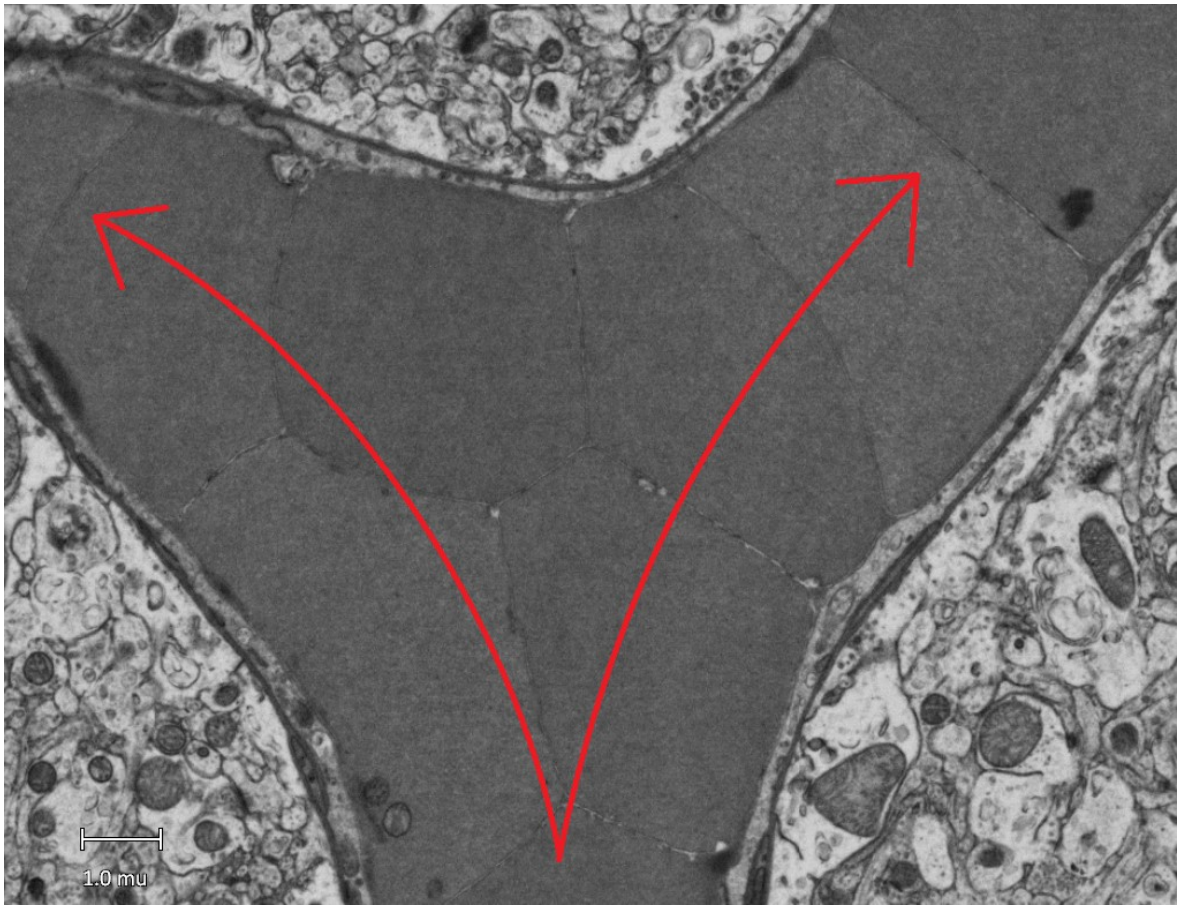

Figure 12: Stacked Erythrocytes. → red arrows show the direction of blood flow. Erythrocytes are closely cramped next to each other and show relatively high electron density. Very thin lines in between the membranes make single erythrocytes still distinguishable from one another.

An overview of erythrocytes reveals the formation of vacuoles (►, **Figure 13**). It is noticeable that the distribution pattern is strictly in the periphery of erythrocytes. A closer inspection of erythrocyte vacuoles shows that the vacuoles are not intracellular, but rather invaginations of the outer erythrocyte membrane. This effect also called membrane internalization has been described before by Ben-Bassat *et al*. They suggested an ATP-dependant shift in calcium and magnesium homoeostasis as the underlying mechanism for membrane internalization (144).

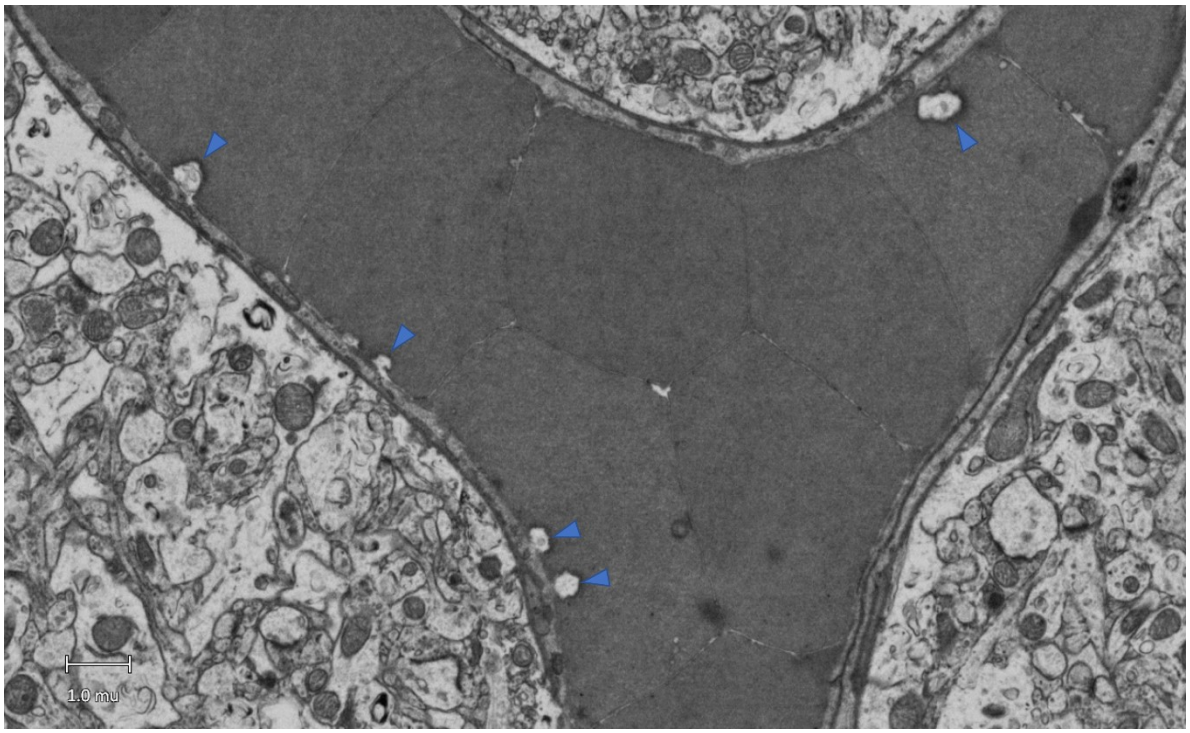

Figure 13: Overview of erythrocyte vacuoles.

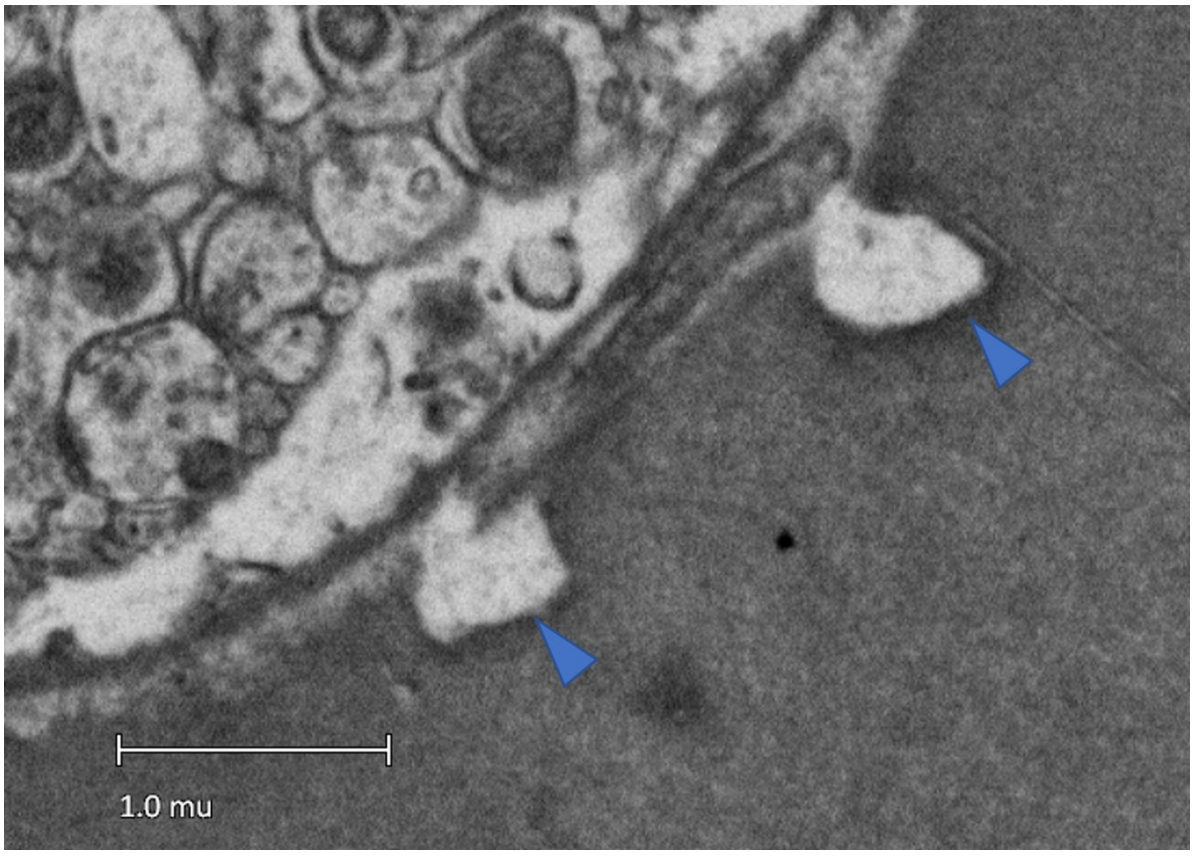

Figure 14: Membrane internalization of erythrocytes

In the area after the clot, erythrocytes look very different than the ones just described, losing most of their original shape. The emergence of polyhedral erythrocytes or polyhedrocytes has been analysed thoroughly by Tutwiler *et al*. They analysed shape changes of erythrocytes going through mechanical pressure delivered by clots, platelets, and thrombin and coined the phrase piezocytes. Piezocytes include all deformations of erythrocytes after mechanical pressure. The cytoskeleton of erythrocytes is very flexible, making it possible for them to change their shape to adapt to different mechanical obstacles. This effect also occurs to a smaller degree when erythrocytes need to squeeze through capillaries. It is important to note that neither the surface area nor volume of the erythrocytes change during the process, only the shape (145,146).

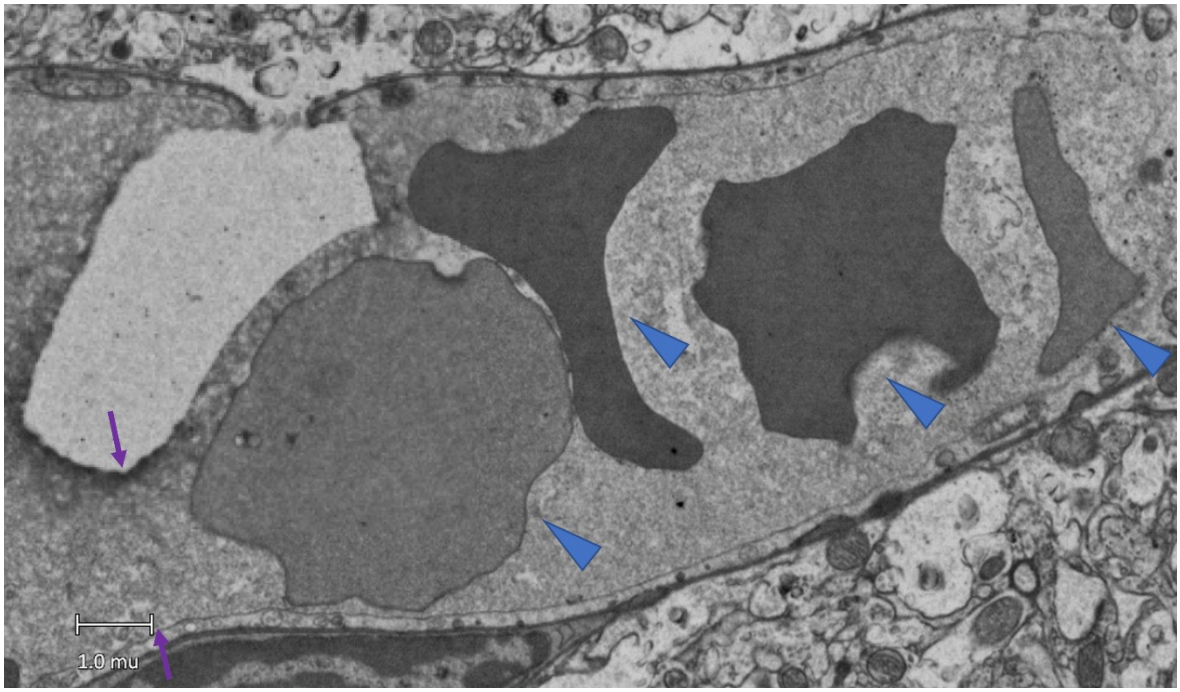

Figure 15: Distorted erythrocytes after mechanical barrier. The erythrocytes (►) have undergone drastic changes in their shape. In the area before the erythrocytes, the blood vessel is massively constricted, creating a very narrow passage for erythrocytes (→). The erythrocytes post constriction observed here do not possess vacuoles.

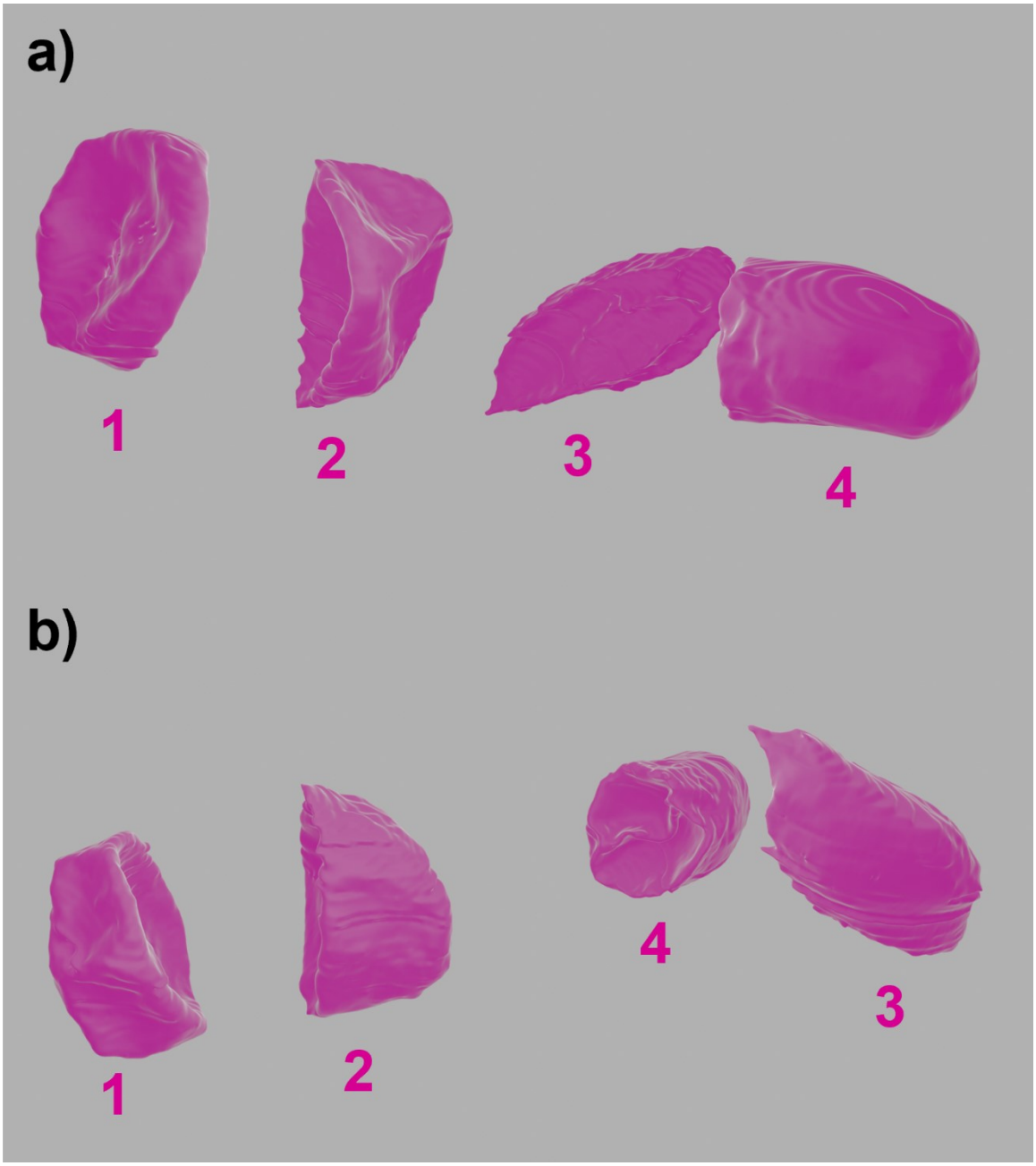

Figure 16: 3D Reconstruction of distorted erythrocytes. This 3D reconstruction further demonstrates the distorted shape of the erythrocytes. **a)** and **b)** show different views of the same erythrocytes. The corresponding cells are numbered from 1-4. Numbers 1 and 2 belong to the group that passed through the constriction. Numbers 3 and 4 belong to the stacked erythrocytes that are coming from the 2 influxes and have not squeezed through yet. The erythrocytes are deformed, and the usual biconcave symmetrical structure is completely lost. Erythrocytes 1 and 2 both have multiple concavities when inspected from both sides. Numbers 3 and 4 have rather convex surfaces. Erythrocyte 3 is flat on one side and convex on the

back side with no concavities at all. Number 4 is ovoid, elongated, and mostly convex. One side of number 4 contains a concavity that is split into two halves. This reconstruction demonstrates how the pressure from stacking erythrocytes before the constriction changes them to take on a convex, spheroid surface. In the process, they change their shape to concave, flat structures to fit through the constriction.

3.4.4. Endothelial Cells and Intact Tight Junctions

A total of 4 endothelial cells have been identified by their location as the innermost lining of the blood vessel and flat structure as well as the nucleus. Pericytes are distinguishable from endothelial cells by their basic structure with multiple primary and secondary processes and by a basal lamina lining on all sides (127).

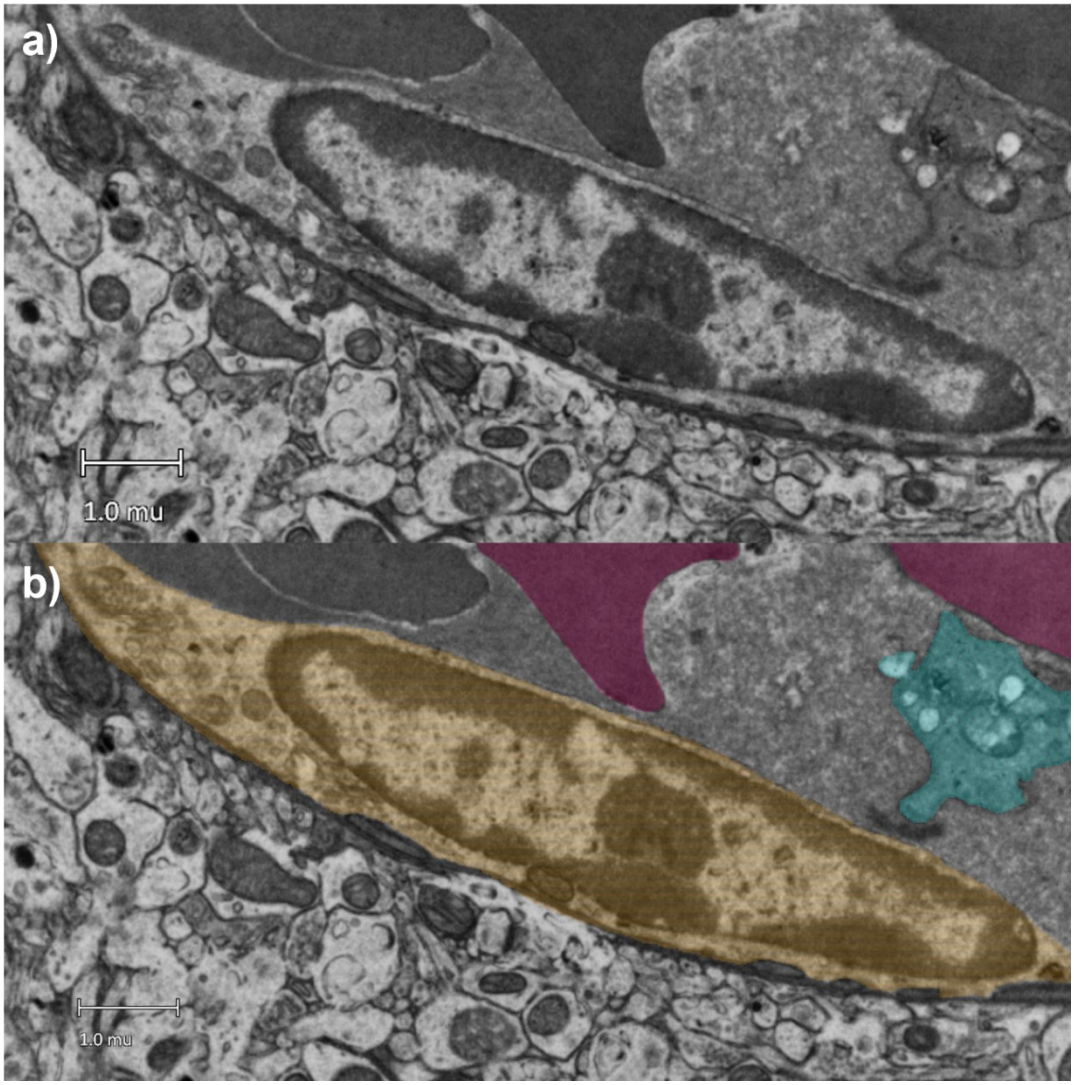

Figure 17: Slice of an endothelial cell. a) shows the raw image and b) adds segmentation of the endothelial cell, erythrocytes, and a platelet. The endothelial cell is the innermost lining of the blood vessel and has a flat form. The nucleus is

also flattened. Immediately next to the endothelial cell is blood content and no basal lamina can be identified, ruling out a pericyte.

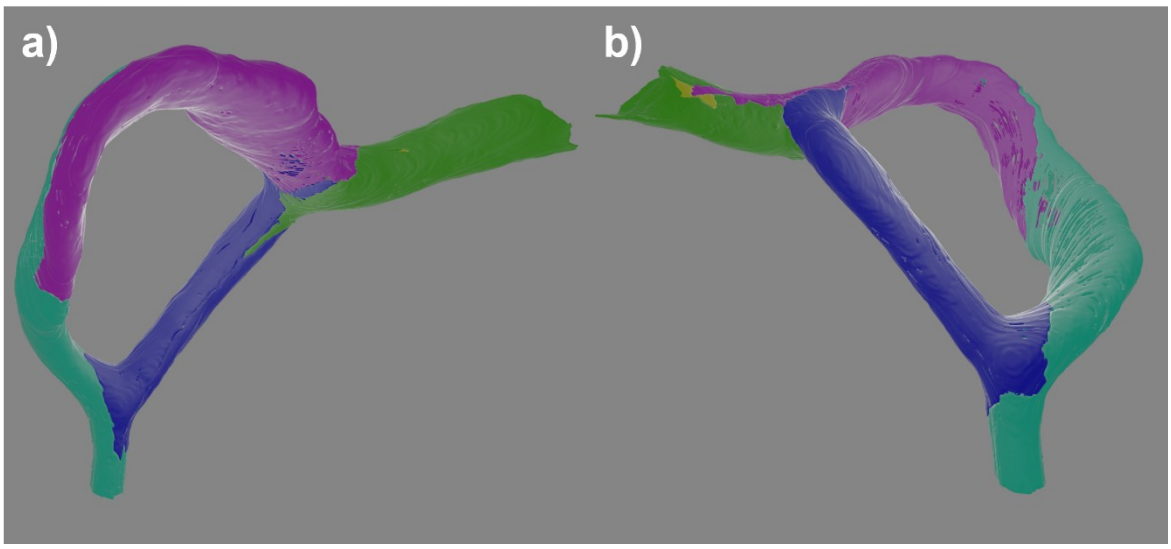

Figure 18: 3D image of endothelial cells. Each colour represents an individual endothelial cell. The vessel is the same in both images, with **a)** representing the front view and **b)** the back view. The small yellow area that can be seen in b) is most likely the edge of another endothelial cell, which barely reached the z stack in the last slices. The turquoise and magenta cells appear to have slits in their wall in this 3D image. This is because the 2D segmentation was done at the highest resolution in mip-level 0, but exporting the 3D object was done on mip-level 2 to minimize processing power requirements and time. Therefore, since mip-level 2 computes only 16 nm pixels instead of 4 nm, wherever the endothelial cell becomes very thin, fine segmentation elements smaller than 16 nm are skipped in computing the 3D object. In the raw EM images, the cells have been inspected at all levels and no slits or other membrane defects could be identified except for the hole described in “3.4.5 Vessel Constriction”.

2 tight junctions were identified in the z-stack. They extend from processes of 2 endothelial cells each on both ends, traveling very closely along the wall of a third endothelial cell.

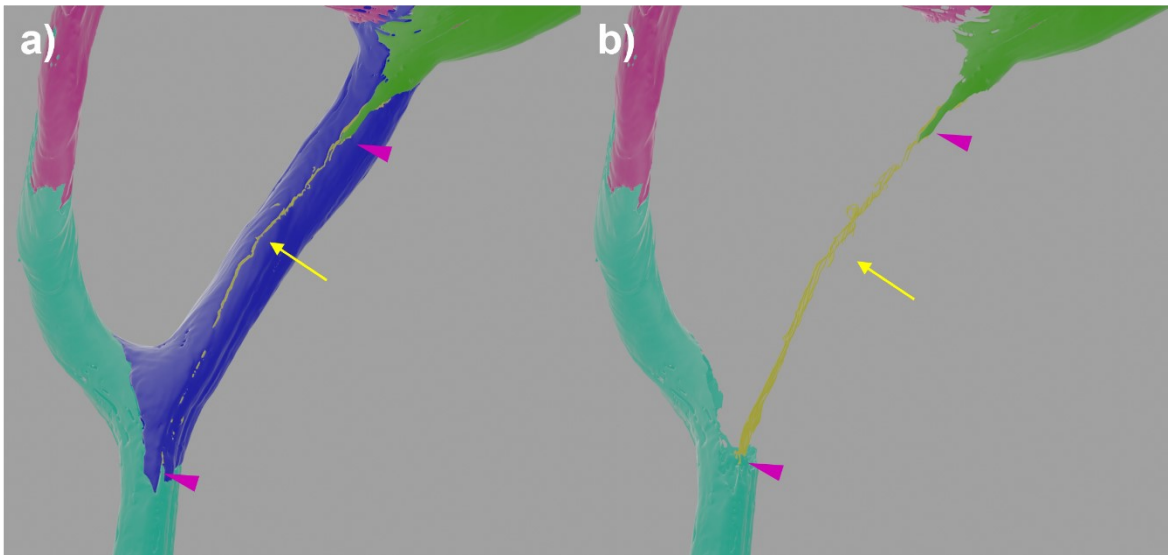

Figure 19: Tight junction 1. The tight junction (→) stretches out from processes (►) of the green and turquoise endothelial cells across the membrane of the blue cell. They function as extensions of the cell membrane in between endothelial cells to give the whole endothelial structure more stability. In a) it seems as though the tight junction is not continuous. Some pixels of the tight junction segmentation were not acquired during 3D export due to its fine structure, as explained in **Figure 18**. In b) the blue endothelial cell is masked, revealing a more detailed progression of the tight junction with no discontinuities.

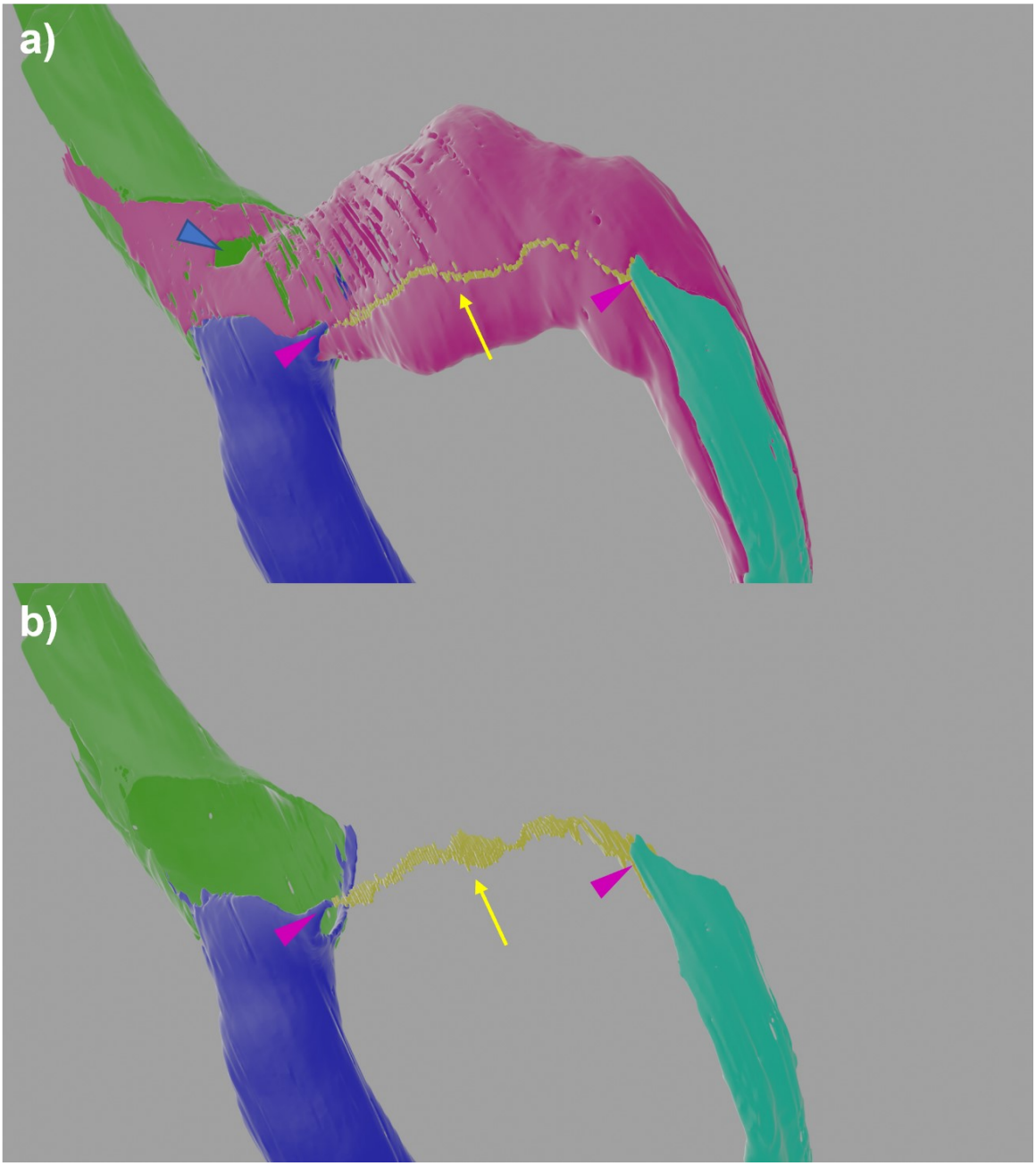

Figure 20: Tight junction 2. Tight junction (→) extending from the turquoise cell process to the blue cell process across the endothelial cell membrane. Slits in the endothelial cell membrane are due to pixel loss effects in 3D exportation (see **Figure 18** for an explanation), but no actual slits were seen in the raw EM data. The hole in the cell, causing the intrusion of extravascular content and the constriction can be seen here as well (►). The tight junction is continuous and not associated with the hole in the endothelial cell.

3.4.5. Vessel Constriction is Caused by Astrocyte Invasion through a Hole in an Endothelial Cell

In the area where the two branches of the vessel meet, a massive constriction of the vessel can be observed. The erythrocytes before the constriction stack (**Figure 12**), whereas those post constrictions show severe shape distortions (**Figure 15**), indicating active stenosis of the vessel with potential disruptions in microcirculation. Producing the occlusion is an infolding structure with very light electron density, several small dark dots, and content invading from the extravascular area.

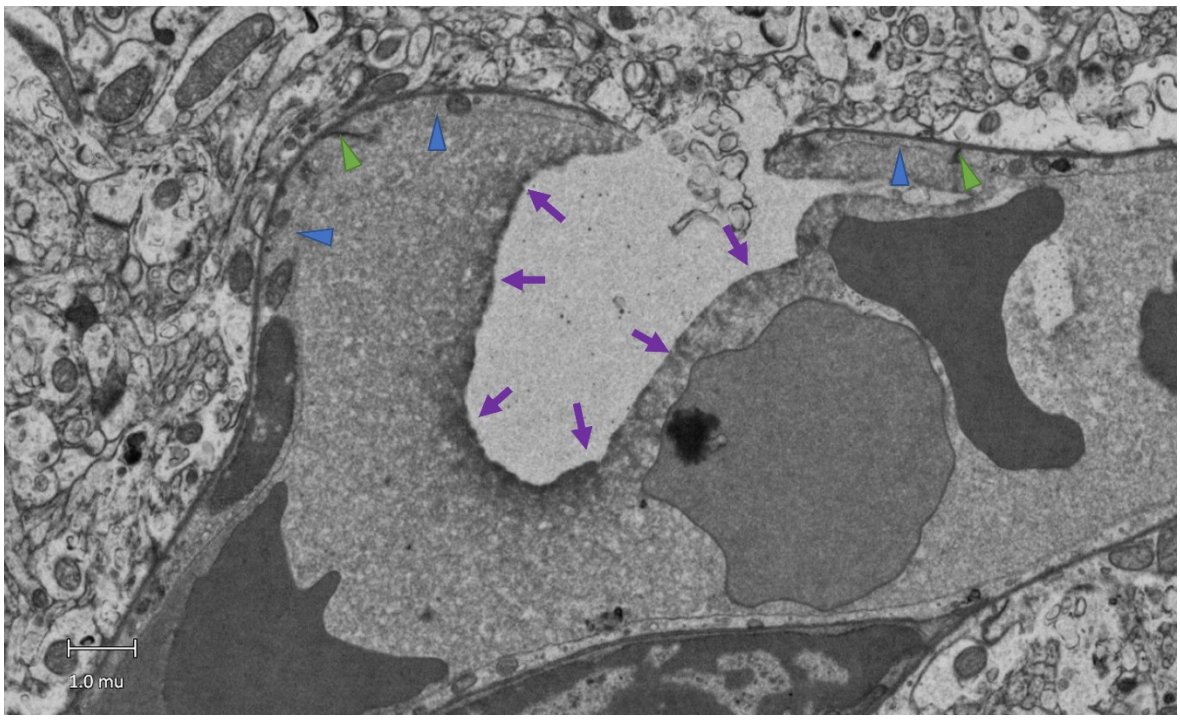

Figure 21: Overview of vessel invagination disrupting blood flow. The content of the infolding structure is reminiscent of astrocyte cytoplasm or processes, with low electron density and microtubules appearing as small dots. There is a clear separation between the invagination and the vessel content (→). Endothelial cells (▶) and intact tight junctions (▶) can be identified. The tight junctions were trailed from beginning to end and no disruptions in tight junctions could be discovered. A closer look at the endothelial cells reveals that no tight junctions are involved in the disruption of vessel integrity but rather a hole in the erythrocyte membrane, which allows the astrocyte end foot-like structure to intrude. This observation could give hints about possible mechanisms for microcirculation disruption, BBB changes after stroke and no-reflow, but it could also be an artefact of sample preparation or 2P imaging. The cause of the vessel invagination remains unclear.

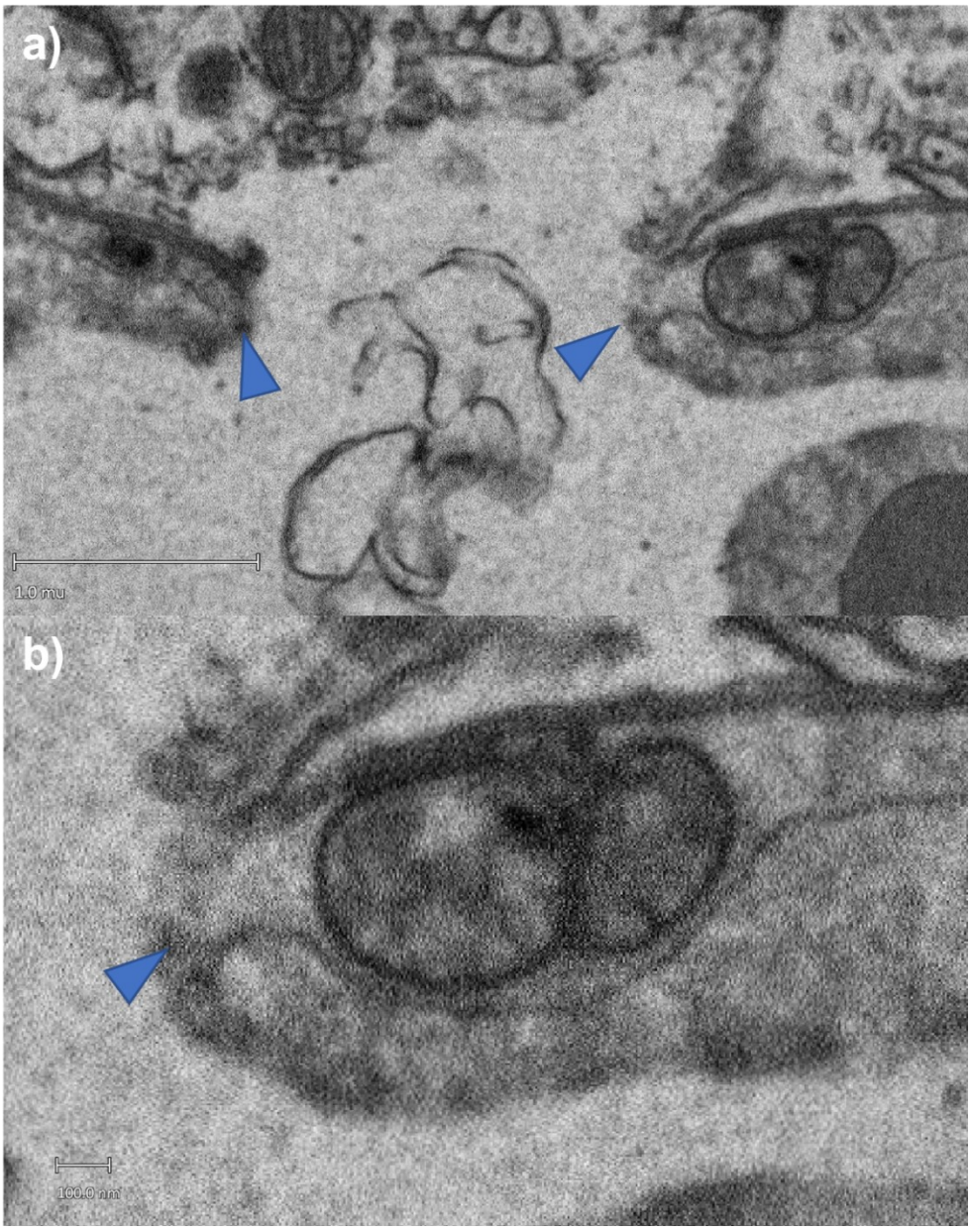

Figure 22: Close inspection of vessel invagination. a) shows a view of both sides of endothelial damage. Trailing the whole expansion of both sides through the z-stack reveals that they are two sides of the same endothelial cell. This is in accordance with the 3D reconstruction of the endothelial cell. No tight junctions are involved in the opening of the endothelial cell. b) is a high-zoom picture on mip-level 0 which demonstrates the loose and open end (►) of the endothelial cell.

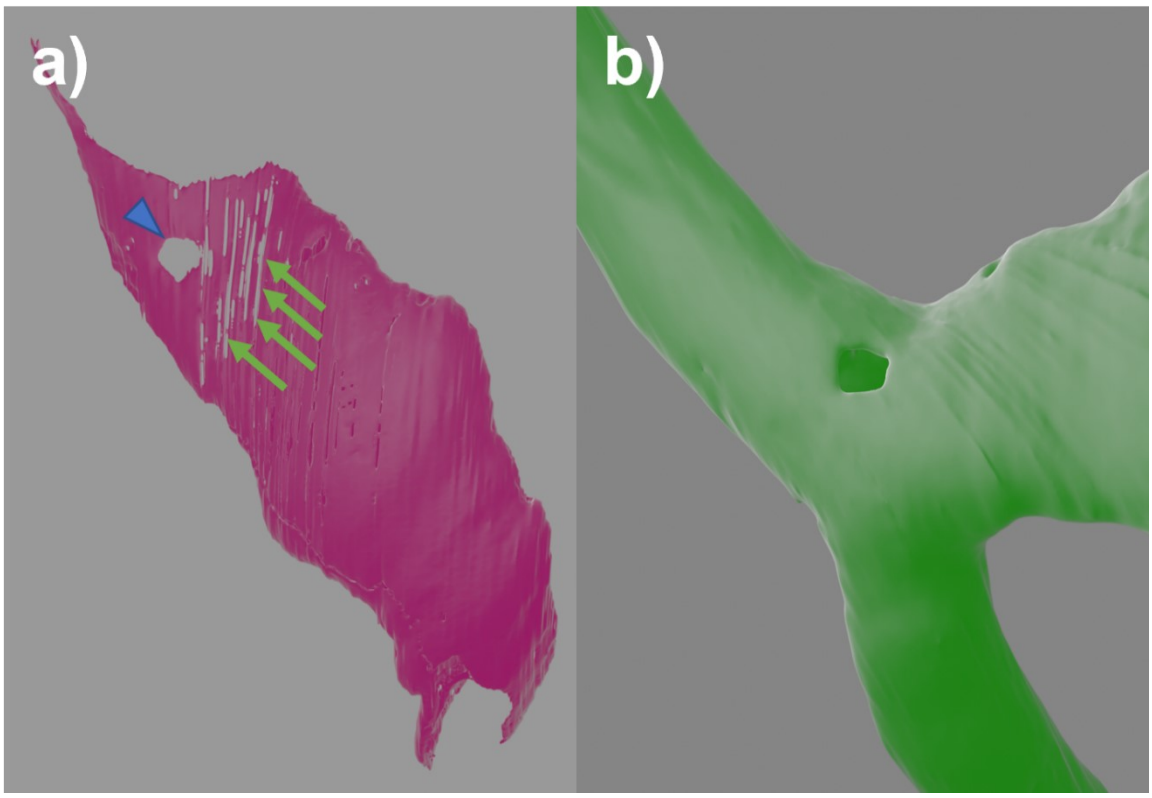

Figure 23: Damaged endothelial cell in 3D. The slits (→) in the endothelial cell in **a)** are the results of pixel losses in thin segmentations and not actual slits in the endothelium (see **Figure 18** for a detailed explanation). To alleviate this effect the vessel has also been reconstructed as a whole and is demonstrated in **b)**. The disruption that can be seen in the 2D images (**Figure 21**, **Figure 22**) is pictured in this image as well (►). It appears as a round-shaped hole in the endothelial wall. Neither tight junctions nor other endothelial cells relate to the hole. The origin remains unclear.

3.4.6. Pericyte Morphology and Interaction with Endothelial Cells

A single pericyte was identified in the z-stack. The pericyte here has 4 large branches with 3 being long and 1 short. The long primary branches send out numerous secondary processes enveloping the vessel. The pericyte sits directly beyond the endothelial cells and has a basal membrane lining.

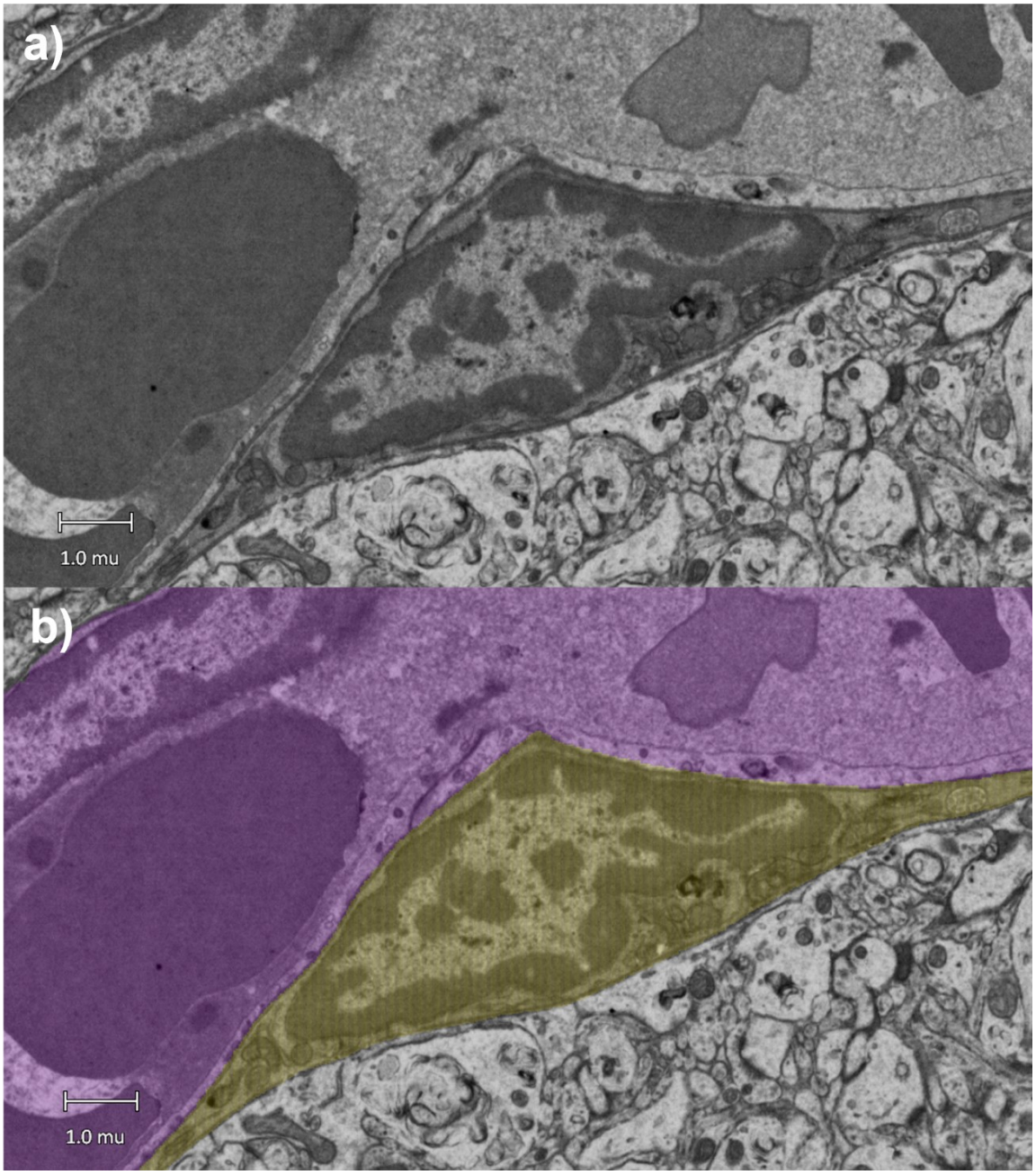

Figure 24: Pericyte perikaryon and nucleus. The pericyte cell body has a triangular shape with the nucleus adapting the same form. It sits on top of the vessel and has relatively darker cytoplasm compared to the endothelium, in contrast to usual pericyte descriptions (see “1.8.5 Endothelial Cells and Pericytes”) (127).

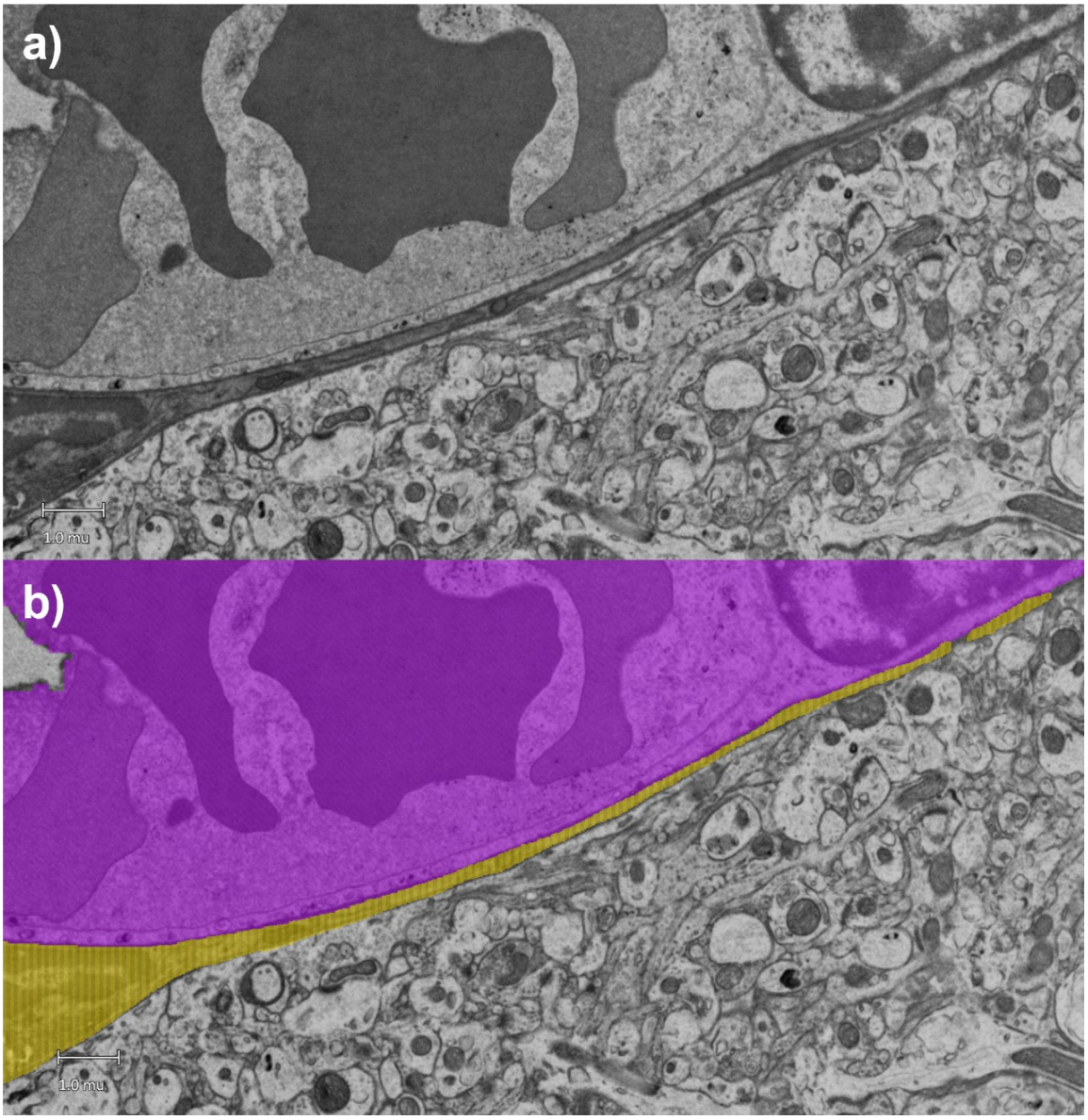

Figure 25: Pericyte process. The pericyte process can be followed using the basal membrane and the higher electron density as criteria. This makes it easy to separate the pericyte from the vessel.

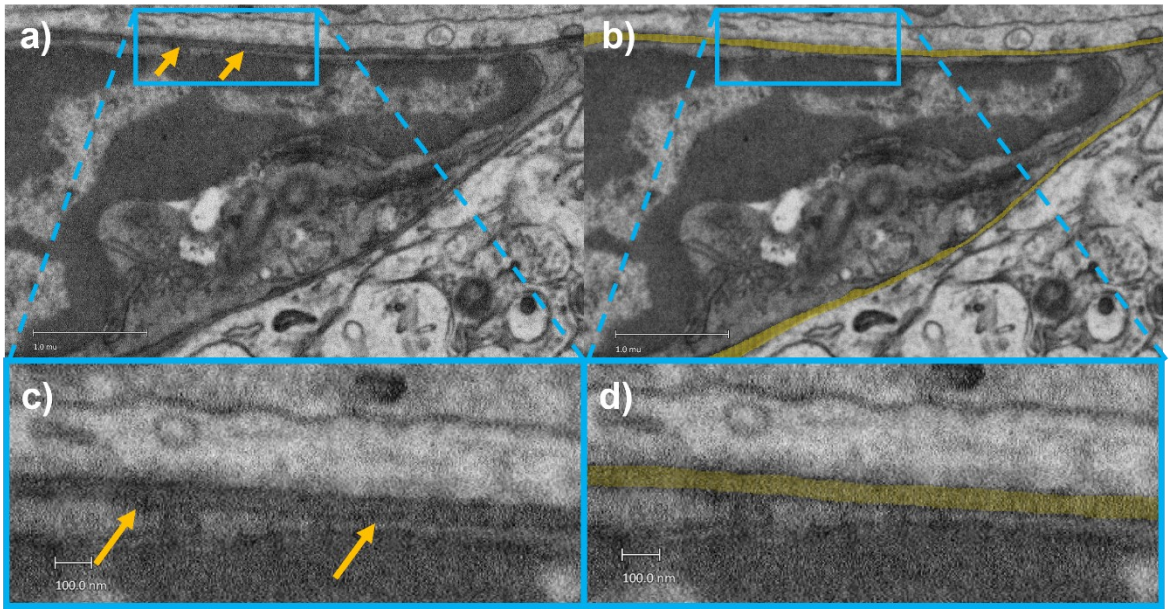

Figure 26: Basal membrane of the pericyte. An approximately 60nm wide basal membrane (→) lining can be identified around the cell. It encloses the pericyte on all sides and separates it from the endothelial cells.

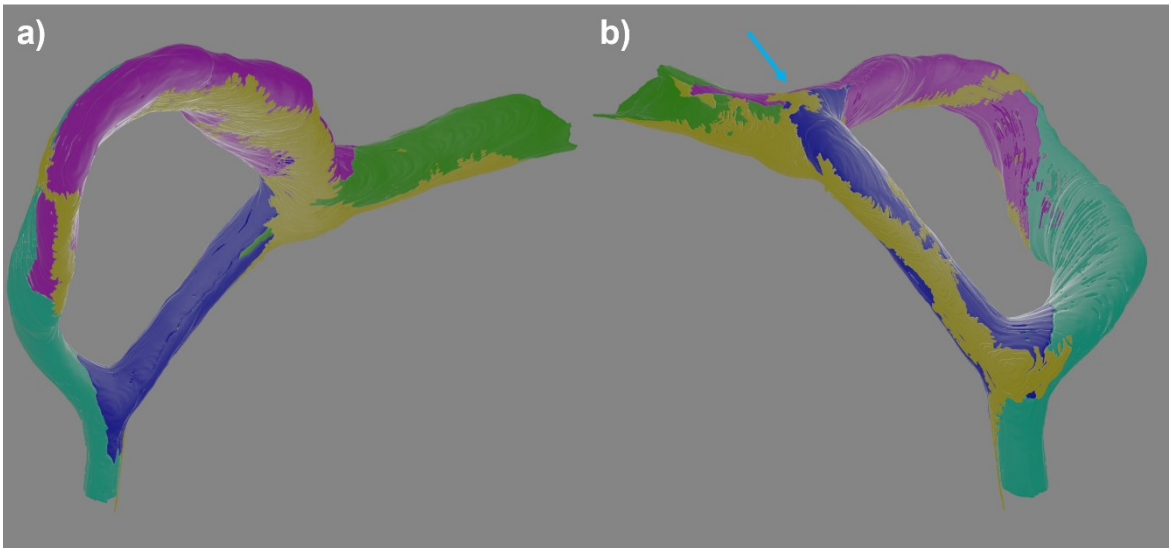

Figure 27: 3D view of the pericyte and the endothelium. The pericyte expands its processes beyond multiple endothelial cells. The back view b) reveals the short process at the top (→). It is narrow at first but expands radially into multiple directions afterwards. The longer branches send out multiple smaller processes left and right resembling a feather-like shape.

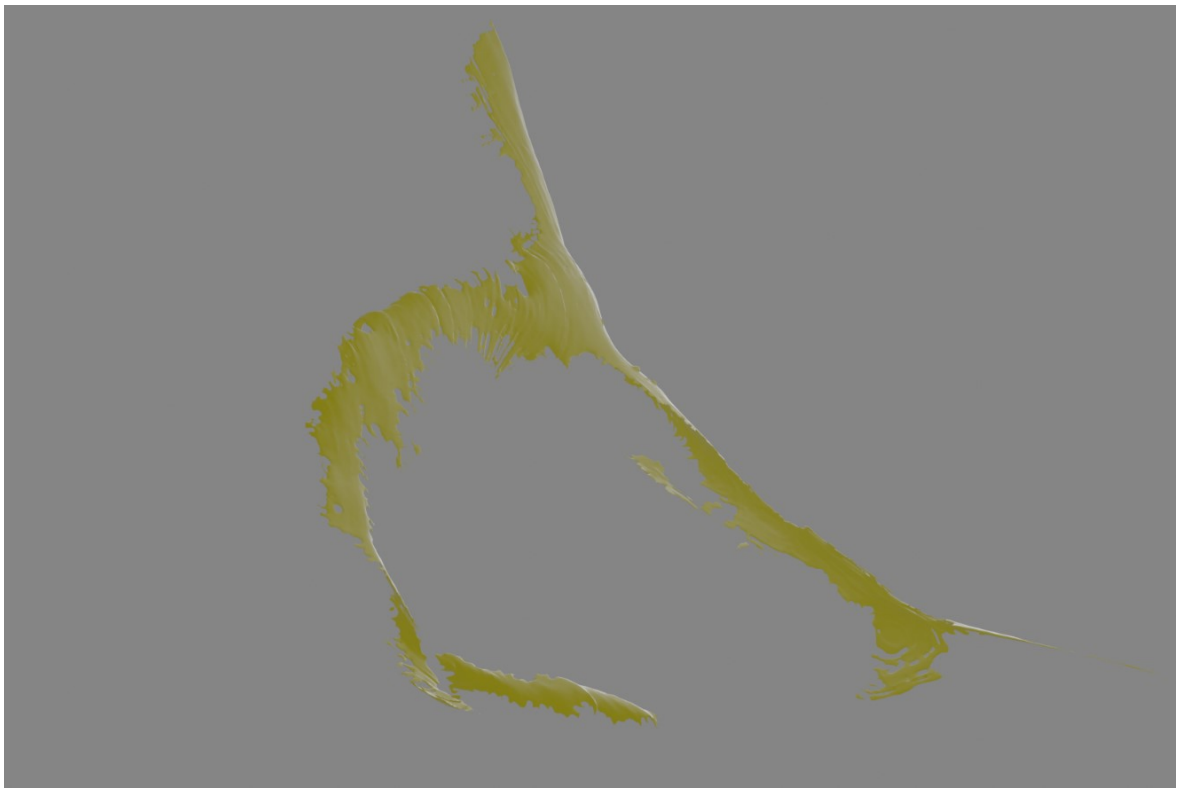

Figure 28: 3D view of the Pericyte. This reconstruction reveals the structure in more detail. 3 long branches can be identified although the top branch expands beyond the z-stack leaving part of the pericyte unknown. The primary processes splitting into pennate secondary processes is demonstrated in this 3D reconstruction.

3.4.7. Neuron Morphology and Subcellular Structures

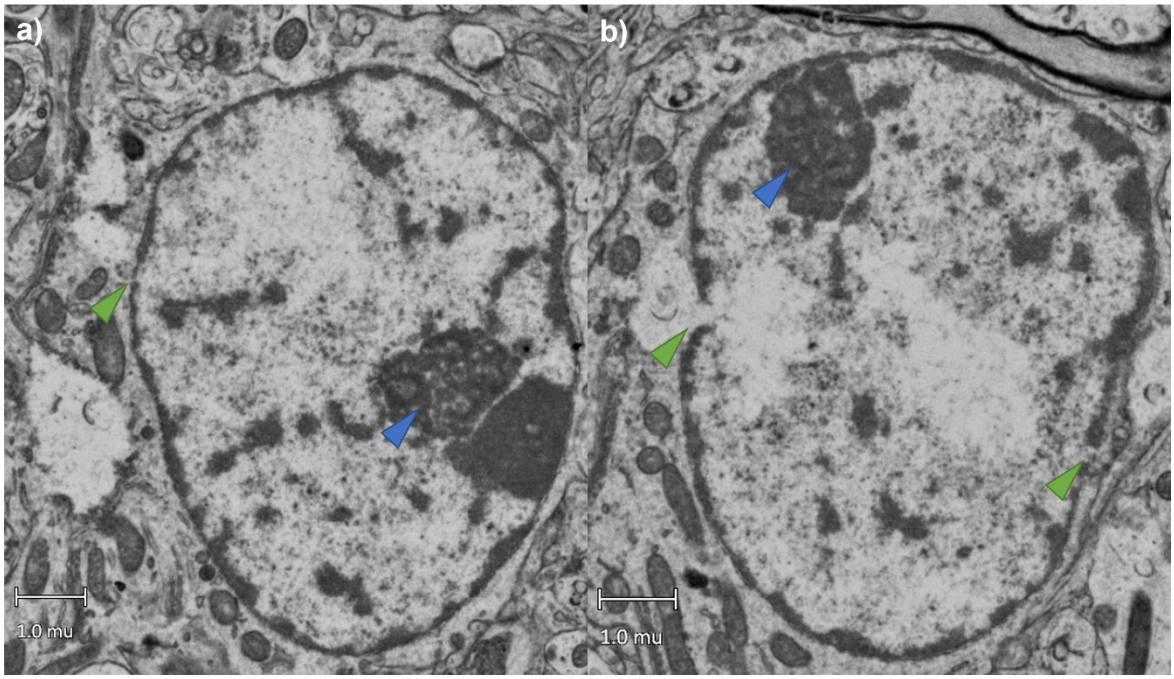

Figure 29: Neuron nucleus. The neuron has a rather pale nucleus with 2 prominent nucleoli (►). It also possesses multiple nuclear pores (►).

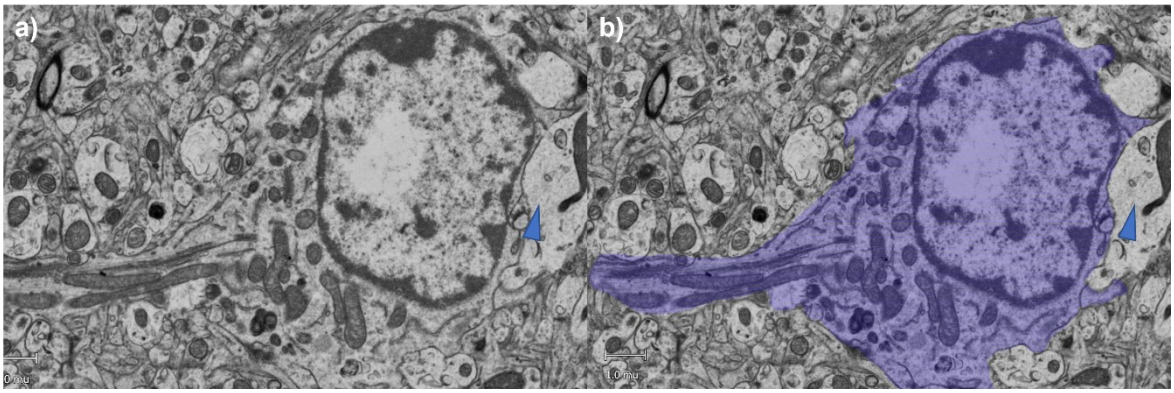

Figure 30: Neuron perikaryon. The neuron has intermediate electron density levels in the cytoplasm in between microglia or oligodendrocytes (dark) and astrocytes (light ►). A dendrite and multiple mitochondria are visible in the neuron.

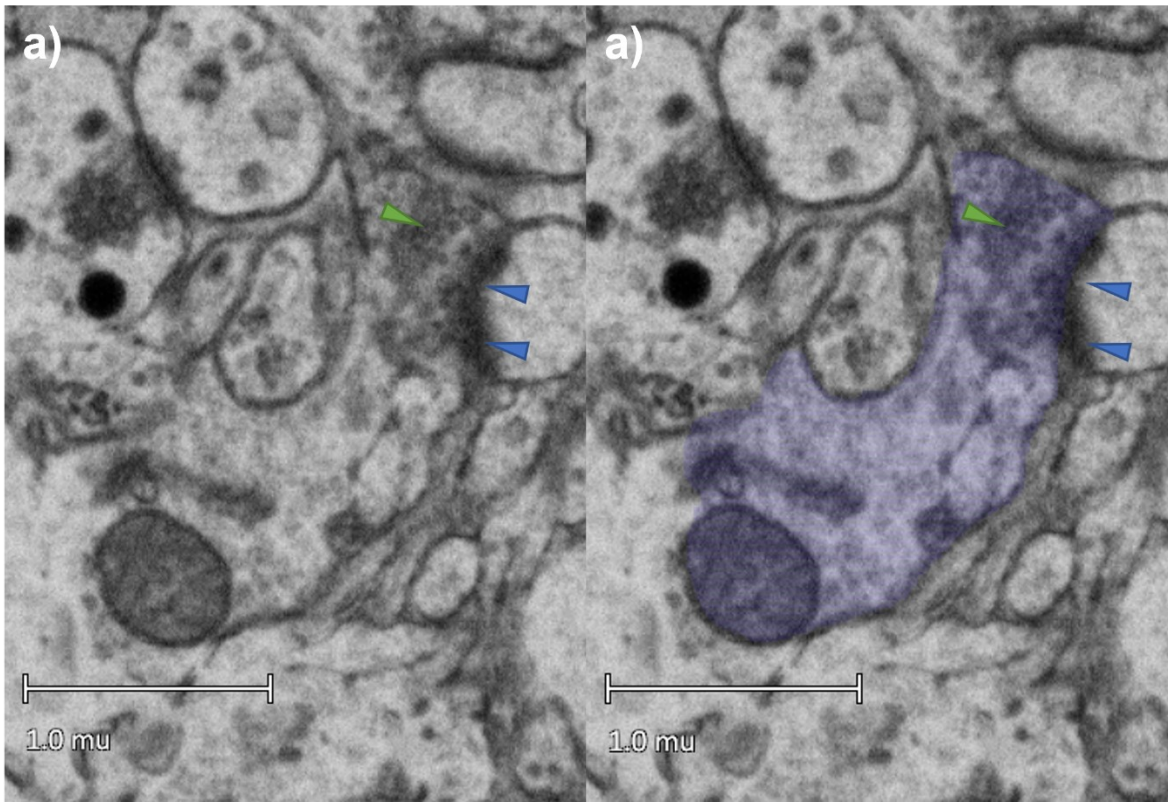

Figure 31: Synapse of the neuron. To confirm that this is a neuron, the branches were followed until synapses were found. Here, a post-synaptic density (▶) and synaptic vesicles (▶) were identified in the periphery of a branch.

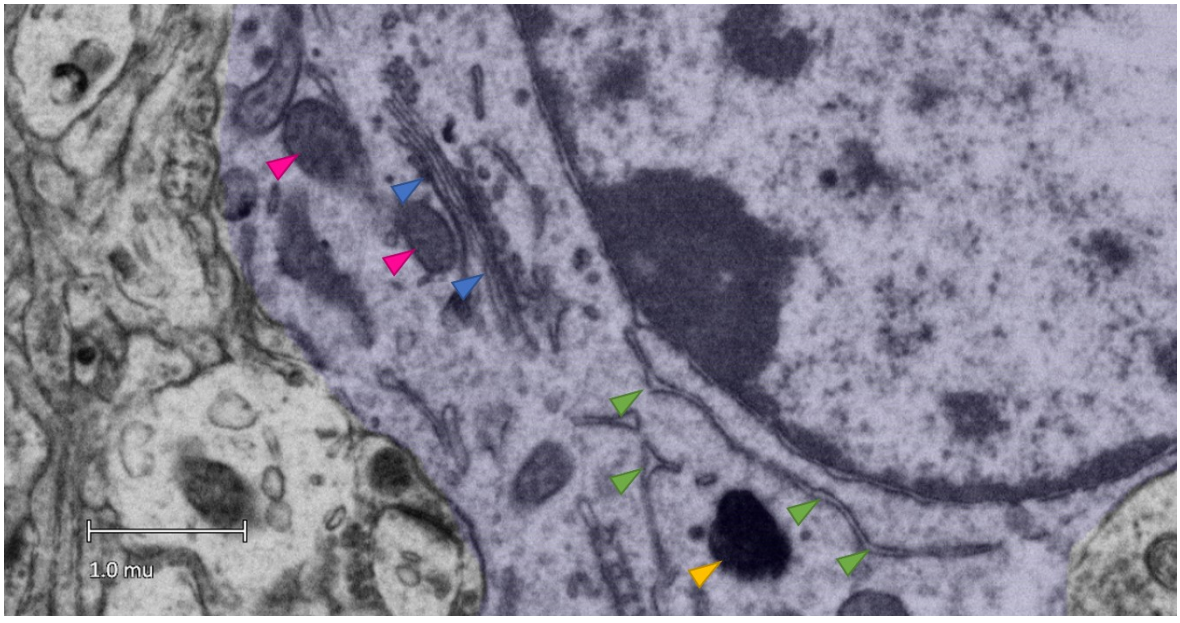

Figure 32: Cell organelles of the neuron. Multiple cell organelles can be found in the perinuclear area: Golgi apparatus with Golgi vesicles (▶), cisternae of endoplasmic reticulum (▶), a lysosome (▶), and mitochondria (▶).

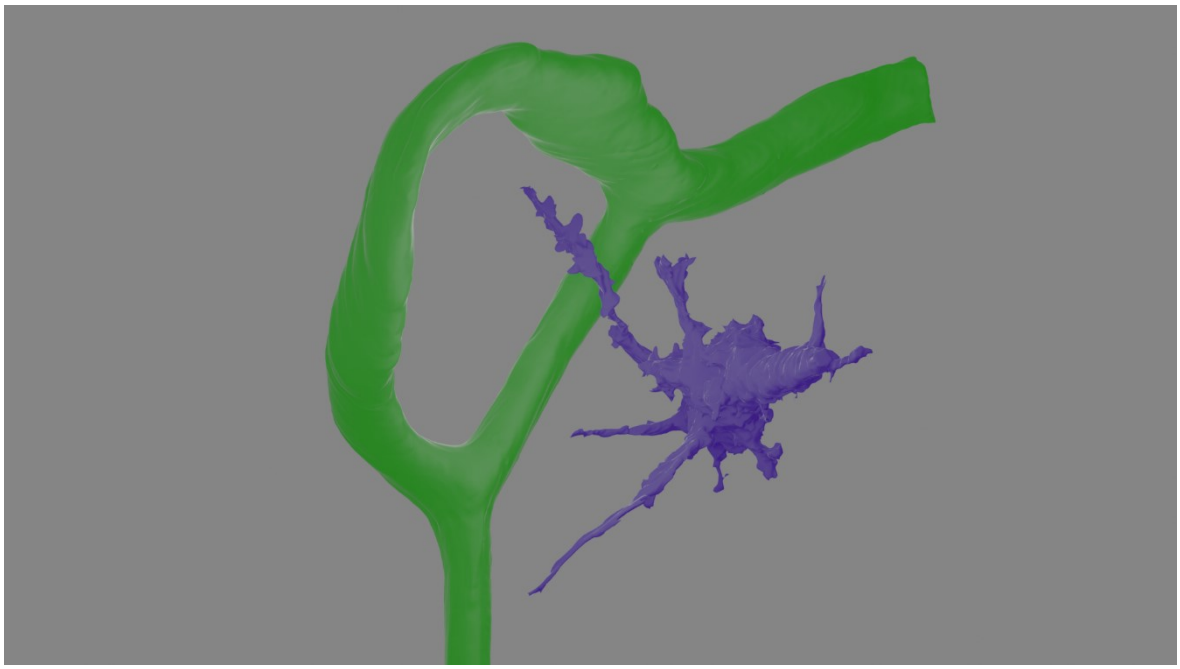

Figure 33: 3D reconstruction of the neuron and the vessel. The neuron can be seen in the vicinity of the microvessel and is visualized with its dendrites. It is important to note that the dendrites extend beyond the z-stack, thus the full magnitude of the neuron cannot be grasped.

3.4.8. Inspection of Microglia showed Multiple Lysosomes and Processes extending to the Vessel Disruption Site

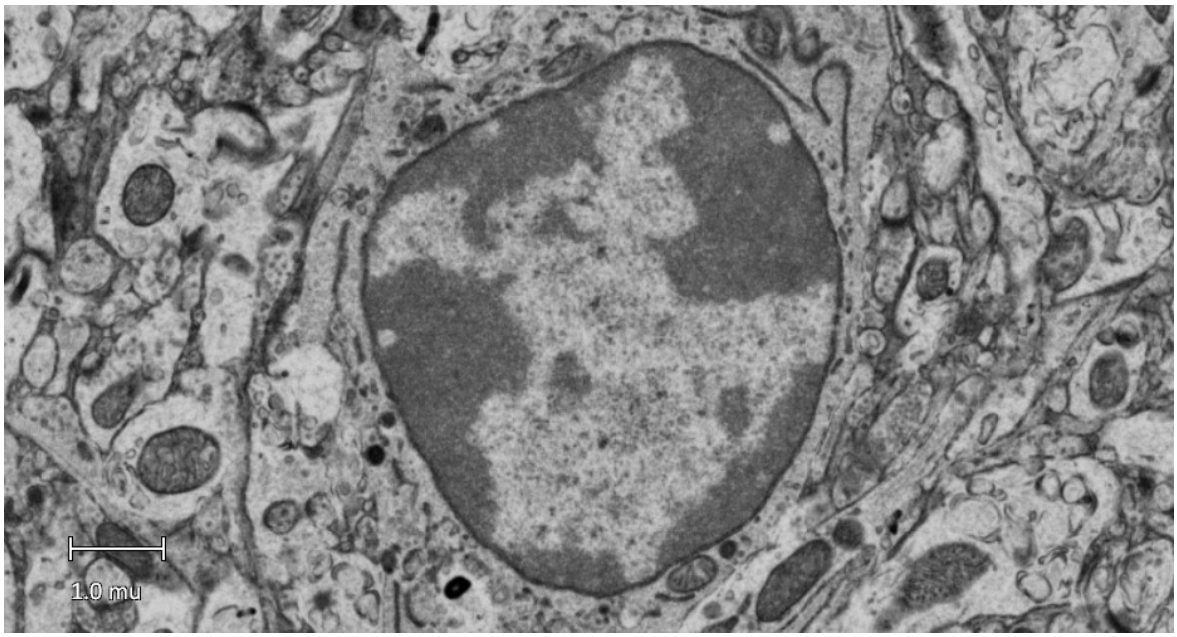

Figure 34: Microglia nucleus. Typical nucleus of a microglial cell with a peripheral heterochromatin pattern.

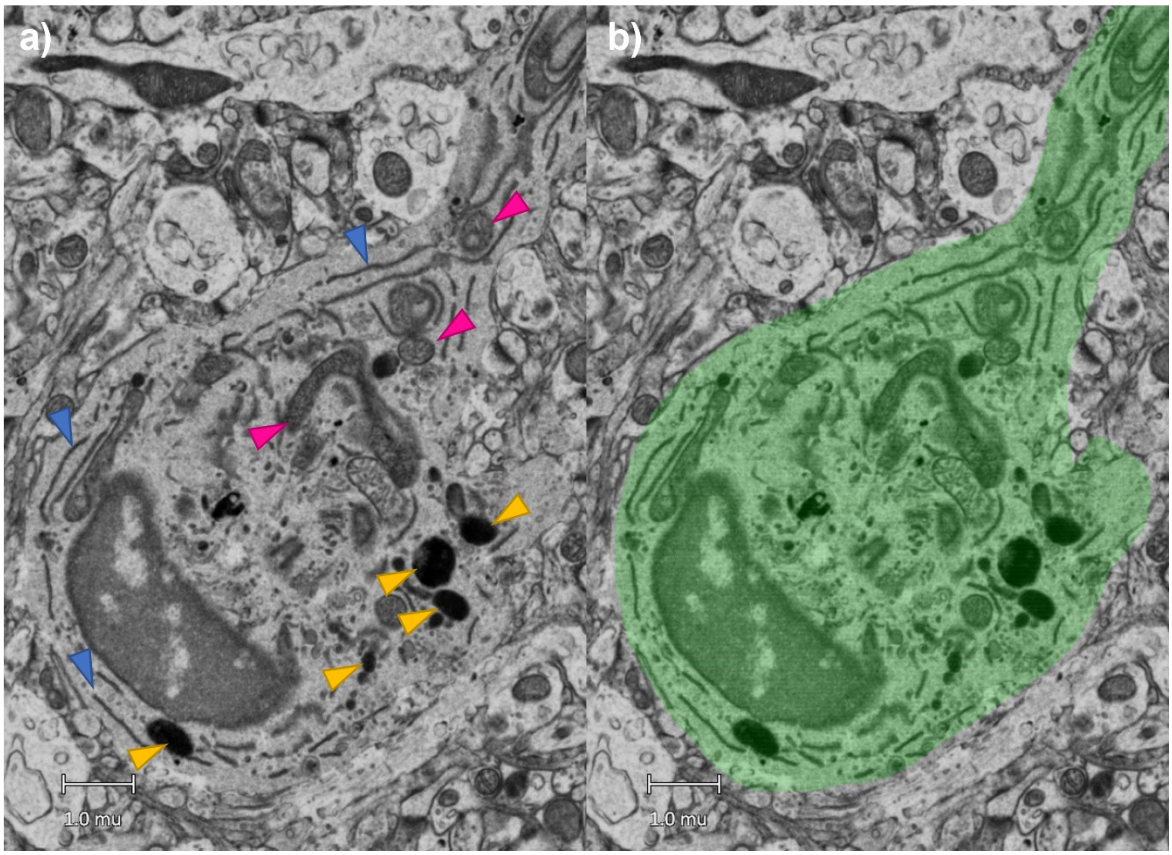

Figure 35: Microglial cell organelles. The microglial cell has relatively dark cytoplasm, characteristically long cisternae of endoplasmic reticulum (▶) and multiple lysosomes with lipidic inclusions (▶). Numerous Mitochondria (▶) are also present. A microglial process can also be seen extending from the cell body.

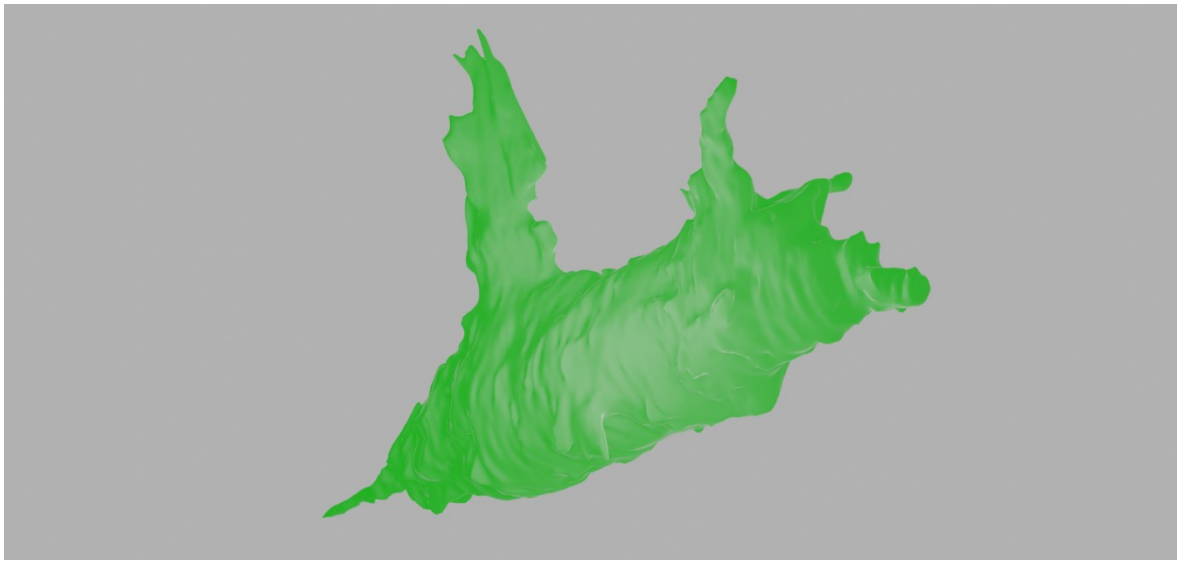

Figure 36: 3D reconstruction of the microglial cell. The perikaryon has an ovoid elongated structure and sends out several processes to the periphery. Compared

to the neuron or the pericyte, the processes are much shorter This cell was reconstructed in its whole magnitude.

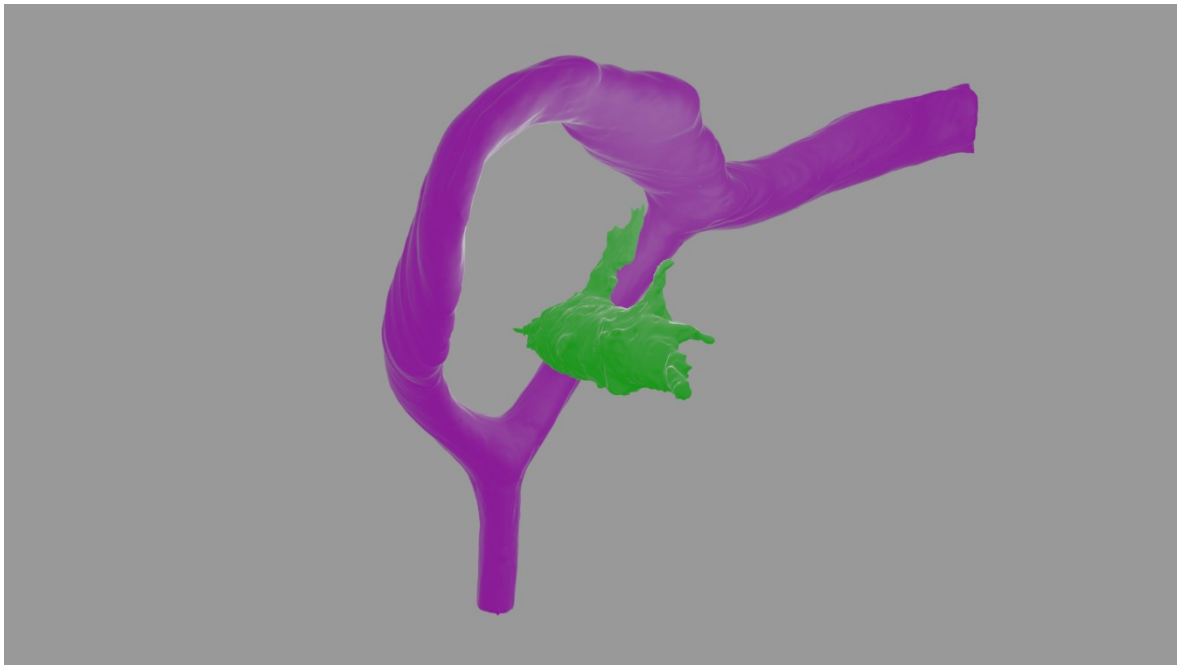

Figure 37: Microglial immune response. The image suggests that the microglial processes tend to expand in direction of the clot causing an immune response. This would be in accordance with the findings of the 2P imaging (**Figure 3**).

3.4.9. Astrocyte End Feet show little Pathologic Activity

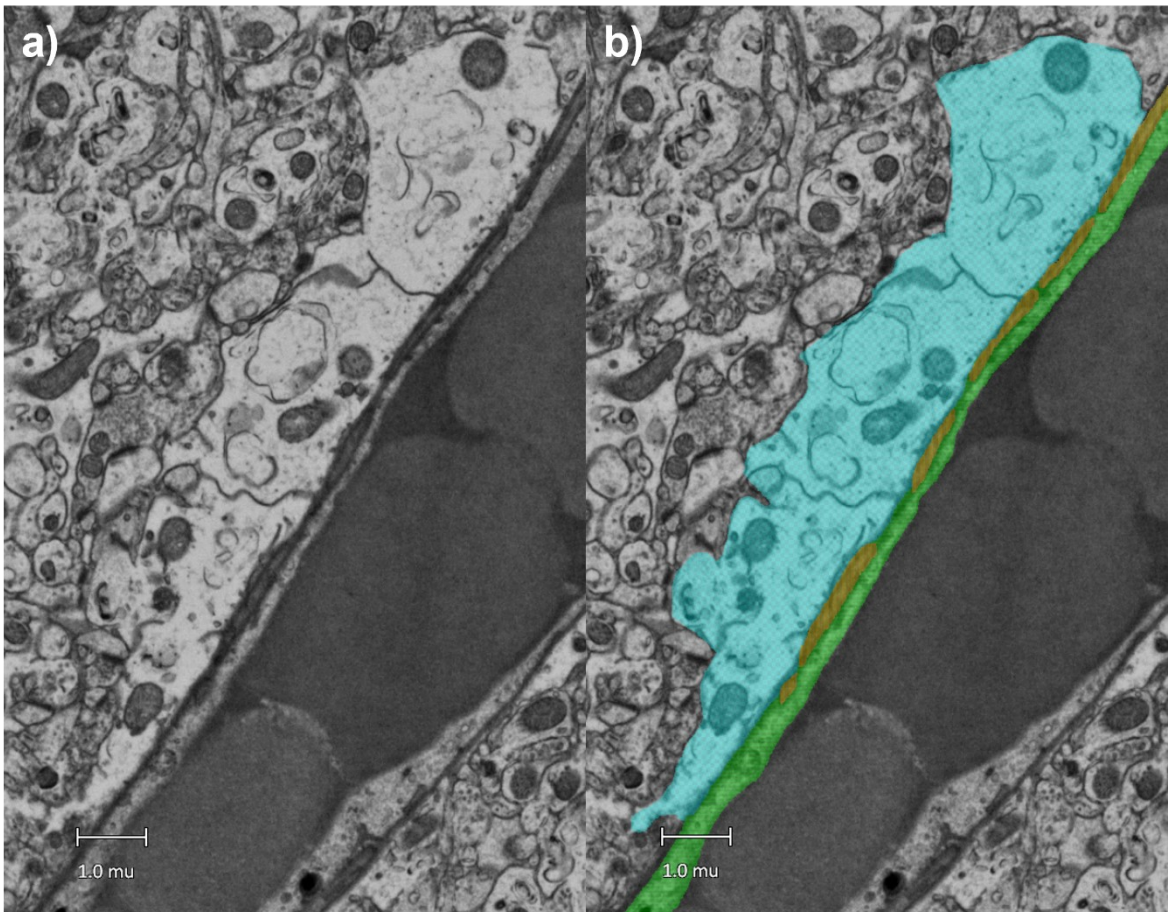

Figure 38: Astrocyte end foot and BBB. In addition to the perivascular location. the astrocyte end foot is identified by its clear cytoplasm. Astrocyte cytoplasm has very low electron density and can therefore be easily distinguished from other structures. The end foot can be seen resting upon the blood vessel. Pericyte processes with their basal lamina are also present in this slice. Together with the endothelium, all these components form the BBB.

Astrocyte end feet were found in multiple locations in the z-stack. They appear slightly swollen, but do not show clear pathologic changes like massive swelling or accumulation of glycogen granules.

3.4.10. Lipid Nanoparticle Accumulation and Transcytosis

Transportation of LNPs through the endothelial wall across the BBB into the brain tissue has been observed before. It was suggested that LNPs can travel through the cell membrane of endothelial cells if blood flow is slow enough to allow the process to happen (97).

Here, the fluorescent LNPs were seen accumulating right before the occlusion in the 2P-microscope (**Figure 6**). The LNPs are visible in the EM as well. They appear as plane expansions of higher electron density and can be found in between erythrocytes (**Figure 39**). This is in accordance with the findings in the 2P-microscope. Additionally, in the areas where LNPs accumulated in the blood vessel, closer inspection reveals lipid droplets moving through the endothelial wall to the parenchyma. Since, the blood flow is slowed down due to the occlusion here, it supports the suggestion that transcytosis is made possible through lower velocities allowing lipids to interact with the endothelial cell membrane (97).

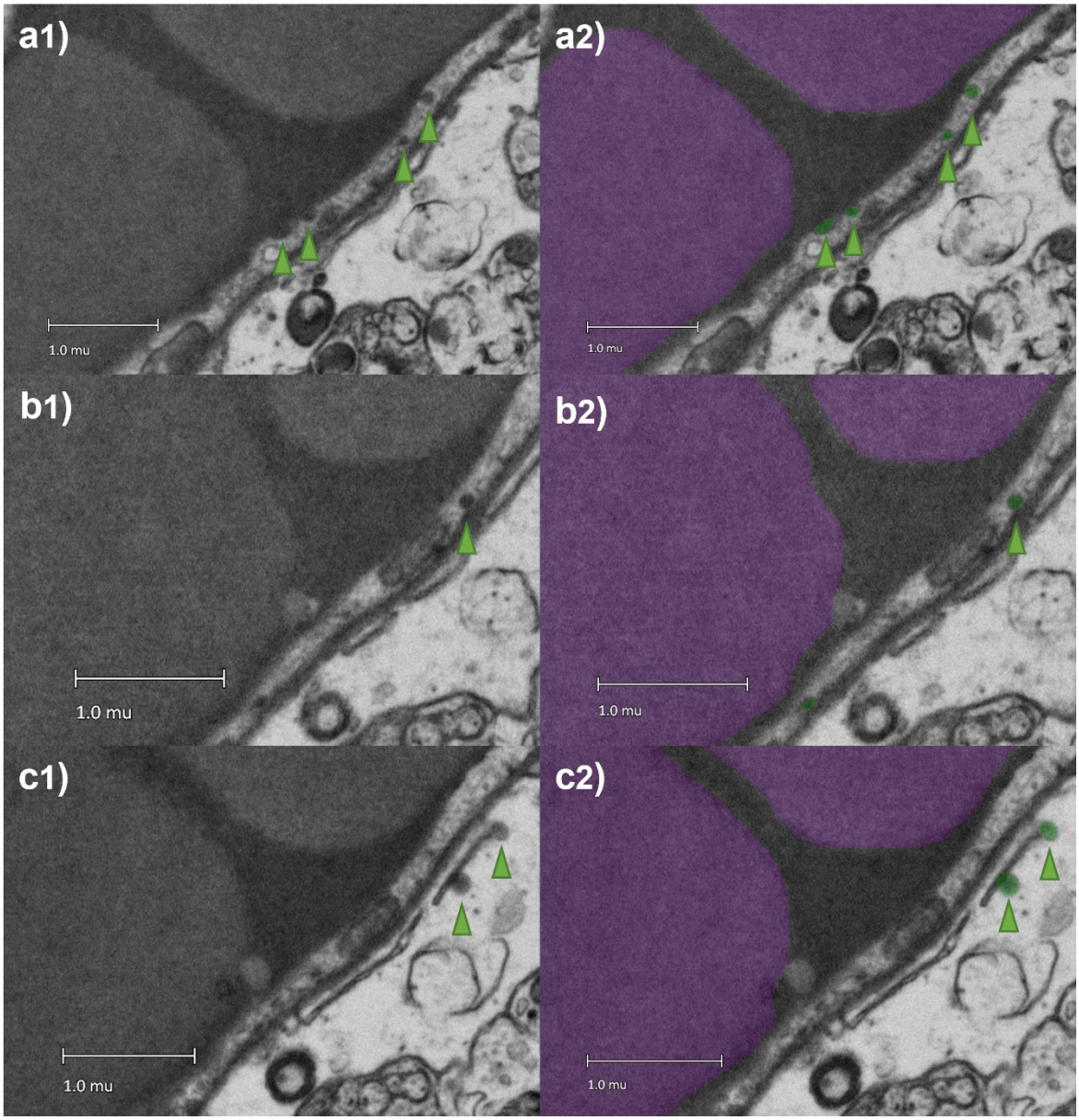

Figure 39: Transcytosis of LNPs through the endothelial wall. Erythrocytes are marked in magenta. The darker plain looking spaces in between erythrocytes are

accumulated LNPs. Droplets of lipids are highlighted in green. In a1) and a2) lipid droplets are seen emerging from the LNP mass in the vessel into the endothelial cell. In b1) and b2) a single droplet converging with the outer endothelial membrane is visible. In c1) and c2) droplets can be seen that have already passed the endothelial wall into the extravascular space. The lipid droplets here range from 80 nm to 150 nm diameter.

Another finding that supports transcytosis as the mechanism rather than disruptions in endothelial integrity or BBB is that all tight junctions that were followed through the whole z-stack were intact from beginning to end.

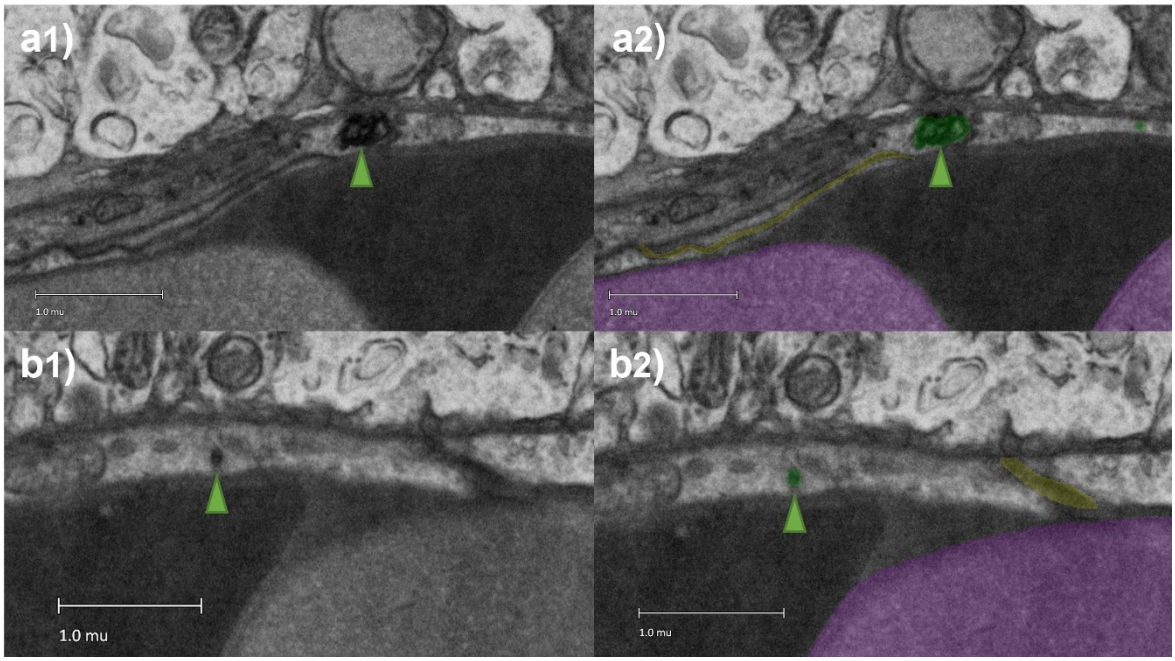

Figure 40: Lipid droplets in endothelium and intact tight junctions. LNP accumulations can be seen as dark material in between erythrocytes. A larger formation of electron dense material can be seen in a1) and a2), most likely of lipidic nature. In b1) and b2) another lipid droplet can be seen in the endothelial cell. Intact tight junctions are marked in yellow. There were no signs of endothelial disruptions in this area.

3.4.11. Axons, Dendrites and Synapses

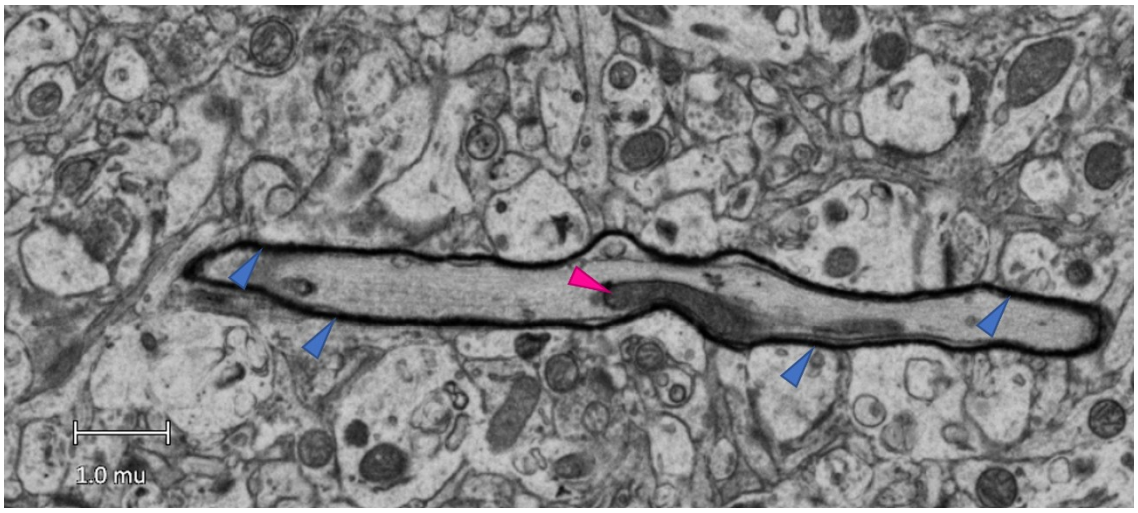

Figure 41: Myelinated axon. Myelinated axons can be identified by their very dark, electron dense myelin sheathing (▶). Mitochondria (▶) and thin lines of neurofilaments can be seen in the axon.

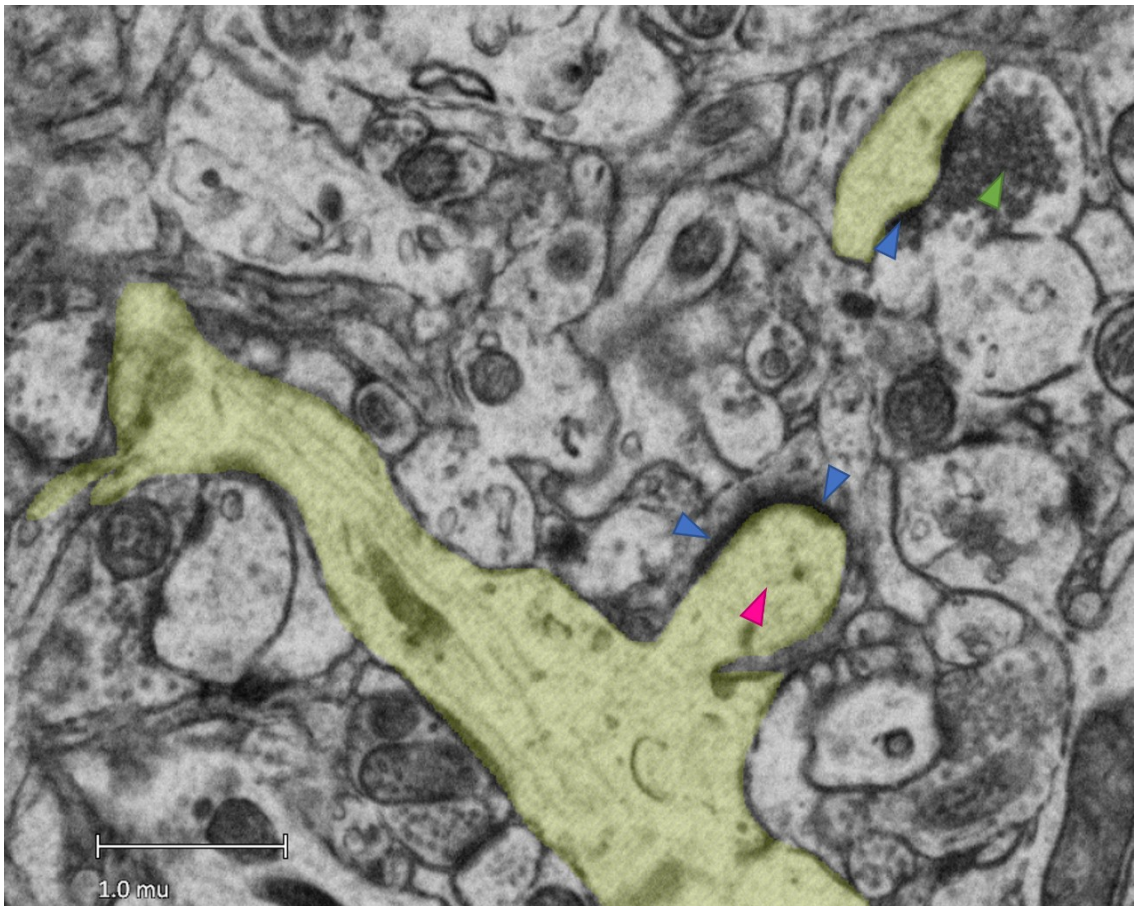

Figure 42: Dendrites and Synapses. The dendrites have irregular progression patterns, cotton-like cytoplasm content and actin filaments. Dendritic spines appear

(►) as protrusions from the dendrite. Mature synapses characterized by the post synaptic density (►) can be seen here. An axon terminal filled with neurotransmitter vesicles (►) contacting a dendrite appears on the top right.

3.4.12. Combining all Pieces to a Single Picture

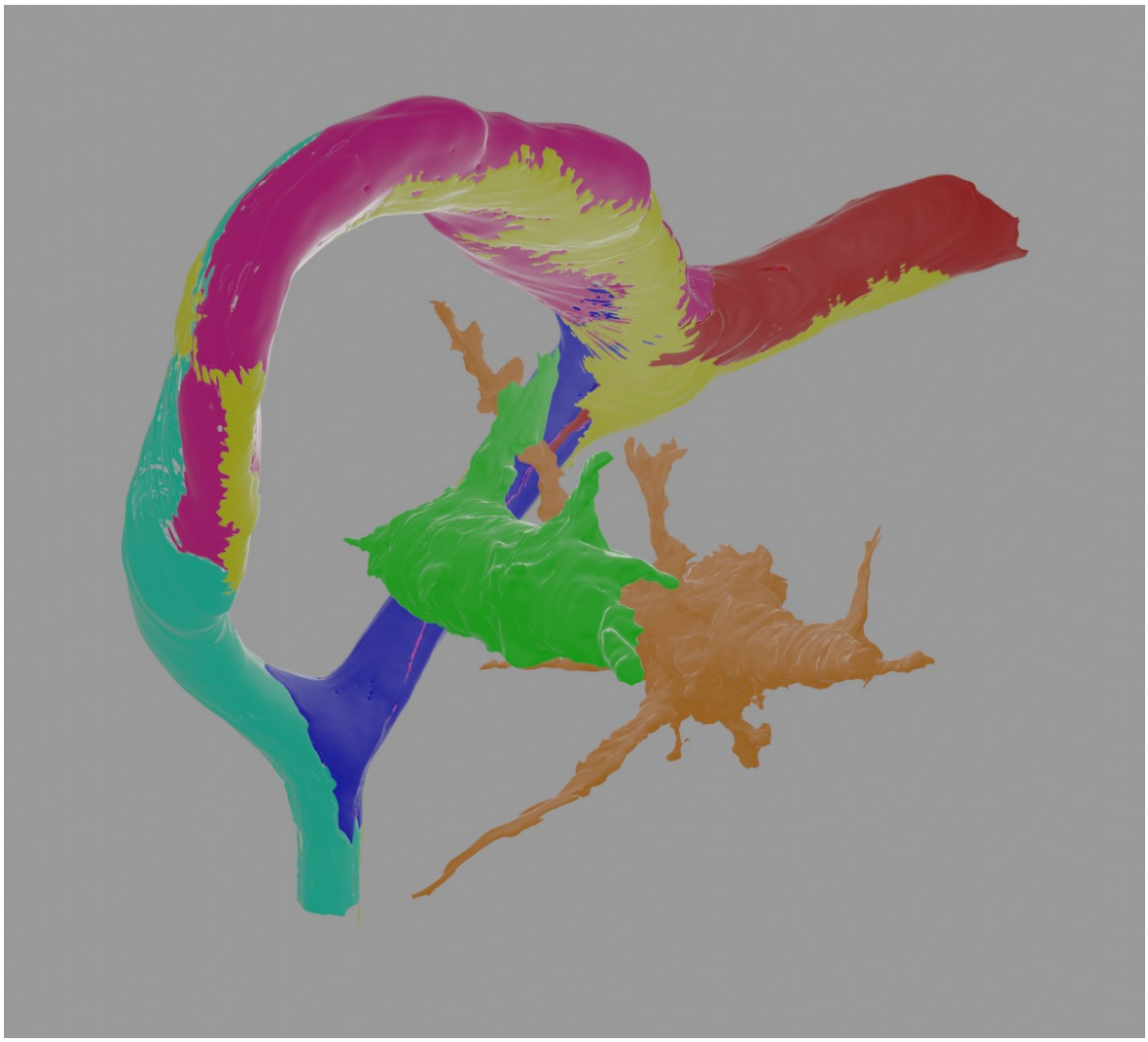

Figure 43: 3D reconstruction of a partially occluded microvessel in the mouse brain with single cellular components. This image combines all endothelial cells (Endothelial cell 1, Endothelial cell 2, Endothelial cell 3, Endothelial cell 4), a pericyte, a neuron and a microglial cell.

4. Discussion

4.1. Magnetic Nanoparticles as Stroke Inductor and Correlation Landmark for CLEM

Iron oxide nanoparticles are very versatile and can be used in many ways. They are magnetic and react to magnetic forces, which makes them very useful to induce focal ischemia in the brain. This method provides a way to induce a targetable, focal cortical stroke, with the great benefit of easy reperfusion and no craniotomy. Using a cranial window, the distance to the magnet can be lowered increasing the forces applied to the nanoparticles and therefore increasing the stroke severity. The magnetic nanoparticles have very low toxicity and can safely be used *in vivo*.

In addition to stroke induction iron oxide nanoparticles also show luminescent properties. If excited with the correct wavelength of light, they are visible in the 2-photon microscope. Additionally, they have very high electron density, making them easily detectable in the electron microscope. Here, they have been successfully used as correlation landmarks for 2-photon and electron microscopy. This opens the door for a lot of research questions. Pathophysiology of stroke remains unclear and one of the biggest problems for scientists is the methodology. It is very difficult to induce stroke and create data with high temporal and spatial resolution and the same time. This problem can be alleviated by using magnetic nanoparticles. Using this method, the processes that happen after a stroke could be analysed at different time points and compared.

4.2. Microcirculatory Changes and Endothelial Damage after Reperfusion of Stroke

Finding a region of interest with the electron microscope was very difficult in the past. With the bright magnetic nanoparticles as correlation landmarks, regions of interest can be identified in the 2-photon microscope and then selectively targeted with the electron microscope. In this work, microcirculatory disruptions were observed after reperfusion of cortical stroke. The magnetic nanoparticles in the area were identified *in vivo* by the 2-photon microscope and used as a reference to create a high-resolution z-stack of images of an occluded microvessel with the electron microscope. In the electron microscope images a hole in the endothelial cell was identified. The hole went directly through a single endothelial cell and was not

connected to tight junctions or other endothelial cells. Interestingly no blood content flowed out through the hole but rather a structure that looked strikingly similar to an astrocyte end foot invaginated into the hole, constricting the blood vessel and blocking the blood flow. It is known that microcirculation is often disrupted after stroke even if the occluded artery is recanalized (no-reflow phenomenon). Here, a clot that formed minutes after reperfusion was easily found with the help of *in vivo* imaging using the 2P microscope. This method could be applied in many further experiments and potentially greatly increase the knowledge of no-reflow phenomena. For example, the cell activity of different cells in the CNS could be investigated in relation to no-reflow with both 2P microscopy and EM. Pericytes, astrocytes, and microglia could all potentially be involved and need to be investigated thoroughly. Smooth muscle cells were not present in the EM-stack, suggesting that they might not be involved in no-reflow. Small arterioles with thin linings of smooth muscle cells and their behaviour after stroke could be investigated in future experiments. The hole in the microvessel that was found here could relate to no-reflow, but it could also be an artifact of laser radiation during *in vivo* imaging or fixation and sample preparation for electron microscopy. If this is not an artifact and can be reproduced in further studies, analysis of this effect might reveal more about the pathophysiological mechanisms of no-reflow. This work offers little evidence about the nature of this effect since the experiment was carried out on one mouse and only a single z-stack was made.

4.3. Erythrocyte Deformation

Previous studies have shown the flexibility of the erythrocyte cytoskeleton. Usually, erythrocytes have a biconcave form which is essential for oxygen transport. Erythrocytes can alter their shape to become polyhedral when high mechanical pressure is present. To a small degree, this effect occurs when erythrocytes need to fit through small capillaries. Total deformation with many concave faces has been observed previously in thrombi. Here, the erythrocytes before the constriction were closely stacked on top of each other with mostly convex surfaces whereas the erythrocytes after the constriction were flattened and showed many concavities. They are most likely erythrocytes that made it through the constriction, totally deforming in the process.

4.4. Immune Response to Microcirculatory Disruption

Microglia were observed in the 2-photon microscope using a green fluorescent protein-derived sensor. Over time, they extended their processes towards occluded microvessels. This suggests that there is a fast immune response to microvessel occlusions. In the z-stack of the electron microscope images a microglial cell in the vicinity of the blood vessel was identified. 3D reconstruction demonstrated how larger processes of the microglia extended towards the vessel disruption. Since only a single microglial cell was found in the images, this could also be a coincidence, but it is in accordance with the observation made during 2-photon imaging. Further investigation is needed to learn more about microglia interaction with the microcirculation. Imaging multiple microglia at different time points of microcirculatory disruptions could reveal more interactions between microglia and other cells.

4.5. Lipid Nanoparticles Leave the Blood Vessel Despite Intact Blood Brain Barrier

Lipid nanoparticles were used as fluorescent markers to trace the blood vessels in the 2-photon microscope. They also possess some electron density making them visible in the electron microscope especially when accumulated. In the constricted microvessel here, lipid nanoparticles accumulate in between erythrocytes. In the area around the vessel, droplets of lipid nanoparticles can be found. Therefore, the blood-brain barrier has been closely observed for disruptions and leakage. One pericyte was present around the vessel. It was traced throughout the z-stack and reconstructed in 3D and there were no signs for pericyte disruption. Except for the one hole with the invagination, the endothelial cells also had no discontinuities. At no point was there leakage of material other than lipid nanoparticles, suggesting an intact endothelial lining. Astrocyte end feet were also identified, and they showed no pathological signs like swelling or uptake of glycogen granules. Lastly, the tight junctions were also traced and showed no discontinuities. 3D reconstructions of the tight junctions also revealed that they extend in between two distant endothelial cells across the membrane of an underlying third endothelial cell, stabilizing the whole endothelial union. Closer inspection showed lipid droplets crossing the intact endothelial membrane via transcytosis. In normal flowing blood there is not enough time for lipids to create contact with the membrane for transcytosis. It could be

possible that transcytosis is made possible here due to the low velocity of the blood. This is therapeutically highly relevant because it shows that lipid nanoparticles could possibly be used to target injured tissue since they leave the blood flow exactly where the occlusion reduces flow velocity. The vessel itself only needs to be constricted or occluded and does not need to be damaged for lipid nanoparticles to reach the tissue. In addition to stroke, this could also be of interest in tumor therapy. Tumors generate their own blood supply by building new blood vessels via angiogenesis (147). In pancreatic cancer, for example, these blood vessels have slower blood flow which could potentially be abused by lipid nanoparticles (148). Since the BBB does not need to be disrupted for lipid nanoparticle functionality as drug carriers, the therapeutic window becomes very short. They could be used in the very early stages of stroke and still be effective. Further investigation could test the effect of lipid nanoparticles attached to neuroprotective substances on the tissue in microcirculatory disruptions.

4.6. Astrocyte Invasion into the Blood Vessel

As already mentioned above, the structure invading the blood vessel fulfils most morphological criteria of an astrocyte. The very clear, low electron-dense cytoplasm with dots of microtubules in combination with the location make it very likely that it is an astrocyte end foot. Reactive gliosis is a known process that occurs after certain forms of CNS damage such as ischemia. Gliosis involves the swelling and proliferation of glial cells, especially astrocytes. The invagination of the blood vessel could possibly be a result of reactive gliosis. The vessel damage could also be an artifact. If gliosis truly supports the impairment of microcirculation, therapeutic approaches that reduce the effects of gliosis could potentially improve the outcome of stroke therapy. This newly discovered occurrence demands further investigation if the astrocyte invasion can be experimentally reproduced.

5. Conclusion

This thesis demonstrates the successful use of magnetic nanoparticles as a stroke inductor and a correlation landmark for correlative light and electron microscopy. This method enables the induction of targetable, focal, reproducible, cortical stroke. It further allows to selectively gather information of the processes in the aftermath with high temporal and spatial resolution. We used this method to observe and analyze disruptions in the blood flow after restoring blood supply to the brain following a stroke. Our approach allowed us to capture these changes with detail and precision. Further experiments using this method could reveal more about the pathophysiology of stroke and microcirculatory changes after stroke.

References

1. GBD 2016 Stroke Collaborators. Global, regional, and national burden of stroke, 1990-2016: a systematic analysis for the Global Burden of Disease Study 2016. Lancet Neurol. 2019 May;18(5):439–58.

2. Sacco RL, Kasner SE, Broderick JP, Caplan LR, Connors JJB, Culebras A, et al. An updated definition of stroke for the 21st century: a statement for healthcare professionals from the American Heart Association/American Stroke Association. Stroke. 2013 Jul;44(7):2064–89.

3. Dalkara T, Arsava EM. Can restoring incomplete microcirculatory reperfusion improve stroke outcome after thrombolysis? J Cereb Blood Flow Metab Off J Int Soc Cereb Blood Flow Metab. 2012 Dec;32(12):2091–9.

4. Kloner RA, King KS, Harrington MG. No-reflow phenomenon in the heart and brain. Am J Physiol Heart Circ Physiol. 2018 Sep 1;315(3):H550–62.

5. Bosetti F, Galis ZS, Bynoe MS, Charette M, Cipolla MJ, del Zoppo GJ, et al. “Small Blood Vessels: Big Health Problems?”: Scientific Recommendations of the National Institutes of Health Workshop. J Am Heart Assoc Cardiovasc Cerebrovasc Dis. 2016 Nov 4;5(11):e004389.

6. Mouridsen K, Hansen MB, Østergaard L, Jespersen SN. Reliable estimation of capillary transit time distributions using DSC-MRI. J Cereb Blood Flow Metab Off J Int Soc Cereb Blood Flow Metab. 2014 Sep;34(9):1511–21.

7. Harder DR, Zhang C, Gebremedhin D. Astrocytes function in matching blood flow to metabolic activity. News Physiol Sci Int J Physiol Prod Jointly Int Union Physiol Sci Am Physiol Soc. 2002 Feb;17:27–31.

8. Lovick TA, Brown LA, Key BJ. Neurovascular relationships in hippocampal slices: physiological and anatomical studies of mechanisms underlying flow-metabolism coupling in intraparenchymal microvessels. Neuroscience. 1999;92(1):47–60.

9. Ballabh P, Braun A, Nedergaard M. The blood-brain barrier: an overview: structure, regulation, and clinical implications. Neurobiol Dis. 2004 Jun;16(1):1–13.

10. Mathiisen TM, Lehre KP, Danbolt NC, Ottersen OP. The perivascular astroglial sheath provides a complete covering of the brain microvessels: an electron microscopic 3D reconstruction. Glia. 2010 Jul;58(9):1094–103.

11. Kuriakose D, Xiao Z. Pathophysiology and Treatment of Stroke: Present Status and Future Perspectives. Int J Mol Sci. 2020 Oct 15;21(20):7609.

12. Kalogeris T, Baines CP, Krenz M, Korthuis RJ. Cell biology of ischemia/reperfusion injury. Int Rev Cell Mol Biol. 2012;298:229–317.

13. Broughton BRS, Reutens DC, Sobey CG. Apoptotic mechanisms after cerebral ischemia. Stroke. 2009 May;40(5):e331-339.

14. Woodruff TM, Thundyil J, Tang SC, Sobey CG, Taylor SM, Arumugam TV. Pathophysiology, treatment, and animal and cellular models of human ischemic stroke. Mol Neurodegener. 2011 Jan 25;6(1):11.

15. Zheng Z, Yenari MA. Post-ischemic inflammation: molecular mechanisms and therapeutic implications. Neurol Res. 2004 Dec;26(8):884–92.

16. Hamann GF, Liebetrau M, Martens H, Burggraf D, Kloss CUA, Bültemeier G, et al. Microvascular basal lamina injury after experimental focal cerebral ischemia and reperfusion in the rat. J Cereb Blood Flow Metab Off J Int Soc Cereb Blood Flow Metab. 2002 May;22(5):526–33.

17. Ishikawa M, Cooper D, Russell J, Salter JW, Zhang JH, Nanda A, et al. Molecular determinants of the prothrombogenic and inflammatory phenotype assumed by the postischemic cerebral microcirculation. Stroke. 2003 Jul;34(7):1777–82.

18. Burrows FE, Bray N, Denes A, Allan SM, Schiessl I. Delayed reperfusion deficits after experimental stroke account for increased pathophysiology. J Cereb Blood Flow Metab Off J Int Soc Cereb Blood Flow Metab. 2015 Feb;35(2):277–84.

19. Yemisci M, Gursoy-Ozdemir Y, Vural A, Can A, Topalkara K, Dalkara T. Pericyte contraction induced by oxidative-nitrative stress impairs capillary reflow despite successful opening of an occluded cerebral artery. Nat Med. 2009 Sep;15(9):1031–7.

20. Little JR, Kerr FWL, Sundt TM. Microcirculatory Obstruction in Focal Cerebral Ischemia: An Electron Microscopic Investigation in Monkeys. Stroke. 1976 Jan 1;7(1):25–30.

21. Garcia JH, Liu KF, Yoshida Y, Chen S, Lian J. Brain microvessels: factors altering their patency after the occlusion of a middle cerebral artery (Wistar rat). Am J Pathol. 1994 Sep;145(3):728–40.

22. Halassa MM, Fellin T, Takano H, Dong JH, Haydon PG. Synaptic islands defined by the territory of a single astrocyte. J Neurosci Off J Soc Neurosci. 2007 Jun 13;27(24):6473–7.

23. Simard M, Arcuino G, Takano T, Liu QS, Nedergaard M. Signaling at the gliovascular interface. J Neurosci Off J Soc Neurosci. 2003 Oct 8;23(27):9254–62.

24. Mulligan SJ, MacVicar BA. Calcium transients in astrocyte endfeet cause cerebrovascular constrictions. Nature. 2004 Sep 9;431(7005):195–9.

25. Schipke CG, Kettenmann H. Astrocyte responses to neuronal activity. Glia. 2004 Aug 15;47(3):226–32.

26. Metea MR, Newman EA. Glial cells dilate and constrict blood vessels: a mechanism of neurovascular coupling. J Neurosci Off J Soc Neurosci. 2006 Mar 15;26(11):2862–70.

27. McCarron RM, Chen Y, Tomori T, Strasser A, Mechoulam R, Shohami E, et al. Endothelial-mediated regulation of cerebral microcirculation. J Physiol Pharmacol Off J Pol Physiol Soc. 2006 Nov;57 Suppl 11:133–44.

28. Allt G, Lawrenson JG. Pericytes: cell biology and pathology. Cells Tissues Organs. 2001;169(1):1–11.

29. Bandopadhyay R, Orte C, Lawrenson JG, Reid AR, De Silva S, Allt G. Contractile proteins in pericytes at the blood-brain and blood-retinal barriers. J Neurocytol. 2001 Jan;30(1):35–44.

30. Mohamed Mokhtarudin MJ, Payne SJ. Mathematical model of the effect of ischemia-reperfusion on brain capillary collapse and tissue swelling. Math Biosci. 2015 May;263:111–20.

31. Shin HK, Dunn AK, Jones PB, Boas DA, Moskowitz MA, Ayata C. Vasoconstrictive neurovascular coupling during focal ischemic depolarizations. J Cereb Blood Flow Metab Off J Int Soc Cereb Blood Flow Metab. 2006 Aug;26(8):1018–30.

32. Longa EZ, Weinstein PR, Carlson S, Cummins R. Reversible middle cerebral artery occlusion without craniectomy in rats. Stroke. 1989 Jan;20(1):84–91.

33. Hata R, Mies G, Wiessner C, Fritze K, Hesselbarth D, Brinker G, et al. A reproducible model of middle cerebral artery occlusion in mice: hemodynamic, biochemical, and magnetic resonance imaging. J Cereb Blood Flow Metab Off J Int Soc Cereb Blood Flow Metab. 1998 Apr;18(4):367–75.

34. Schmid-Elsaesser R, Zausinger S, Hungerhuber E, Baethmann A, Reulen HJ. A critical reevaluation of the intraluminal thread model of focal cerebral ischemia: evidence of inadvertent premature reperfusion and subarachnoid hemorrhage in rats by laser-Doppler flowmetry. Stroke. 1998 Oct;29(10):2162–70.

35. McColl BW, Carswell HV, McCulloch J, Horsburgh K. Extension of cerebral hypoperfusion and ischaemic pathology beyond MCA territory after intraluminal filament occlusion in C57Bl/6J mice. Brain Res. 2004 Jan 30;997(1):15–23.

36. Maeda K, Hata R, Hossmann KA. Regional metabolic disturbances and cerebrovascular anatomy after permanent middle cerebral artery occlusion in C57black/6 and SV129 mice. Neurobiol Dis. 1999 Apr;6(2):101–8.

37. Li F, Omae T, Fisher M. Spontaneous hyperthermia and its mechanism in the intraluminal suture middle cerebral artery occlusion model of rats. Stroke. 1999 Nov;30(11):2464–70; discussion 2470-2471.

38. Drew PJ, Shih AY, Driscoll JD, Knutsen PM, Blinder P, Davalos D, et al. Chronic optical access through a polished and reinforced thinned skull. Nat Methods. 2010 Dec;7(12):981–4.

39. Holtmaat A, Bonhoeffer T, Chow DK, Chuckowree J, De Paola V, Hofer SB, et al. Long-term, high-resolution imaging in the mouse neocortex through a chronic cranial window. Nat Protoc. 2009;4(8):1128–44.

40. Watson BD, Dietrich WD, Busto R, Wachtel MS, Ginsberg MD. Induction of reproducible brain infarction by photochemically initiated thrombosis. Ann Neurol. 1985 May;17(5):497–504.

41. Kim GW, Sugawara T, Chan PH. Involvement of oxidative stress and caspase-3 in cortical infarction after photothrombotic ischemia in mice. J Cereb Blood Flow Metab Off J Int Soc Cereb Blood Flow Metab. 2000 Dec;20(12):1690–701.

42. Sommer CJ. Ischemic stroke: experimental models and reality. Acta Neuropathol (Berl). 2017 Feb;133(2):245–61.

43. Lee VM, Burdett NG, Carpenter A, Hall LD, Pambakian PS, Patel S, et al. Evolution of photochemically induced focal cerebral ischemia in the rat. Magnetic resonance imaging and histology. Stroke. 1996 Nov;27(11):2110–8; discussion 2118-2119.

44. Yanagisawa M, Kurihara H, Kimura S, Goto K, Masaki T. A novel peptide vasoconstrictor, endothelin, is produced by vascular endothelium and modulates smooth muscle Ca2+ channels. J Hypertens Suppl Off J Int Soc Hypertens. 1988 Dec;6(4):S188-191.

45. Robinson MJ, Macrae IM, Todd M, Reid JL, McCulloch J. Reduction of local cerebral blood flow to pathological levels by endothelin-1 applied to the middle cerebral artery in the rat. Neurosci Lett. 1990 Oct 16;118(2):269–72.

46. Hughes PM, Anthony DC, Ruddin M, Botham MS, Rankine EL, Sablone M, et al. Focal lesions in the rat central nervous system induced by endothelin-1. J Neuropathol Exp Neurol. 2003 Dec;62(12):1276–86.

47. Fuxe K, Bjelke B, Andbjer B, Grahn H, Rimondini R, Agnati LF. Endothelin-1 induced lesions of the frontoparietal cortex of the rat. A possible model of focal cortical ischemia. Neuroreport. 1997 Jul 28;8(11):2623–9.

48. Biernaskie J, Corbett D, Peeling J, Wells J, Lei H. A serial MR study of cerebral blood flow changes and lesion development following endothelin-1-induced ischemia in rats. Magn Reson Med. 2001 Oct;46(4):827–30.

49. Schirrmacher R, Dea M, Heiss WD, Kostikov A, Funck T, Quessy S, et al. Which Aspects of Stroke Do Animal Models Capture? A Multitracer Micro-PET Study of Focal Ischemia with Endothelin-1. Cerebrovasc Dis Basel Switz. 2016;41(3–4):139–47.

50. Nakagomi S, Kiryu-Seo S, Kiyama H. Endothelin-converting enzymes and endothelin receptor B messenger RNAs are expressed in different neural cell species and these messenger RNAs are coordinately induced in neurons and astrocytes respectively following nerve injury. Neuroscience. 2000;101(2):441–9.

51. Sozmen EG, Kolekar A, Havton LA, Carmichael ST. A white matter stroke model in the mouse: axonal damage, progenitor responses and MRI correlates. J Neurosci Methods. 2009 Jun 15;180(2):261–72.

52. Mayzel-Oreg O, Omae T, Kazemi M, Li F, Fisher M, Cohen Y, et al. Microsphere-induced embolic stroke: an MRI study. Magn Reson Med. 2004 Jun;51(6):1232–8.

53. Winding O. Cerebral microembolization following carotid injection of dextran microspheres in rabbits. Neuroradiology. 1981;21(3):123–6.

54. Gerriets T, Li F, Silva MD, Meng X, Brevard M, Sotak CH, et al. The macrosphere model: evaluation of a new stroke model for permanent middle cerebral artery occlusion in rats. J Neurosci Methods. 2003 Jan 30;122(2):201–11.

55. Wilmes FJ, Garcia JH, Conger KA, Chui-Wilmes E. Mechanisms of blood-brain barrier breakdown after microembolization of the cat's brain. J Neuropathol Exp Neurol. 1983 Jul;42(4):421–38.

56. Overgaard K, Sereghy T, Boysen G, Pedersen H, Høyer S, Diemer NH. A rat model of reproducible cerebral infarction using thrombotic blood clot emboli. J Cereb Blood Flow Metab Off J Int Soc Cereb Blood Flow Metab. 1992 May;12(3):484–90.

57. Zhang Z, Zhang RL, Jiang Q, Raman SB, Cantwell L, Chopp M. A new rat model of thrombotic focal cerebral ischemia. J Cereb Blood Flow Metab Off J Int Soc Cereb Blood Flow Metab. 1997 Feb;17(2):123–35.

58. Orset C, Macrez R, Young AR, Panthou D, Angles-Cano E, Maubert E, et al. Mouse model of in situ thromboembolic stroke and reperfusion. Stroke. 2007 Oct;38(10):2771–8.

59. Ansar S, Chatzikonstantinou E, Wistuba-Schier A, Mirau-Weber S, Fatar M, Hennerici MG, et al. Characterization of a new model of thromboembolic stroke in C57 black/6J mice. Transl Stroke Res. 2014 Aug;5(4):526–33.

60. Niessen F, Hilger T, Hoehn M, Hossmann KA. Differences in clot preparation determine outcome of recombinant tissue plasminogen activator treatment in experimental thromboembolic stroke. Stroke. 2003 Aug;34(8):2019–24.

61. Wang CX, Todd KG, Yang Y, Gordon T, Shuaib A. Patency of cerebral microvessels after focal embolic stroke in the rat. J Cereb Blood Flow Metab Off J Int Soc Cereb Blood Flow Metab. 2001 Apr;21(4):413–21.

62. Smith WS, Sung G, Starkman S, Saver JL, Kidwell CS, Gobin YP, et al. Safety and efficacy of mechanical embolectomy in acute ischemic stroke: results of the MERCI trial. Stroke. 2005 Jul;36(7):1432–8.

63. Jia JM, Chowdary PD, Gao X, Ci B, Li W, Mulgaonkar A, et al. Control of cerebral ischemia with magnetic nanoparticles. Nat Methods. 2017 Feb;14(2):160–6.

64. Karimi Z, Karimi L, Shokrollahi H. Nano-magnetic particles used in biomedicine: core and coating materials. Mater Sci Eng C Mater Biol Appl. 2013 Jul 1;33(5):2465–75.

65. Working PK, Newman MS, Johnson J, Cornacoff JB. Safety of Poly(ethylene glycol) and Poly(ethylene glycol) Derivatives. In: Poly(ethylene glycol) [Internet]. American Chemical Society; 1997 [cited 2023 Feb 8]. p. 45–57. (ACS Symposium Series; vol. 680). Available from: https://doi.org/10.1021/bk-1997-0680.ch004

66. Yamaoka T, Tabata Y, Ikada Y. Distribution and tissue uptake of poly(ethylene glycol) with different molecular weights after intravenous administration to mice. J Pharm Sci. 1994 Apr;83(4):601–6.

67. Fercher AF, Briers JD. Flow visualization by means of single-exposure speckle photography. Opt Commun. 1981 Jun 1;37(5):326–30.

68. Briers JD, Fercher AF. Retinal blood-flow visualization by means of laser speckle photography. Invest Ophthalmol Vis Sci. 1982 Feb;22(2):255–9.

69. Li L, Lundkvist A, Andersson D, Wilhelmsson U, Nagai N, Pardo AC, et al. Protective role of reactive astrocytes in brain ischemia. J Cereb Blood Flow Metab Off J Int Soc Cereb Blood Flow Metab. 2008 Mar;28(3):468–81.

70. Mostany R, Miquelajauregui A, Shtrahman M, Portera-Cailliau C. Two-photon excitation microscopy and its applications in neuroscience. Methods Mol Biol Clifton NJ. 2015;1251:25–42.

71. Pawley JB, editor. Handbook Of Biological Confocal Microscopy [Internet]. Boston, MA: Springer US; 2006 [cited 2023 Jan 20]. Available from: http://link.springer.com/10.1007/978-0-387-45524-2

72. Lakowicz JR, editor. Principles of Fluorescence Spectroscopy [Internet]. Boston, MA: Springer US; 2006 [cited 2023 Jan 20]. Available from: https://link.springer.com/10.1007/978-0-387-46312-4

73. Shimomura O, Johnson FH, Saiga Y. Extraction, purification and properties of aequorin, a bioluminescent protein from the luminous hydromedusan, Aequorea. J Cell Comp Physiol. 1962 Jun;59:223–39.

74. Morise H, Shimomura O, Johnson FH, Winant J. Intermolecular energy transfer in the bioluminescent system of Aequorea. Biochemistry. 1974 Jun 4;13(12):2656–62.

75. Chudakov DM, Matz MV, Lukyanov S, Lukyanov KA. Fluorescent proteins and their applications in imaging living cells and tissues. Physiol Rev. 2010 Jul;90(3):1103–63.

76. Wang S, Hazelrigg T. Implications for bcd mRNA localization from spatial distribution of exu protein in Drosophila oogenesis. Nature. 1994 Jun 2;369(6479):400–3.

77. Livet J, Weissman TA, Kang H, Draft RW, Lu J, Bennis RA, et al. Transgenic strategies for combinatorial expression of fluorescent proteins in the nervous system. Nature. 2007 Nov 1;450(7166):56–62.

78. Kühn R, Schwenk F, Aguet M, Rajewsky K. Inducible gene targeting in mice. Science. 1995 Sep 8;269(5229):1427–9.

79. Zuo Y, Lubischer JL, Kang H, Tian L, Mikesh M, Marks A, et al. Fluorescent proteins expressed in mouse transgenic lines mark subsets of glia, neurons, macrophages, and dendritic cells for vital examination. J Neurosci Off J Soc Neurosci. 2004 Dec 8;24(49):10999–1009.

80. Feng G, Mellor RH, Bernstein M, Keller-Peck C, Nguyen QT, Wallace M, et al. Imaging neuronal subsets in transgenic mice expressing multiple spectral variants of GFP. Neuron. 2000 Oct;28(1):41–51.

81. Förster Th. Zwischenmolekulare Energiewanderung und Fluoreszenz. Ann Phys. 1948;437(1–2):55–75.

82. Stryer L, Haugland RP. Energy transfer: a spectroscopic ruler. Proc Natl Acad Sci U S A. 1967 Aug;58(2):719–26.

83. Siegel RM, Chan FK, Zacharias DA, Swofford R, Holmes KL, Tsien RY, et al. Measurement of molecular interactions in living cells by fluorescence resonance energy transfer between variants of the green fluorescent protein. Sci STKE Signal Transduct Knowl Environ. 2000 Jun 27;2000(38):pl1.

84. Tian L, Hires SA, Mao T, Huber D, Chiappe ME, Chalasani SH, et al. Imaging neural activity in worms, flies and mice with improved GCaMP calcium indicators. Nat Methods. 2009 Dec;6(12):875–81.

85. Tsien RW, Tsien RY. Calcium channels, stores, and oscillations. Annu Rev Cell Biol. 1990;6:715–60.

86. Stosiek C, Garaschuk O, Holthoff K, Konnerth A. In vivo two-photon calcium imaging of neuronal networks. Proc Natl Acad Sci U S A. 2003 Jun 10;100(12):7319–24.

87. Dana H, Chen TW, Hu A, Shields BC, Guo C, Looger LL, et al. Thy1-GCaMP6 transgenic mice for neuronal population imaging in vivo. PloS One. 2014;9(9):e108697.

88. Marzin J, Gérard J, Izraël A, Barrier D, Bastard G. Photoluminescence of single InAs quantum dots obtained by self-organized growth on GaAs. Phys Rev Lett. 1994 Aug 1;73(5):716–9.

89. Bouhelier A, Bachelot R, Lerondel G, Kostcheev S, Royer P, Wiederrecht GP. Surface plasmon characteristics of tunable photoluminescence in single gold nanorods. Phys Rev Lett. 2005 Dec 31;95(26):267405.

90. Sadat ME, Kaveh Baghbador M, Dunn AW, Wagner HP, Ewing RC, Zhang J, et al. Photoluminescence and photothermal effect of Fe3O4 nanoparticles for medical imaging and therapy. Appl Phys Lett. 2014 Sep;105(9):091903.

91. Barnes WL, Dereux A, Ebbesen TW. Surface plasmon subwavelength optics. Nature. 2003 Aug 14;424(6950):824–30.

92. Predescu AM, Matei E, Berbecaru AC, Pantilimon C, Drăgan C, Vidu R, et al. Synthesis and characterization of dextran-coated iron oxide nanoparticles. R Soc Open Sci. 2018 Mar;5(3):171525.

93. Mitchell MJ, Billingsley MM, Haley RM, Wechsler ME, Peppas NA, Langer R. Engineering precision nanoparticles for drug delivery. Nat Rev Drug Discov. 2021 Feb;20(2):101–24.

94. Chen Y, Liu L. Modern methods for delivery of drugs across the blood-brain barrier. Adv Drug Deliv Rev. 2012 May 15;64(7):640–65.

95. Neves AR, Queiroz JF, Weksler B, Romero IA, Couraud PO, Reis S. Solid lipid nanoparticles as a vehicle for brain-targeted drug delivery: two new strategies of functionalization with apolipoprotein E. Nanotechnology. 2015 Dec 11;26(49):495103.

96. Neves AR, Queiroz JF, Lima SAC, Reis S. Apo E-Functionalization of Solid Lipid Nanoparticles Enhances Brain Drug Delivery: Uptake Mechanism and Transport Pathways. Bioconjug Chem. 2017 Apr 19;28(4):995–1004.

97. Khalin I, Adarsh N, Schifferer M, Wehn A, Groschup B, Misgeld T, et al. Size-Selective Transfer of Lipid Nanoparticle-Based Drug Carriers Across the Blood Brain Barrier Via Vascular Occlusions Following Traumatic Brain Injury. Small Weinh Bergstr Ger. 2022 May;18(18):e2200302.

98. Marschallinger J, Iram T, Zardeneta M, Lee SE, Lehallier B, Haney MS, et al. Lipid-droplet-accumulating microglia represent a dysfunctional and proinflammatory state in the aging brain. Nat Neurosci. 2020 Feb;23(2):194–208.

99. Minsky M. Microscopy apparatus [Internet]. US3013467A, 1961 [cited 2023 Jan 20]. Available from: https://patents.google.com/patent/US3013467A/en

100. Gandin E, Lion Y, Van de Vorst A. Quantum Yield of Singlet Oxygen Production by Xanthene Derivatives. Photochem Photobiol. 1983;37(3):271–8.

101. Eggeling C, Widengren J, Rigler R, Seidel CA. Photobleaching of Fluorescent Dyes under Conditions Used for Single-Molecule Detection: Evidence of Two-Step Photolysis. Anal Chem. 1998 Jul 1;70(13):2651–9.

102. Greenbaum L, Rothmann C, Lavie R, Malik Z. Green fluorescent protein photobleaching: a model for protein damage by endogenous and exogenous singlet oxygen. Biol Chem. 2000 Dec;381(12):1251–8.

103. Göppert-Mayer M. Über Elementarakte mit zwei Quantensprüngen. Ann Phys. 1931;401(3):273–94.

104. Peticolas WL, Goldsborough JP, Rieckhoff KE. Double Photon Excitation in Organic Crystals. Phys Rev Lett. 1963 Jan 15;10(2):43–5.

105. Denk W, Strickler JH, Webb WW. Two-photon laser scanning fluorescence microscopy. Science. 1990 Apr 6;248(4951):73–6.

106. Khalin I, Heimburger D, Melnychuk N, Collot M, Groschup B, Hellal F, et al. Ultrabright Fluorescent Polymeric Nanoparticles with a Stealth Pluronic Shell for Live Tracking in the Mouse Brain. ACS Nano. 2020 Aug 25;14(8):9755–70.

107. Lee WCA, Chen JL, Huang H, Leslie JH, Amitai Y, So PT, et al. A dynamic zone defines interneuron remodeling in the adult neocortex. Proc Natl Acad Sci U S A. 2008 Dec 16;105(50):19968–73.

108. Xu HT, Pan F, Yang G, Gan WB. Choice of cranial window type for in vivo imaging affects dendritic spine turnover in the cortex. Nat Neurosci. 2007 May;10(5):549–51.

109. Trachtenberg JT, Chen BE, Knott GW, Feng G, Sanes JR, Welker E, et al. Long-term in vivo imaging of experience-dependent synaptic plasticity in adult cortex. Nature. 2002 Dec 19;420(6917):788–94.

110. Chow DK, Groszer M, Pribadi M, Machniki M, Carmichael ST, Liu X, et al. Laminar and compartmental regulation of dendritic growth in mature cortex. Nat Neurosci. 2009 Feb;12(2):116–8.

111. Keck T, Mrsic-Flogel TD, Vaz Afonso M, Eysel UT, Bonhoeffer T, Hübener M. Massive restructuring of neuronal circuits during functional reorganization of adult visual cortex. Nat Neurosci. 2008 Oct;11(10):1162–7.

112. Holtmaat AJGD, Trachtenberg JT, Wilbrecht L, Shepherd GM, Zhang X, Knott GW, et al. Transient and persistent dendritic spines in the neocortex in vivo. Neuron. 2005 Jan 20;45(2):279–91.

113. Egerton RF. Physical Principles of Electron Microscopy [Internet]. Boston, MA: Springer US; 2005 [cited 2023 Feb 2]. Available from: http://link.springer.com/10.1007/b136495

114. Knoll M, Ruska E. Das Elektronenmikroskop. Z Für Phys. 1932 May 1;78(5):318–39.

115. Williams DB, Carter B. Transmission Electron Microscopy [Internet]. New York, NY: Springer US; 2009 [cited 2023 Feb 2]. Available from: https://link.springer.com/book/10.1007/978-0-387-76501-3

116. Goldstein JI, Newbury DE, Echlin P, Joy DC, Lyman CE, Lifshin E, et al. Scanning Electron Microscopy and X-ray Microanalysis: Third Edition [Internet]. Boston, MA: Springer US; 2003 [cited 2023 Feb 2]. Available from: https://link.springer.com/10.1007/978-1-4615-0215-9

117. Schalek R, Kasthuri N, Hayworth K, Berger D, Tapia J, Morgan J, et al. Development of High-Throughput, High-Resolution 3D Reconstruction of Large-

Volume Biological Tissue Using Automated Tape Collection Ultramicrotomy and Scanning Electron Microscopy. Microsc Microanal. 2011 Jul;17(S2):966–7.

118. Hayworth KJ, Morgan JL, Schalek R, Berger DR, Hildebrand DGC, Lichtman JW. Imaging ATUM ultrathin section libraries with WaferMapper: a multi-scale approach to EM reconstruction of neural circuits. Front Neural Circuits [Internet]. 2014 [cited 2023 Feb 4];8. Available from: https://www.frontiersin.org/articles/10.3389/fncir.2014.00068

119. Kukulski W, Schorb M, Welsch S, Picco A, Kaksonen M, Briggs JAG. Precise, correlated fluorescence microscopy and electron tomography of lowicryl sections using fluorescent fiducial markers. Methods Cell Biol. 2012;111:235–57.

120. Spiegelhalter C, Laporte JF, Schwab Y. Correlative light and electron microscopy: from live cell dynamic to 3D ultrastructure. Methods Mol Biol Clifton NJ. 2014;1117:485–501.

121. Guizetti J, Schermelleh L, Mäntler J, Maar S, Poser I, Leonhardt H, et al. Cortical constriction during abscission involves helices of ESCRT-III-dependent filaments. Science. 2011 Mar 25;331(6024):1616–20.

122. Kolotuev I, Schwab Y, Labouesse M. A precise and rapid mapping protocol for correlative light and electron microscopy of small invertebrate organisms. Biol Cell. 2009 Dec 4;102(2):121–32.

123. Müller-Reichert T, Srayko M, Hyman A, O'Toole ET, McDonald K. Correlative light and electron microscopy of early Caenorhabditis elegans embryos in mitosis. Methods Cell Biol. 2007;79:101–19.

124. Watanabe S, Lehmann M, Hujber E, Fetter RD, Richards J, Söhl-Kielczynski B, et al. Nanometer-resolution fluorescence electron microscopy (nano-EM) in cultured cells. Methods Mol Biol Clifton NJ. 2014;1117:503–26.

125. Briegel A, Chen S, Koster AJ, Plitzko JM, Schwartz CL, Jensen GJ. Correlated light and electron cryo-microscopy. Methods Enzymol. 2010;481:317–41.

126. Haindl M, Filip J. Visual Texture [Internet]. London: Springer; 2013 [cited 2023 Mar 6]. Available from: http://link.springer.com/10.1007/978-1-4471-4902-6

127. Peters A, Palay SL, Webster H deF. The Fine Structure of the Nervous System. Neurons and their Supporting Cells. 3rd edition. J Neuropathol Exp Neurol. 1991 May 1;50(3):282.

128. SynapseWeb [Internet]. [cited 2023 Feb 16]. Available from: https://synapseweb.clm.utexas.edu/home

129. Wittmann M, Queisser G, Eder A, Wiegert JS, Bengtson CP, Hellwig A, et al. Synaptic activity induces dramatic changes in the geometry of the cell nucleus: interplay between nuclear structure, histone H3 phosphorylation, and nuclear calcium signaling. J Neurosci Off J Soc Neurosci. 2009 Nov 25;29(47):14687–700.

130. Miller RH, Raff MC. Fibrous and protoplasmic astrocytes are biochemically and developmentally distinct. J Neurosci Off J Soc Neurosci. 1984 Feb;4(2):585–92.

131. Nahirney PC, Reeson P, Brown CE. Ultrastructural analysis of blood-brain barrier breakdown in the peri-infarct zone in young adult and aged mice. J Cereb Blood Flow Metab Off J Int Soc Cereb Blood Flow Metab. 2016 Feb;36(2):413–25.

132. Oberheim NA, Takano T, Han X, He W, Lin JHC, Wang F, et al. Uniquely hominid features of adult human astrocytes. J Neurosci Off J Soc Neurosci. 2009 Mar 11;29(10):3276–87.

133. Tremblay MÈ, Zettel ML, Ison JR, Allen PD, Majewska AK. Effects of aging and sensory loss on glial cells in mouse visual and auditory cortices. Glia. 2012 Apr;60(4):541–58.

134. Peinado MA, Quesada A, Pedrosa JA, Torres MI, Martinez M, Esteban FJ, et al. Quantitative and ultrastructural changes in glia and pericytes in the parietal cortex of the aging rat. Microsc Res Tech. 1998 Oct 1;43(1):34–42.

135. El Hajj H, Savage JC, Bisht K, Parent M, Vallières L, Rivest S, et al. Ultrastructural evidence of microglial heterogeneity in Alzheimer's disease amyloid pathology. J Neuroinflammation. 2019 Apr 16;16(1):87.

136. Ornelas S, Berthiaume AA, Bonney SK, Coelho-Santos V, Underly RG, Kremer A, et al. Three-dimensional ultrastructure of the brain pericyte-endothelial interface. J Cereb Blood Flow Metab Off J Int Soc Cereb Blood Flow Metab. 2021 Sep;41(9):2185–200.

137. Nakano M, Atobe Y, Goris RC, Yazama F, Ono M, Sawada H, et al. Ultrastructure of the capillary pericytes and the expression of smooth muscle alpha-actin and desmin in the snake infrared sensory organs. Anat Rec. 2000 Nov 1;260(3):299–307.

138. Papa M, Bundman MC, Greenberger V, Segal M. Morphological analysis of dendritic spine development in primary cultures of hippocampal neurons. J Neurosci Off J Soc Neurosci. 1995 Jan;15(1 Pt 1):1–11.

139. Tremblay ME, Riad M, Chierzi S, Murai KK, Pasquale EB, Doucet G. Developmental course of EphA4 cellular and subcellular localization in the postnatal rat hippocampus. J Comp Neurol. 2009 Feb 20;512(6):798–813.

140. Tremblay MÈ, Lowery RL, Majewska AK. Microglial interactions with synapses are modulated by visual experience. PLoS Biol. 2010 Nov 2;8(11):e1000527.

141. Lee JH, Kim JY, Noh S, Lee H, Lee SY, Mun JY, et al. Astrocytes phagocytose adult hippocampal synapses for circuit homeostasis. Nature. 2021 Feb;590(7847):612–7.

142. Kilkenny C, Browne WJ, Cuthill IC, Emerson M, Altman DG. Improving bioscience research reporting: the ARRIVE guidelines for reporting animal research. PLoS Biol. 2010 Jun 29;8(6):e1000412.

143. Guillen J. FELASA guidelines and recommendations. J Am Assoc Lab Anim Sci JAALAS. 2012 May;51(3):311–21.

144. Ben-Bassat I, Bensch KG, Schrier SL. Drug-induced erythrocyte membrane internalization. J Clin Invest. 1972 Jul;51(7):1833–44.

145. Tutwiler V, Mukhitov AR, Peshkova AD, Le Minh G, Khismatullin RR, Vicksman J, et al. Shape changes of erythrocytes during blood clot contraction and the structure of polyhedrocytes. Sci Rep. 2018 Dec 17;8(1):17907.

146. Fung YC. Biomechanics [Internet]. New York, NY: Springer; 1993 [cited 2023 Feb 24]. Available from: http://link.springer.com/10.1007/978-1-4757-2257-4

147. Folkman J. Tumor Angiogenesis: Therapeutic Implications. N Engl J Med. 1971 Nov 18;285(21):1182–6.

148. Komar G, Kauhanen S, Liukko K, Seppänen M, Kajander S, Ovaska J, et al. Decreased blood flow with increased metabolic activity: a novel sign of pancreatic tumor aggressiveness. Clin Cancer Res Off J Am Assoc Cancer Res. 2009 Sep 1;15(17):5511–7.